UNIVERSITÀ DEGLI STUDI DI CATANIA
FACOLTÀ DI SCIENZE MATEMATICHE, FISICHE E NATURALI

LAURA FRANCALANZA

Exploring Central Collisions in the Reaction $^{58}Ni+^{48}Ca$ at 25 AMeV with CHIMERA

TESI DI DOTTORATO DI RICERCA IN FISICA

Relatori: *Chiar.mo Prof. Angelo Pagano*
Chiar.ma Prof.ssa Francesca Rizzo

XXVII CICLO

Contents

Introduction

Nuclear physics is not just a branch of physics, but, much more than this, it is a unique way to investigate aspects of nature still not fully understood, and not accessible by other routes.

Over many decades since the discovery of radioactivity, nuclear physics' studies have driven human knowledge toward the discovery of the nucleus, of the atomic configuration in the space and charge distribution, continuing incessantly through the street of beta decay and neutrino discovery, up to cosmic rays and sub-nuclear particles.

The study of the nuclear structure, came out from the far studies of the "plum pudding atomic model" of Thomson, the crucial Rutherford experiment and the improved Bohr's model, stimulated the evolution of the nuclear physics leading to consider the nucleus as a complex system ruled by strong and coulomb interactions.

Afterwards, technological innovations born from the ever growing needs of more performing machines, in order to going behind the fervent imagination of nuclear research, produced new possibilities in the ways to address and to approach this science, opening the doors to the long, very frequented and vivid road of nuclear reactions.

It is through the analysis of different reaction mechanisms in the collisions or through the synthesis of nuclear species not found in nature (since unstable), the goal is in any case the understanding of the properties of the matter that constitutes our Universe. Nuclear reactions between heavy ions in particular, already at energy of some tens of MeV in the laboratory frame, have energy enough to lead nuclear systems formed in the collisions in extreme conditions of temperature and density, far from the situation of finite nuclear matter (namely a nucleus) in its ground state.

It is possible to reach, for instance, conditions present only in the deep of the most compact neutron stars and investigate the behaviour of nuclear matter varying its density, thus leading to build the trajectory of nuclear matter in terms of temperature, pressure, volume, isospin: namely, the Equation Of State for finite nuclear matter.

Stimulated by this great opportunities, in the last decades an ever rising interest of nuclear research has been focused on thermodynamic aspects of the heavy ions reactions at intermediate energies, aiming to the investigation of the very fascinating and exciting world of the phase transitions and, more in general, of the whole class of critical phenomena. It can be interesting in this regard to quote the several connections highlighted between the phase transitions of nuclear matter and cosmo-gravitational phenomena like evolution of the early Universe at the Big-Bang and gravitational collapses [SIE83, SIE83b].

The possibility of a liquid – gas phase transition in the nuclear matter and of a region where the two phases can coexist, theoretically predicted already since the 60s, has been experimentally studied in a very extensively way, and it is nowadays an object of debate. From an experimental point of view, such a thematic is addressable through multifragmentation phenomena at intermediate energies (the so called "Fermi energy regime", ranging from about 10 to about 100 AMeV), as it will be better discussed in the first chapter.

Of course, it can be hard to imagine being able to recreate in laboratory what, up to the advent of accelerator machines, was observed only in the "sky", and indeed the achievement of such an ambitious goal called for efforts from both technological - instrumental and conceptual - interpretative point of view.

First of all, the phenomena triggered in a laboratory environment take a very short time, of the order of about 10^{-22} sec, and their observation depends on the asymptotic (after about 10^{-9} sec) information that we can achieve by the reaction products, properly collected by means of a particular apparatus (the detector, or multidetector).

By means of global variables related to a single collision event and to the reaction products' measured features it is possible to go back to the reaction process and to characterize the emitting sources. Information about the presence of a single source per event or more sources and their possible relationship, the size and the excitation energy of such sources, their N/Z ratio and temperature can be accessible.

The complete reconstruction of the collision event so becomes indispensable, i.e. the as complete as possible collection of the reaction products, together with their measure in term of charge, mass and energy: this is nowadays possible by means of

4π multidetectors that, covering a large solid angle around the target, are able to collect fragments and light particles from collisions with very high efficiency.

In this regard, in the second chapter the main basic features of the CHIMERA 4π multidetector located at the Laboratori Nazionali del Sud (LNS) in Catania are briefly described.

Moreover, the reaction mechanisms involved in a nuclear reaction are just in part under control, in the sense of a prior preparation and selection of their occurrence. Depending on the energy available in the reaction, on the impact parameter, but also on the size of the involved nuclei and on their characteristics (internal structure, N/Z ratio and so on), there several possible scenarios opened for the formation of excited nuclear clusters that can then decay through several different channels.

Such a strong competition between different reaction mechanisms is the main characteristic of the collisions at energies in the Fermi energy range, where the contemporary presence of mean field and two body dissipation processes make possible the competition between mechanisms typical of lower and higher energy in a same reaction.

For these reasons, the individuation of the different processes among all the possible reaction mechanisms occurred during a reaction become one of the first and most important challenge in order to study a given phenomenon.

In this regard, after a careful selection of centrality performed by means of an event shape analysis described in the third chapter, the fourth one will be entirely devoted to the exploration of a possible onset of multifragmentation phenomena in strong competition with evaporation-like mechanisms in central collisions from ^{58}Ni + ^{48}Ca central collisions. In particular such an investigation will drive us toward the selection of multifragmentation sources of mass around 100 amu (even if present just in small percentage) and their termodinamical characterization in terms of excitation energy and apparent temperature.

CHAPTER 1

Heavy ion collisions at intermediate energies.

1.1 The Fermi energy regime

Heavy ion collisions in the so called "Fermi energy regime" (namely between 10 and 100 AMeV) are one of the most studied topics in nuclear physics, mostly thank to the high variety of processes involved and to their relevant roles in the understanding of nuclear matter behaviour under several, also extreme, conditions of temperature and density.

From an experimental point of view, the access to important observables and the possibility to build very meaningful global variables, also by using last generation devices and multidetectors, have allowed a systematic and accurate study of the nuclear reactions in this energetic range, and leaded a rising interest by physicists from different laboratories in the world over the last thirty years.

Nuclear spectroscopy, as well as nuclear dynamics and nuclear astrophysics took a great boost from studies carried on in this energy region, whose richness lies in its intermediate position between low and high energy ranges, so in the coexistence and competition of several different reaction mechanisms.

As it's commonly known, the interaction between nucleons inside the nuclei can be explained via a mean field potential, where a nucleon that crosses a nucleus "feels" the whole of the nucleons inside it, or, alternatively, via a two body (nucleon-nucleon) dissipation process, depending on the energy involved in the reaction. And it's just the competition between these two processes that we can qualitatively understand by the following simple considerations, that characterizes the intermediate energy domain.

In a nucleus – nucleus (A-A) collision the nuclei relative velocity, v_{AA}, and so the relative energy, is related to the reduced relative wavelenght associated with a nucleon-nucleon collision $\lambda/2\pi$, by the simple expression:

$$\frac{\lambda}{2\pi} = \frac{h}{2\pi m v_{nn}}$$

Eq. 1.1

where m is the nucleonic mass. As the relative energy between nuclei increases, (and therefore v_{nn} increases), the associated $\lambda/2\pi$ decreases, and in a fixed target collision we can talk in terms of beam energy: rising values of beam energy, 1, 10, 100, 1000 AMeV, correspond to $\lambda/2\pi$ equal to 6.5, 2.1, 0.67, 0.24 fm respectively.

If we compare these lengths with the mean inter-nuclear distances (namely 2 fm), it's common to assume a predominance, in low energy collisions (up to 10 – 20 AMeV), of a one body (mean field) dissipation process, where a nucleon of the incident nucleus "sees" the whole nucleus around itself, experiencing the nuclear and the coulomb effective interaction as a result of an average potential of all the neighbouring nucleons. Similarly, at higher energy the associated wavelenght is short enough to be compared to the nucleon-nucleon relative distance and consequently the two body (n-n) interactions gain more and more relevance.

In the first case (namely up to 10-20 AMeV) the reaction mechanism in dominated by compound nucleus formation, fast (or quasi) fusion, and deep inelastic reactions [NGO78, GRE85, BON86]. Instead with increasing of energy a participant-spectator picture takes place, with the formation of a so called "fireball" in the overlapping zone between projectile and target nuclei that can reach large values of both excitation energy and nuclear density [PEI94].

The transition from one body to n-n interaction mechanism is not sharp, but the onset of the typical high energy processes competes with the progressive disappearance of the low energy ones, so that the energy region that hold this interchange becomes a very productive and challenging field of study for the understanding the "how", "why" and under what conditions nuclear matter chooses to follow one or another "behaviour". Such a behaviour, in terms of physical observables (like density, temperature, pressure, volume, isospin..) could be understood by means of an Equation Of State, the so called EOS of finite nuclear matter: following a precise trajectory in the phase space, just an EOS, nuclear matter

can explore several region of temperature and excitation energy very far from the ground state and around density far too from the saturation value.

Nowadays the main part of our knowledge regards symmetric nuclear matter at saturation density, so that further investigations about nuclear matter at extreme condition (and exotic nuclear matter too) are encouraged and carried out.

1.2 The importance of impact parameter

Several ingredients that we can manage in planning a nuclear reaction, such the already mentioned relative velocity of colliding nuclei, their masses and charges, the content of neutron with respect to proton (we will discuss about the quantum number called isospin) can drive the path of a nuclear collision, so that the choice of these asymptotic variables is a first selection of the mechanisms that will be involved in the reaction. Furthermore, there is another important ingredient that strongly affects the process and that we cannot manage or sorting, but just try to select on an event by event basis in the final phase of such an experiment: it is the impact parameter.

The impact parameter, usually indicated as "b", is in a semiclassical way related to the orbital angular momentum, l, in the entrance channel of the reaction:

$$L \cong \hbar l = bq$$

Eq. 1.2

where q is the asymptotic momentum and b represents the distance between the direction of the projectile's velocity and the parallel line passing through the centre of the target.

This is a typical aspect of collisions at low and intermediate energy, whose associated wavelenght is short with respect to the dimensions of the colliding region, so the quantum character of the incident wave is strongly attenuated, and the classical description, in terms of a well defined trajectory, is predominant.

The lower or higher value of this observable not only determines the nuclear region involved in the collision (that is a very important feature at the high energies) but it also drives the reaction toward different interaction mechanisms followed by the associated decay modes of the formed nuclei or de-excitation of nuclear systems

When the impact parameter assumes low values (under the "grazing" value), indeed, the projectile's trajectory is determined by the competition between the attractive nuclear potential and the Coulombian repulsive one.

In particular, along the last decades, several experiments have established that, at least at moderate energies (up to ≈ 40 AMeV), in peripheral and semiperipheral collisions the reaction mechanism has a mainly binary character: the observed Projectile Like Fragments (PLF) and Target Like Fragments (TLF) are products of de-excitation (via evaporation of neutrons and light charged particles) of primary products (quasi-projectile QP* and quasi-target QT*) from a binary reactions [SCH04]. This binary reaction mechanism at intermediate energy appears as a continuation of the deep inelastic collisions typical of the lower incident energy (fig.1.1).

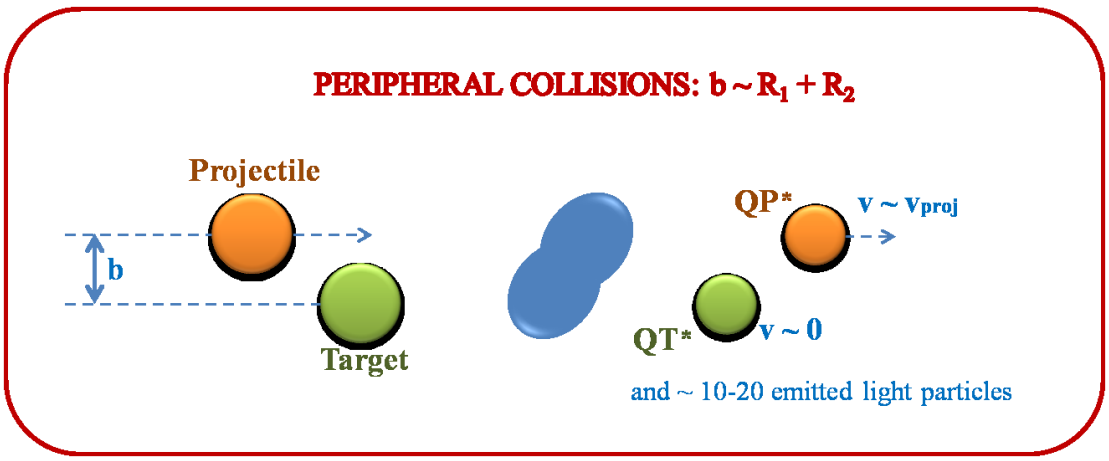

Figure 1.1 A Schematic picture of a semiperipheral collision at low - intermediate energy.

With increasing of the inelasticity, mostly for the semiperipheral collisions, this binary character is progressively reduced, and along with PLF, TLF and evaporated particles a new class of fragments called IMFs (Intermediate Mass Fragments, namely with $3 \leq Z \leq 12$) becomes an important feature of the intermediate energy collisions. The emission of these IMFs could not be explained by statistical decay of excited PLF or TLF [MON94, TOK95, LEC95, STE95, SOB97] so a systematic analysis carried out in the past years thanks to the advent of 4π detectors generation [LUK97, BOC00, LEF00, MIL01, MIL02, DAV02, PIA02, COLI03, DEF05,

DEF05b, RUS06] fixed some important peculiarities of this not statistical IMFs production (fig.1.2)

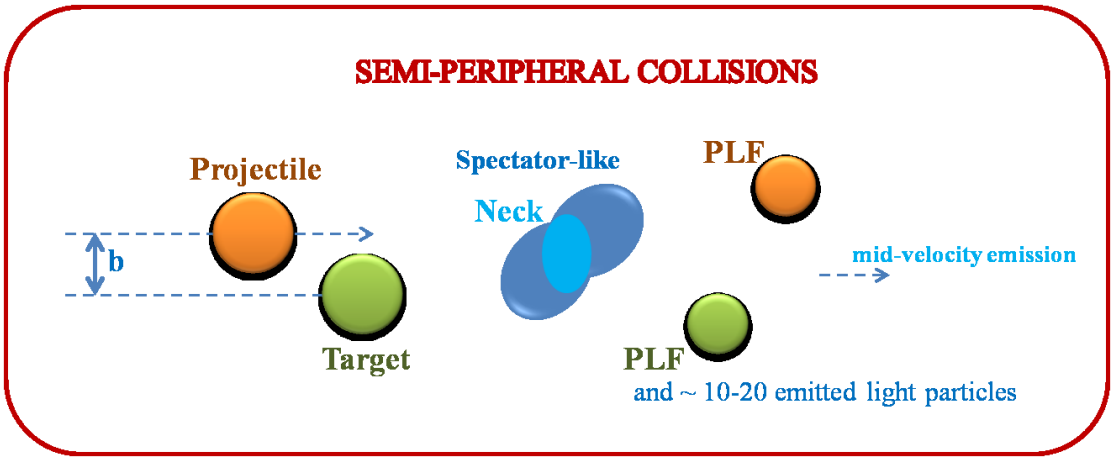

Figure 1.2 A schematic picture of neck emission: one of the possible reaction mechanisms in semiperipheral collisions.

Otherwise, with the decreasing of the impact parameter, so with increasing of "centrality", the collisions become more and more dissipative, because of a larger value of the overlapping mass involved that brings a large amount of the total energy available in the centre of mass. This can lead to very excited nuclear systems, characterized by high values of temperatures and density, and to "explosive" phenomena, that can be experimentally revealed such as a collection of intermediate mass fragments ($3 \leq Z \leq 15$) and light particles in a large solid angle around the target: the so called multifragmentation mechanism. [BOW93, SAN95, COR95, DAG96, POP98, BEA00] (this issue will be better discussed in the following chapters).

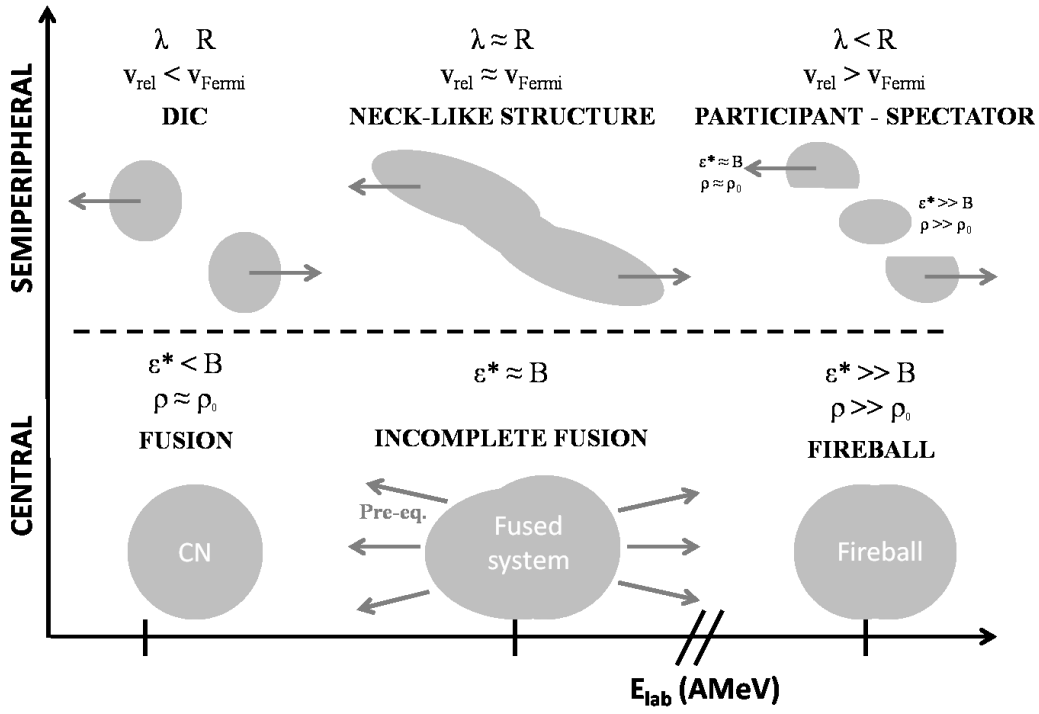

Figure 1.3 Diagram of the different reaction mechanisms with changing of incident energy (x axis) and impact parameter (y axis).

So a question is left open performing a nuclear reaction: since we cannot prepare our experiment just for central collisions, how we intend select the desired degree of centrality?

1.3 How to select the impact parameter?

In this paragraph I would like to discuss the most common methods that have been used by several experimental groups in the contest of heavy ion physics to select the centrality of the collisions. As above mentioned, the knowledge of the impact parameter is an important tool in order to select different reaction mechanisms, so in order to focus the analysis on one (or more) precise issue.

First of all, because of the impact parameter is not directly measurable, a researcher is called to find those variables that could be sensitive to this observable, and as a second step, if it's convenient and if they are not self-correlated, these variables can be related to one another.

Therefore, which are the more sensitive observables?

1.3.1 The importance of impact parameter

Of course, the most commonly used observable in both Fermi energy and relativistic nucleus - nucleus collisions is the multiplicity of detected particles (M_P). Indeed at intermediate energy, as cited above, one of the most relevant features is the production of IMFs whose number, in particular, changes with changing of the reaction mechanisms involved that strongly depend, finally, on the impact parameter value *b*.

In fig. 1.4 the total charged particles multiplicity (M_{CP} instead of M_P because CHIMERA is able to detect just charged particles) event by event is presented for the reaction $^{58}Ni+^{48}Ca$ at 25 *AMeV*: we can notice that this distribution shows a typical shape with a tail at high values of M_{CP}, due to the dominance of a binary reaction mode on the reaction mechanisms [CHA91, BEA96, BOR97, LAR98, PLA99]. In particular, for low excitation energy of the formed systems, the emission is characterized by a very low particles multiplicity (PLF, TLF and some light particles) and related to peripheral collisions.

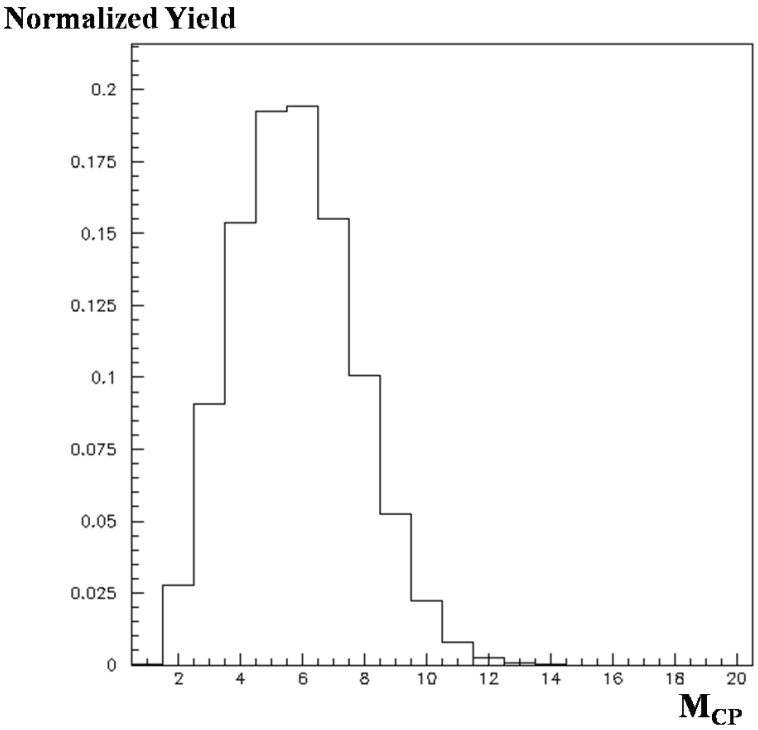

Figure 1.4 Charged particles multiplicity distribution for all the complete events in the $^{58}Ni+^{48}Ca$ at 25 AMeV reaction.

Since the rising violence of the collision, that drives the system toward more explosive phenomena, highest values of particles' multiplicity can be associated to central collisions, so that as a qualitative trend, we can imagine that the greater the multiplicity of detected particles the lower the impact parameter.

Moreover, under some assumptions, it is also possible to extract a quantitative relation between detected multiplicity and impact parameter [CAV90]: the so called "Cavata method". An example of correlation between multiplicity and impact parameter using Cavata method is given in figure 1.5 for two different systems colliding at the same energy [RUS06].

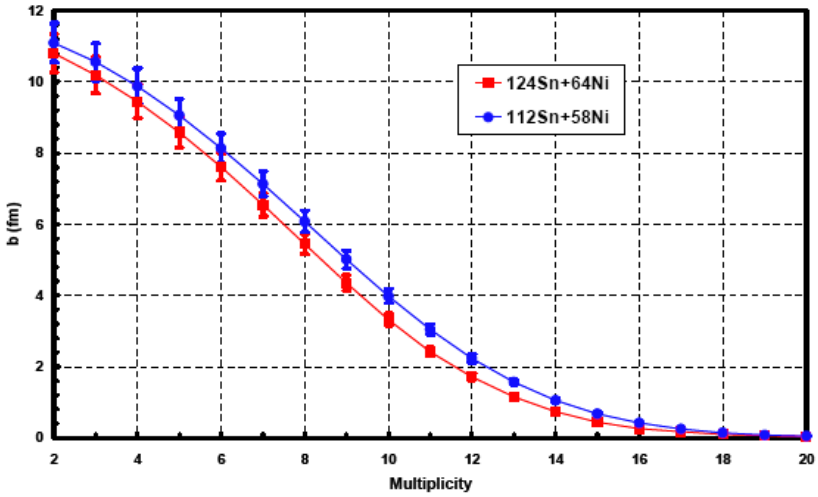

Figure 1.5 Estimated impact parameter b versus measured multiplicity for the system ^{112}Sn + ^{58}Ni (blue squares) and ^{124}Sn + ^{64}Ni (red circles) at 35 AMeV [RUS06]

Although this method is very commonly used, in the present work its use is not so convenient (as we will see in the following) and it's interesting and very relevant for the continuation of the analysis to understand the reason of such an issue. The incident energy of the studied reaction (*25 AMeV*) is indeed placed at the very beginning of the intermediate energy range, where the competition with low energy reaction mechanisms is strongest. Also in central collisions, indeed, similarly to what happens at low energy ones (with the formation of a compound nucleus after complete fusion), the charged particles multiplicity in not high and very similar to that observed in peripheral and semiperipheral ones (mostly binary and ternary). This is due to a reaction mechanism ruled by incomplete fusion followed by evaporation of light particles.

The incident energy is in fact not high enough to lead to high values of excitation energy of the composite system formed in central collisions, so that it is possible to assist just to an onset of multifragmentation, and therefore events with a high value of M_{CP} don't constitute the main contribution from such collisions.

1.3.2 Total Kinetic Energy Loss

Experimental evidences [CHA91] suggest that the Total Kinetic Energy Loss (TKEL) in a collision is a useful variable in order to evaluate the impact parameter b [STE95]: with increasing of the centrality degree, indeed, the energy violence of the collision increases. Therefore it increases also the energy that can be dissipated in both thermal and collective degrees of freedom and that we therefore cannot find as kinetic energy in the exit channel of the reaction. This available energy, that is the kinetic energy of the relative motion (translational) in the entrance channel, can be found as excitation energy of the projectile or target remnants, light particles or fragments emission.

The TKEL variable can be obtained as the difference between the kinetic energy in the entrance channel (E_{in} measured in the centre of mass frame) and that one in the exit channel of the reaction, TKE, measured as the sum of all reaction products kinetic energy before of any decay:

$$TKEL = E_{in} - TKE$$

Eq. 1.3

The experimental results show that the *TKEL* is well related to the impact parameter, both at low, where the pre-equilibrium processes are almost not present, and at intermediate energies [CHA91].

The two above cited variables (M_{CP} and TKEL), or methods, are the most commonly used, but there are also several other methods that can be used in order to quantitatively extract a value of the impact parameter, or, qualitatively, a degree of centrality. Usually, the choice of a precise method not only depends on the preferences of the authors, but mostly on the needs related to the apparatus and to the variables that are accessible in the experiment.

The CHIMERA multidetector, used to perform the experiment analysed in this thesis, can reveal charged particle for which it is possible to perform identification in charge, mass and energy. Furthermore, also thank to its high number of telescopes (so the high value of granularity) and the large covered solid angle, it is a powerful instrument to measure all global variables, so that both the methods of the Total

Particles Multiplicity (that with CHIMERA becomes Charged Particles Multiplicity) and the *TKEL* are very powerful tools to discriminate the classes of centrality.

Several other groups in the world use observables like the total transverse energy *Et* (defined in eq.1.4), or the transverse energy of light charged particles (Z=1,2) namely $Et_{1,2}$ [BOC00, PET90, PHA92]:

$$E_t = \sum_{i=1}^{N} E_i sin^2(\vartheta_i)$$

Eq. 1.4

Depending on the efficiency of the experimental set-up in measuring energy for different particles, it could be indeed convenient to restrict the summation in eq.1.4 to those particles for which threshold effects are weaker, such as the light charged particles, so obtaining the variable $Et_{1,2}$.

For the present work it was carried out a further method in order to select the centrality of the collision and, in particular, to isolate emissions from a unique source: the event shape analysis, that will be better discussed in the third chapter.

1.3.3 Event shape analysis

The event shape (in momentum space) is obtained by measuring and diagonalizing the kinetic tensor Q_{ij}:

$$Q_{ij} = \sum_{Z \geq 3} \frac{p_i p_j}{2m}$$

Eq. 1.5

where $p_{i,j}$ are the Cartesian components of the momentum of each fragment with $Z \geq 3$ in an event and m is its mass, being the summation extended over all fragments emitted in the same event.

In particular, we will refer to the so called "flow angle", ϑ_{flow}, that is the orientation of the first eigenvalues of Q_{ij} with respect to beam direction.

Such a procedure (see the third chapter for its application to the ^{58}Ni + ^{48}Ca reaction), taking into account the event shape in the momentum space and the

orientation of the main axis of this figure (an ellipsoid) with respect to the beam direction, is very useful to evaluate whether the system keeps or not memory of the entrance channel of the reaction.

We also have to remind that the three classes of centrality, namely peripheral, semi-peripheral and central, are not equiprobable, but the central one covers just a little part of the total cross section, so that the main part of the collision events is due to peripheral and semiperipheral collisions.

Moreover, as already stressed, any method we choose for the centrality selection, it refers to asymptotic variables, which are determined by different reaction mechanisms that are competitive at Fermi energy: the binary behaviour for instance, that is commonly related, at lower energy, to peripheral collisions, is still present for low value of *b* in such reactions, due to the memory of the characteristic mechanisms at low energies like the fusion-fission. For all these reasons there's not a unique good method for impact parameter evaluation, but it strongly depends, besides the experimental apparatus, on the considered system too, on the precise energy value (Fermi energy is a large range, namely from 10 to 100 AMeV) of the reaction, and on the reaction mechanisms expected for these. We will see in the next chapters that a restrictive selection of most central collisions is finally not simple and it could need the measure of several observable and their simultaneous use.

1.4 Central collisions: main features

The various reactions mechanisms accessible with a heavy ion collision open the doors to several aspects of nuclear matter, allowing the exploration of different regions of temperature, excitation energy, density, isospin, and so on.

The central collisions in particular, leading to the most violent reactions between heavy nuclei, can investigate the properties of finite nuclear matter in conditions very far from the ground states of the nuclei.

Although some general properties of such collisions at intermediate energies are already established, these still are object of experimental and theoretical study of the international scientific community. We will see how some processes involved in

central collisions provide indeed a valuable tool for probing the nuclear Equation Of State (EOS) [DAN01, BAR05] and may indicate a liquid-gas phase transition in finite nuclear system [POC95, POC96, HAU98, MIL98].

The most central collisions can lead to the formation of a unique source, characterized by excitation energy comparable with the nucleons' binding energy. This system can undergo several decay modes depending on its angular momentum, its density, its excitation energy…

At moderate excitation energy ($E^* \leq 3AMeV$) the dominant decay modes are particle evaporation leading to heavy residues, and statistical fission, accompanied or anticipated (in this case we talk of "pre-equilibrium emission") by light particles emissions. These processes are almost relevant at low incident energy, where the projectile and target nuclei form a compound nucleus, that is a nucleus with life time long enough (10^{-16} – 10^{-20} s) to equilibrate all the freedom degrees, both intrinsic and collective, excited above its ground state: if the mass and charge of this nucleus are critical for fission, this splits into two big fragments, if not it evaporates light particles up to its complete deexcitation, following a statistical decay.

The role of the angular momentum is also important at this stage, because a high value of this quantum number can "reduce" the height of the fission barrier and opens that decay channel.

Otherwise, when excitation energy rises up to a significant fraction of the binding energy ($E^* \gtrsim 3AMeV$) intermediate mass fragments emission takes place (see figure 1.6), indicating the onset of the so called fragmentation [BOW93, SAN95, COR95, DAG96, POP98, BEA00].

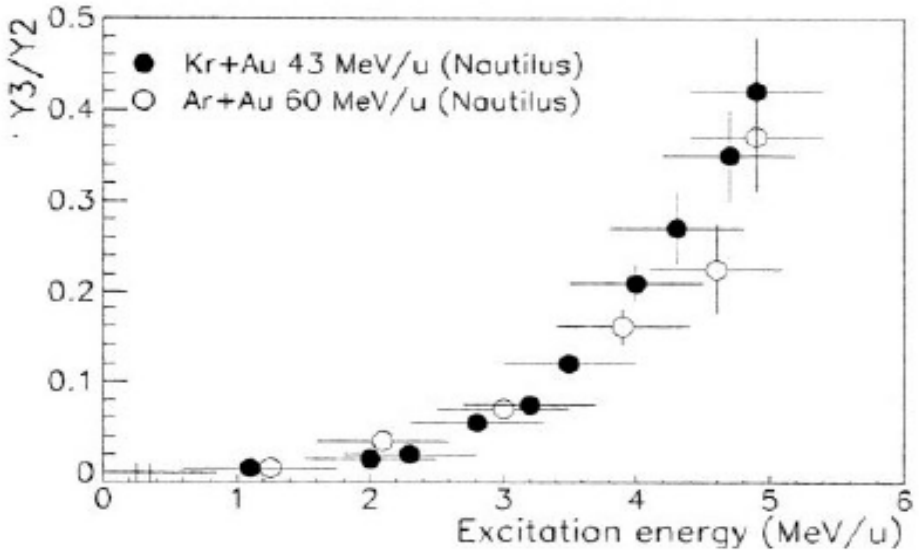

Figure 1.6 Evolution of the competition between fission events (two bodies) and three body decay as function of the excitation energy. Sources with mass A = 200-220 amu from central and semi-central collisions.

At these excitation energies, reachable at incident energy above 10 AMeV, there's not yet the formation of a proper compound nucleus: the system after the collision has not time to relax all degrees of freedom before going toward other allowed very energetic mechanisms. We will refer to such systems as "composite nuclei", or "confined nuclear matter", and to the process as "incomplete fusion".

In figure 1.7 the ratio between the complete fusion cross section and the total cross section is shown as function of the incident energy for six different systems: it's possible to notice how the contribution of the complete fusion become less and less relevant above E_{inc} = 10 AMeV, up to reach very low values proceeding through all the Fermi energy range.

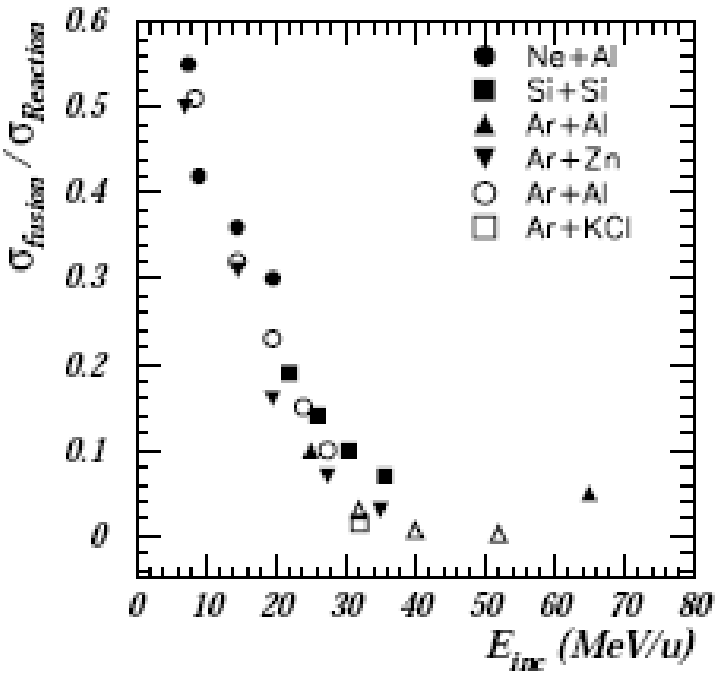

Figure 1.7 Evolution of the complete fusion cross section and reaction cross section ratio with increasing of incident energy for six different systems […].

It is important to underline that this trend is finally independent from the system, thus from the entrance channel of the reaction.

1.5 Multifragmentation

Multifragmentation [BOW93, SAN95, COR95, DAG96, POP98, BEA00], constituting the main decay channel of nuclear matter formed in central heavy ion collisions at intermediate energies, has received great attention by a large number of physicist who looked at this process as to an evolution, with rising of the excitation energy, of the light particles' evaporation process in the low energy regime.

Moreover, the role of the dynamics in the fragments formation is an attractive issue for an understanding of the reaction mechanisms in this Fermi regime, characterized by the presence of a copious production of IMFs.

1.5.1 Experimental evidences

Multifragmentation can be observed in central collisions or, alternatively, as decay of the partners of binary, both central and semi-peripheral, collisions, depending on the incident energy.

Over the Fermi energy regime, for very dissipative binary collisions, the outgoing PLF^* and TLF^* can be so much excited ($E^* > 3$-4 AMeV) to decay via multifragmentation: this process is characterized by an higher value of the cross section with respect to that in central collisions and by the presence of fragments in the mass region between PLF and TLF.

Otherwise, for central collisions, the multifragmentation cross section doesn't exceed values of about 100 mbarn and the fragments emission is isotropically distributed in the centre of mass reference frame. In figure 1.8 it is shown the mean value of the IMFs multiplicity, as function of the periphericity (measured by b/b_m, being b_m the grazing impact parameter) for three different values of incident energy in the reaction Au + Au: the multifragmentation is favoured in central collisions at about 100 AMeV (the upper part of Fermi energy regime) and in semi-peripheral collisions at higher energy.

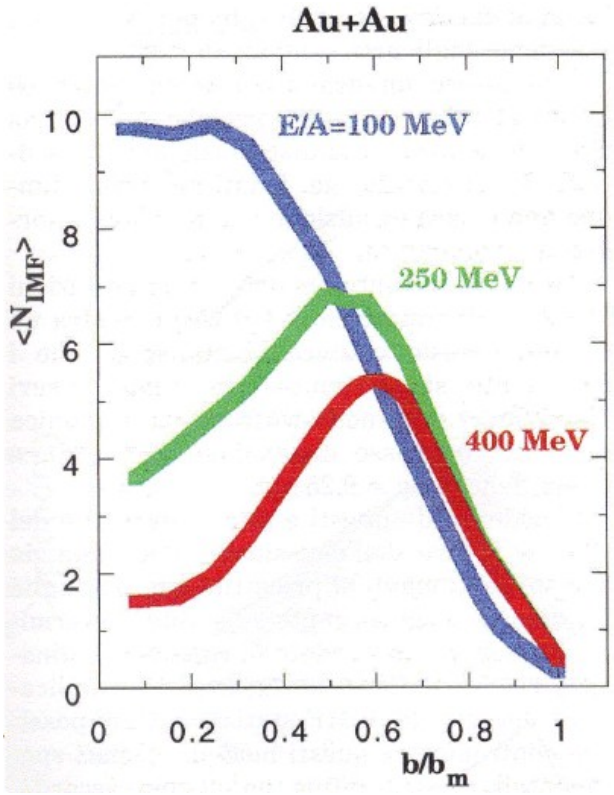

Figure 1.8 Mean IMFs multiplicity as function of reduced impact parameter for four different incident energy from Aladin collaboration. form [GER11].

From an experimental point of view, the characteristics of multifragmentation can be explored measuring some observables such as the mass and the charge distributions, and following their evolution as a function of the dissipated energy.

For both central and semiperipheral collisions, such an IMFs production is observed as a universal mechanism, independent on the nuclei involved in the reaction or on the incident energy, showing a complete domain of the energy released to the composite system: the multiplicity of fragments shows a maximum at $E^{*} \approx$ 8 -10 AMeV and then decreases, due to the beginning of the vaporization regime [BAC95, RIC01, RIV01, BON00], namely the disintegration of the system in a large number of light particles (Z = 1,2) (see figure 1.9). This "rise and fall" of multifragmentation with the increasing violence of the collision has been observed in the first experiment with ALADIN [OGI91] and in figure 1.10 we can see the same behaviour for central ^{84}Kr + ^{197}Au collisions with the Miniball/wall array [LYN95].

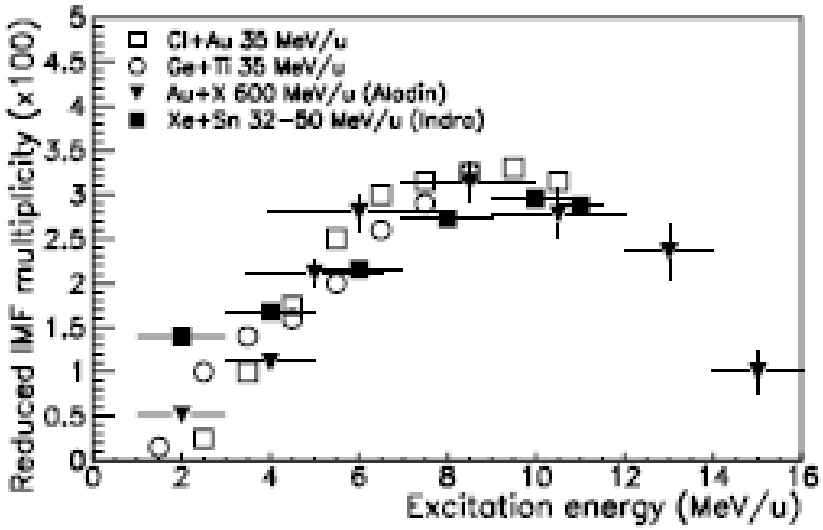

Figure 1.9 Rise and fall of multifragmentation (in terms of reduced IMF multiplicity vs excitation energy) as observed by Aladin and Indra collaborations. From [DUR98] and references therein.

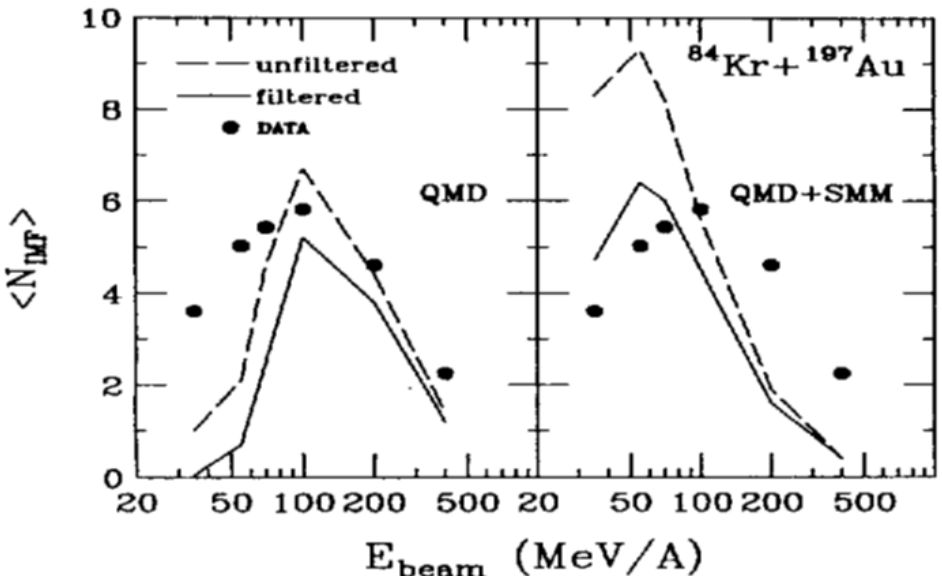

Figure 1.10 Mean IMF multiplicities for ^{84}Kr + ^{197}Au collisions as a function of beam energy [LYN95].

1.5.2 Equilibrium hypothesis and statistical model

The independence of such a mechanism on the projectile and target nuclei and, in general, on the entrance cannel of the reaction, suggests that the system that experiences multifragmentation is already enough thermally and chemically equilibrated. In this sense, multifragmentation statistical models (the most common

are the Berlin model [GRO86] for a prompt multifragmentation and the SMM model of Copenhagen [BOND95] that considers a possible sequential emission) well reproduce the experimental data assuming the system (namely the source of fragments) being in an equilibrium stage (with respect to this, see the following paragraphs): the models consider a source at low nuclear density with respect to the saturation density ρ_0 ($1/3\rho_0$) where the fragments are simultaneously produced and isotropically distributed in its volume. In this statistical framework the multifragmentation follows bulk instability, in contrast with mechanisms involving surface instability, such as the fragment emissions from neck region in peripheral and semi-peripheral collisions.

Anyway it is important to keep in mind that such models need often some "ad hoc" inputs like the excitation energy, the mass, the density of the source at the freeze-out, and any other parameters, and that a sample of input values well reproducing experimental data could not be unique.

1.5.3 Time involved

Moreover, several analyses carried out about the time related to the multifragmentation, by studying the velocity correlation functions (fragments interferometry) and following matching with theoretical simulations, show that such a process is a fast process: in particular, cause the fragments are simultaneously emitted, multifragmentation appears as a fast "one step" process, with typical associated time of about *100 fm/c* (figure 1.11), comparable with time taken for the complete energy transfer and equilibration of internal degrees of freedom (and this is very important to support the equilibrium hypothesis), but at least an order of magnitude smaller then the time expected time for the decay of the compound nucleus formed at low energies, where the fragment are sequentially emitted in a "multi-step" way.

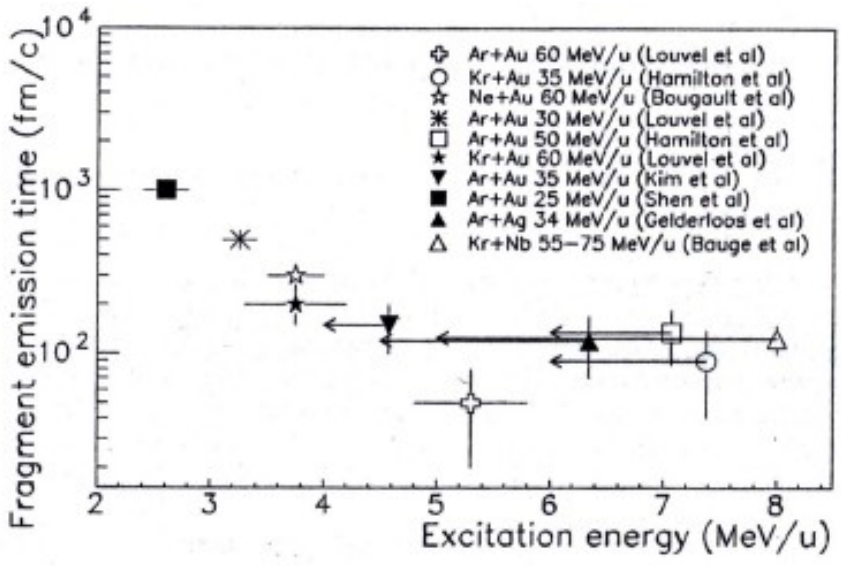

Figure 1.11 Fragment emission time vs. excitation energy evaluated for several systems: for E*≥4-5 MeV it is possible to observe time saturation at about 100 fm/c [DUR01].

Nevertheless, some ambiguities relate to space-time properties of the emitting sources persist, since neither the source sizes nor its lifetime are known: small sources emitting in a long time and big ones emitting in a shorter time produce the same kind of correlation functions, so that an efficient discrimination between them may be very difficult.

1.5.4 Dynamics and thermodynamics

Usually, for a better understanding of the formation stage of such hot sources, it is useful to refer to dynamical models, which take into account several stages of the collisions from the very beginning up to the so called "freeze-out".

The similarity between effective nucleon-nucleon interaction (that shows a short range repulsive potential, and an attractive one at long range) and the Van der Waals molecular gas forces stimulated the research for a possible nuclear matter phase transition.

With respect to this, dynamical calculations in the framework of the transport theory predict a first stage of the nuclear collision, during about ~ 50 *fm/c*, characterized by a strong compression of the nuclear system.

In such a situation the density is greater than the saturation one, with a consequent rising of temperature; consequently the system would experience an expansion, corresponding to a decreasing of the density, which leads it within the so called "coexistence region", a metastable region between a Fermi's liquid ($E^* \propto T^2$) and a Boltzmann's gas ($E^* \propto T$) phase of nuclear matter.

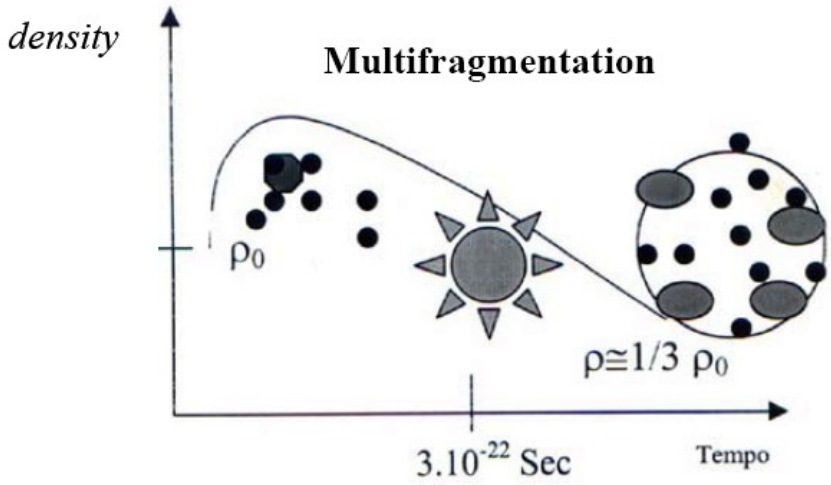

Figure 1.12 Schematic picture of time-density evolution during central collision at intermediate energy [RUS06]

According to such model calculations, by using mean field theory and parameterizing the nuclear interaction with the Skyrme forces, it is possible to obtain an equation of state (EOS) for infinite nuclear matter[1] that predicts a critical point, at T_c=16 MeV and $\rho_c \approx {}^1/_3\,\rho_0$, below which (i.e. for lower values of temperatures, inside the metastable coexistence region) it is possible to distinguish a region called "spinodal region", characterized by small density fluctuations (look at figures 1.12 and 1.13 for a schematic picture). Such small fluctuations can exponentially grow, so that the system would experience mechanical instabilities (negative values of the derivate of the pressure with respect to the density: fig. 1.14) that could disassemble it, giving rise to a prompt multifragmentation.

[1] The infinite nuclear matter is an idealized matter consisting of protons and neutrons in an infinite volume where the coulomb interactions are not present. The infinite volume implies no surface effects, so that finally the the binding energy for such a kind of matter is about 16MeV, in contrast with that for nuclei (about 8 MeV).

In particular, it can be shown that because of the finiteness of the nuclear forces and to the length imposed by the quantum Heisenberg uncertainty principle such instabilities present a precise wave length [CHO94, GUA97] that favours the breaking of the system in equal size fragments [CHO08].

If the system survives, a heavy and hot source will be formed, that could de-excite statistically emitting both light particles and IMFs.

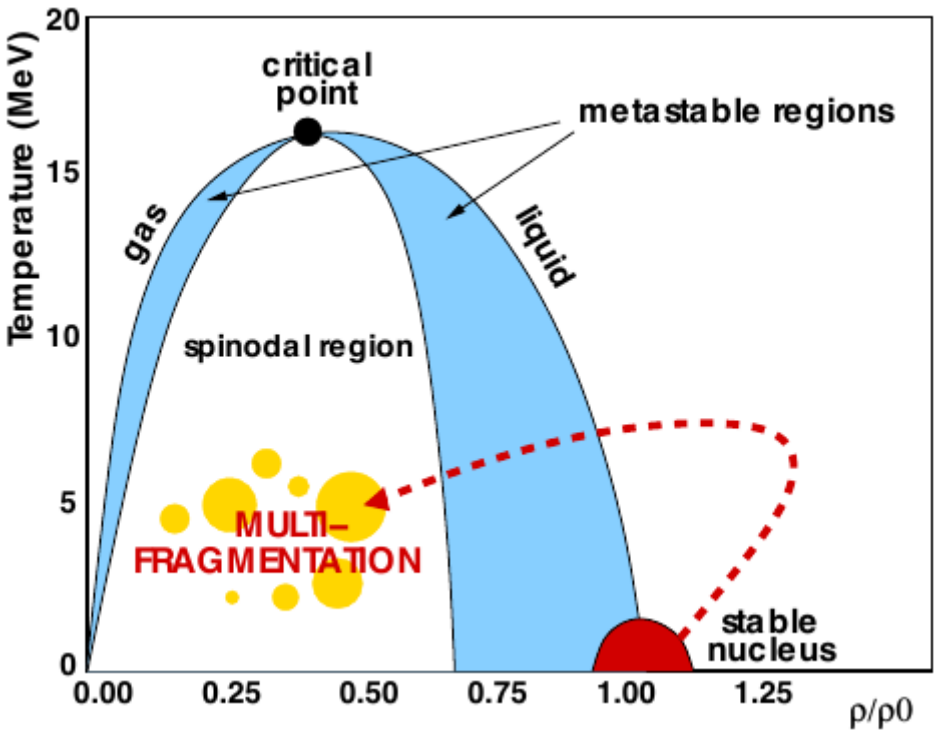

Figure 1.13 Pictorial view of the different regions of temperatures and density for infinite nuclear matter.

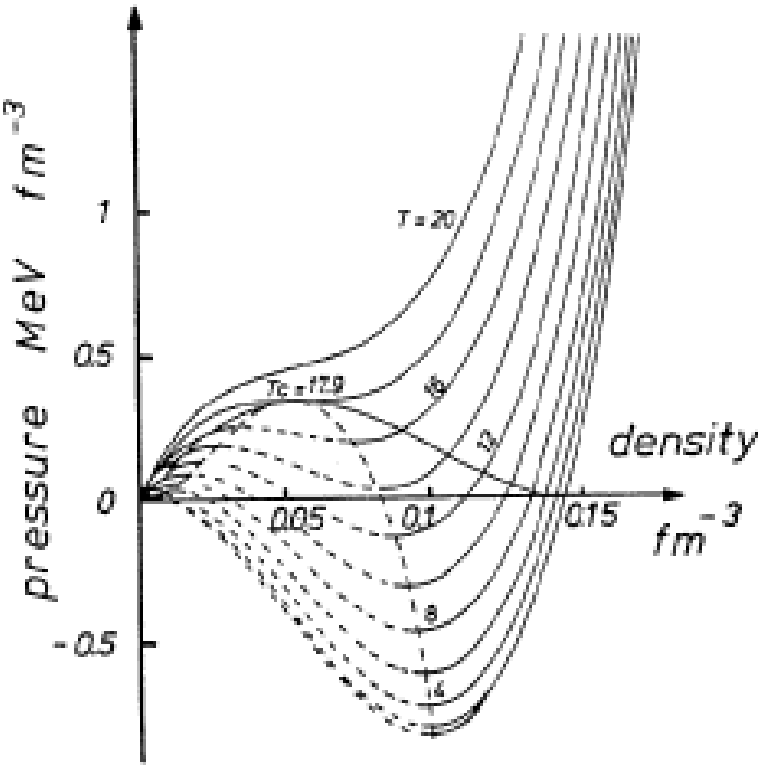

Figure 1.14 Isotherm curves in the pressure – density plane: it is consider a phenomenological equation of state parameterized with the Skyrme forces. In such a representation the saturation point corresponds to the zero pressure point at finite density and the liquid-gas coexistence to the drawn full line. The dashed lines correspond instead to the mechanical instabilities of the spinodale region [DUR01 and reference therein].

Whether this is the scenario for infinite nuclear matter, the situation is slightly more complicated when we want to extend such concepts, as the existence of a relation between pressure and density (so temperature), that means the existence of an equation of state, to finite nuclei: a nucleus is indeed a system with a finite number of components (nucleons) kept in a volume and, if excited, behaves as a transient hot system without an external pressure field that keeps it at values of volume and pressure fixed by the mean field.

In such a situation the definition of temperature is also delicate and it requires a strong hypothesis of thermalization of the system: in the past decade there have been many attempts to test if a thermal equilibrium was a reasonable approximate description of the multifragmenting sources [POC95, GUL97, TSA96, NAT00].

Experimentally, in searching for evidences for such a compression phase followed by an expansion one, the collective flow is a very useful observable: kinetic energy distributions for all emitted particle in several experiments have shown a contribution of collective energy that can be well reproduced assuming the existence of a common expansion velocity (due to the expansion mechanical boost plus coulomb repulsion that involves all the particles in the system) for all emitted fragments:

$$\langle E_{kin} \rangle = \langle E_{thermal} \rangle + \langle E_{collective} \rangle \rightarrow \langle {}^{E_{kin}}/_{A} \rangle = {}^{3}/_{2}\, TA + \langle {}^{E_{collective}}/_{A} \rangle$$

Eq. 1.6

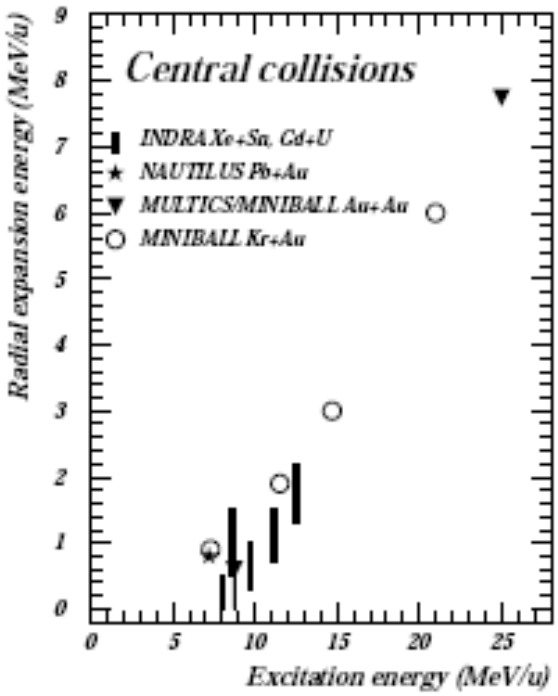

Figure 1.15 Systematic of the radial expansion energy as a function of excitation energy per nucleon in central collisions at Fermi energies [DUR01 and ref. Therein].

Since the expansion has not a favourite direction, but it's isotropic (that is a further indication for an emission from equilibrated system), the radial collective flow is an important tool: this collective contribution to kinetic energy become relevant for incident energy over *30-40 AMeV*, corresponding to an excitation energy of about 5 MeV in central collisions (see fig. 1.15) and reaches about the 30-50% of the total available energy for $E_{inc}/A \approx 100\ AMeV$.

The thermal contribution is more important for light particles, while the collective one is relevant for higher values of masses, so that E_{kin}/A *Vs* A (or Z) is a good variable to which refer in order to distinguish the two components of the kinetic flow.

Coming back to involved times and to the termodinamical equilibrium hypothesis for multifragmentation sources, it's important noticing that at Fermi energies the collective velocity values correspond to an expansion time greater than the thermalization time: that's very important for the freeze-out definition in statistical models.

1.5.5 Thermodynamics and liquid-gas phase transition

In the past decade many analyses have been performed in order to put in evidence the liquid-gas phase transition in nuclei [CHO97].

Phase transitions are known to be related to critical behaviours and to be ruled by universal properties. In particular, at the critical point the system presents a fractal structure and so scaling laws [FIS67] should be hold: this leads for example to the famous power low shape of the fragment size distribution (fig. 1.16) [GUA94, DAG00, CHO97]. These critical behaviours have been identified in many nuclear reactions. The inferred critical exponents are in reasonable agreement with those expected for the liquid-gas phase transition.

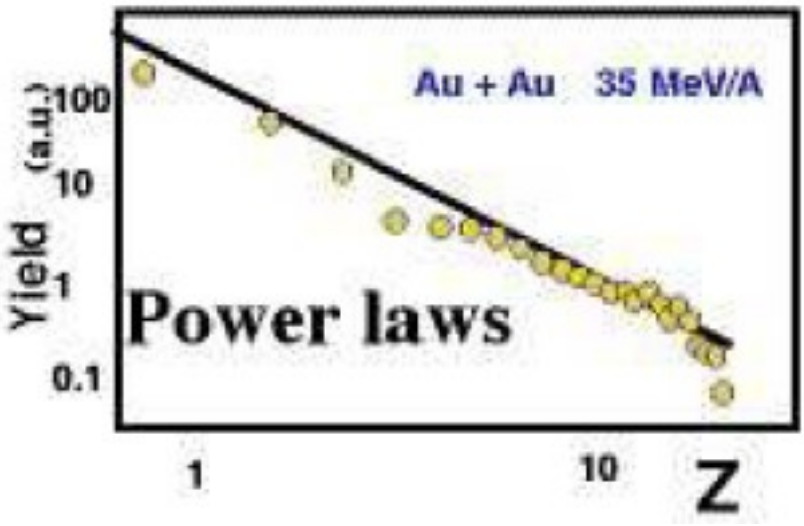

Figure 1.16 Typical fragment size distribution fitted by a power law indicating the proximity of a critical point. [CHO97]

The scaling is indeed based on the simple idea that a real gas of interacting particles can be considered as an ideal gas of clusters in chemical equilibrium and this can be seen as the basis of many multifragmentation models. In finite systems not only the fragments (gas) distribution can be studied but also the largest fragment (liquid) distribution can be measured, and these may be considered, together with other several experimental evidences [CHO97, figure 1.17], among the strongest signals for a liquid-gas phase transition of nuclear matter [BOT00].

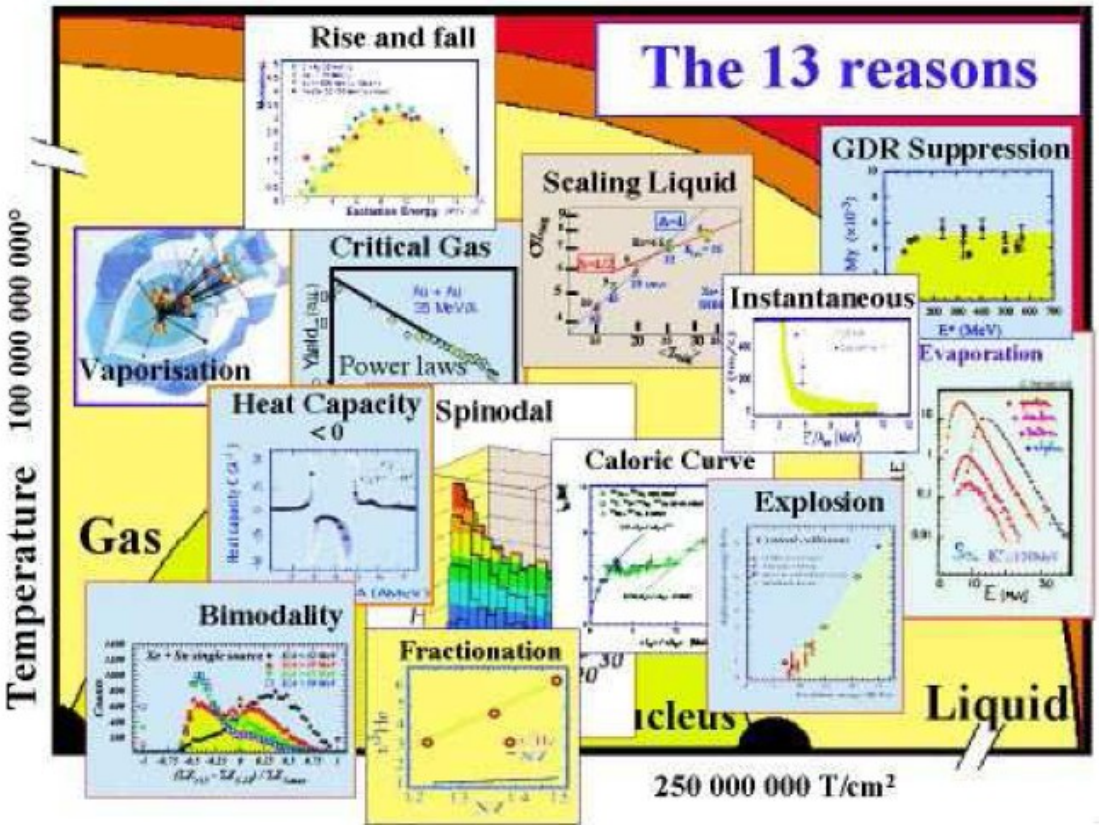

Figure 1.17 Sketch of the 13 signals of the nuclear liquid gas phase transition [CHO97].

Moreover, in order to get direct information about the nuclear phase diagram and the associated equation of state it is possible to define termodinamical variables and to build, by studying their correlations, a caloric curve, usually presented as the variation of temperature as function of excitation energy (figures 1.18) [POC95, GUL97, MIL98, NAT02].

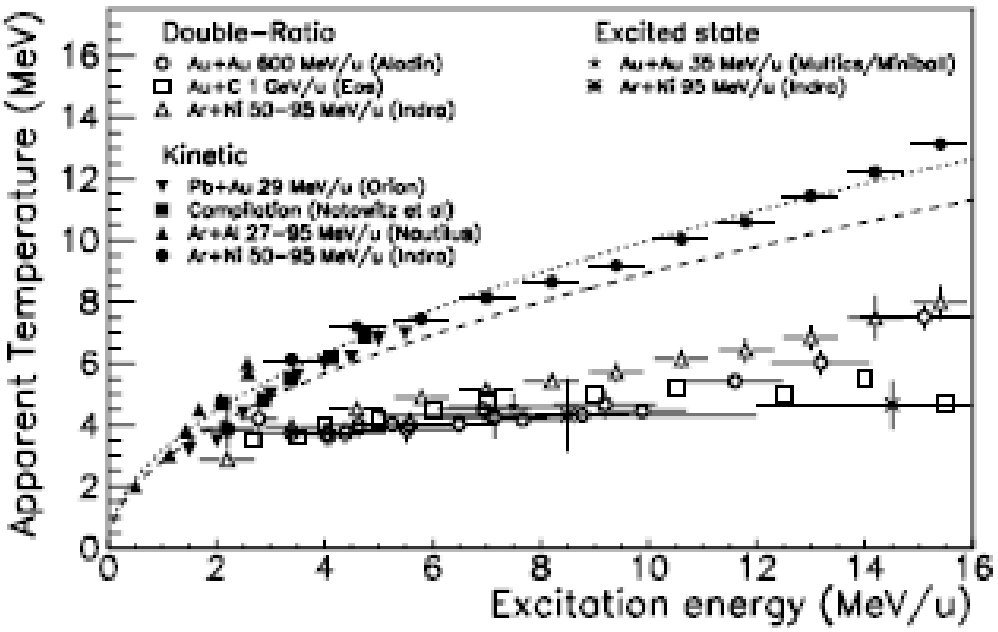

Figure 1.18 Systematic of measured nuclear temperatures with the three different methods briefly discussed in the following of the section. From [DUR01] and references therein.

Such first results highlighted evidences for a phase transition as an almost constant temperature over a broad range of energies, the so called “plateau”.

It has been shown that the mass of the fragmenting system has also an influence on the observed caloric curve [NAT02, NAT08], the temperature of the observed plateau decreasing with such a value of mass.

Temperature measurements [ALB85, LEN99, DAG00, DAG02, GER04, GER04b] (called “apparent” since the difference between results from different methods) can be achieved by using different thermometers like the slope of the kinetic energy spectra (“kinetic temperature”), the ratio between excited states population (“internal temperature”) and the double ratios of isotope yields (“chemical temperature”) (see figure 1.19 for a pictorial representation of the three methods).

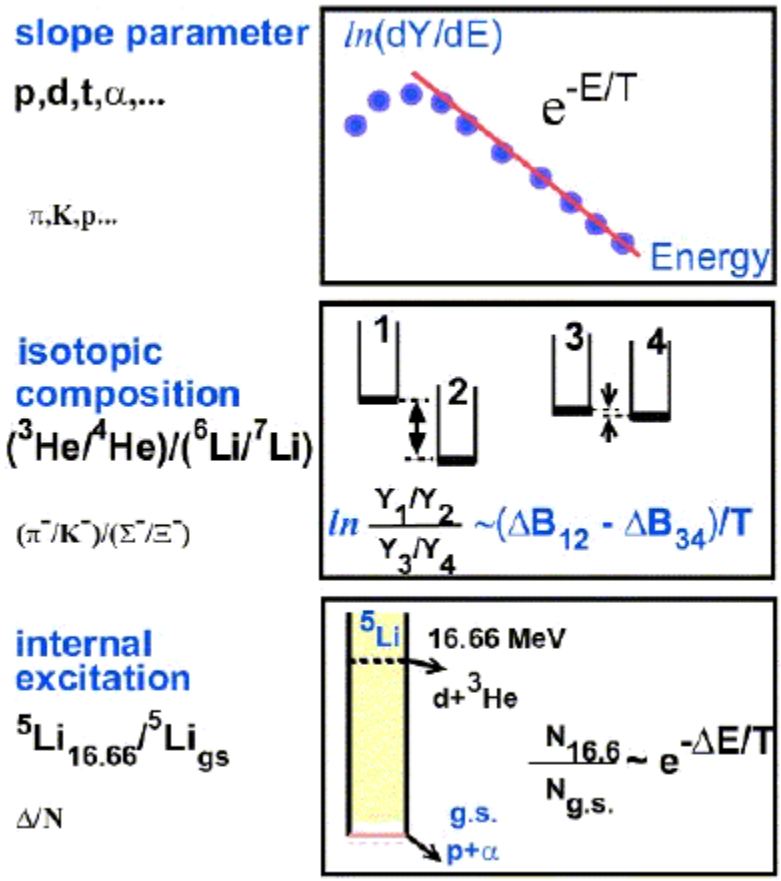

Figure 1.19 Schematic description of the three methods used in measuring temperature of emitting sources in nuclear collisions. From [GER11].

The definition of temperature for an excited nucleus is actually not easy, first of all because of the difficulty in building a relation between temperature and excitation energy for a small system. Such a problem, that theoretically is addressed in terms of microcanonical or canonical approach, is experimentally overcome by looking at a collection of nuclei at the same time: in this way the cumulative effect due to the high number of observations reduces the limitations due to the small size of the primary studied system (the single emitting source). Moreover, another important issue is the fact that an excited emitting nucleus is an open system: in a statistical framework indeed it can exchange matter and energy with the outside.

From an experimental point of view the temperature is measured starting by the probability of emission of a given particle with a precise kinetic energy, related to the

density of states of the residue after evaporation, $\rho(E^*)$, as a function of its excitation energy.

All the three above mentioned methods are thus based on an experimental determination of the density of state of the decaying hot nucleus as a function of the excitation energy, differing by using several properties of emission products.

Briefly, the so called "kinetic" method is based on measuring the slope of kinetic distributions of evaporated particles and light fragments, under the assumptions of the direct connection between such a quantity and $\rho(E^*)$. In a first approximation the kinetic energy spectrum is addressed as a Maxwell distribution, as coming from a surface emission, but an important issue in such considerations is the possibility that the excitation energy of the emitting system could be enough to lead to a prompt multifragmentation. In the latter case indeed all the particles are emitted in a single step, coming from a bulk emission of the nuclear source and a possible correction in the sense of a Boltzmann approximation has to be taken into account.

The second method, that measures the so called "internal excitation" temperature, is instead performed by studying discrete state population ratios of selected nuclear species. It assumes that the relative probability to excite different states of a given cluster is directly linked to the density of states by means of a Boltzmann factor.

Finally, the method of double ratios of isotope yields, assuming the existence of a unique source for all used isotopes, the thermal and chemical equilibrium of the such a source and the validity of the Maxwell-Boltzmann statistics for the system, has the aim to measure the temperature starting from the probability of formation of a given cluster, that depends on the chemical potential.

In the case of a hot source at density lower than the saturation one, for which the determination of the chemical potential is not readily accessible experimentally, this purpose is reached by measuring the population ratio between two couples of nuclear species differing for a neutron or for a proton [ALB95].

See section 4.4 for further explanations about the isotopic ratios method and its application to the ^{58}Ni+^{48}Ca system.

CHAPTER 2

Overview of the CHIMERA multidetector

This second chapter is devoted to provide the main features of the CHIMERA multidetector, by means of which the $^{58}Ni+^{48}Ca$ reaction has been performed at 25 AMeV of incident energy at the Laboratori Nazionali del Sud in Catania.

2.1 General feature of CHIMERA multidetector

CHIMERA is a **C**harged **H**eavy **I**on Mass and **E**nergy **R**esolving **A**rray arranged in a 4π configuration around the target. It consists of 1192 detector modules (Si-CsI(Tl) telescopes) distributed on 35 rings: 17 of them compose the sphere, of 40 cm radius and the other 18 the so called "forward part", being located in front of it in a cylindrical geometry along the beam axis. The whole apparatus has a total length of about 4 m, as illustrated in fig. 2.1a), b), and is designed to operate in a vacuum chamber [PAG95].

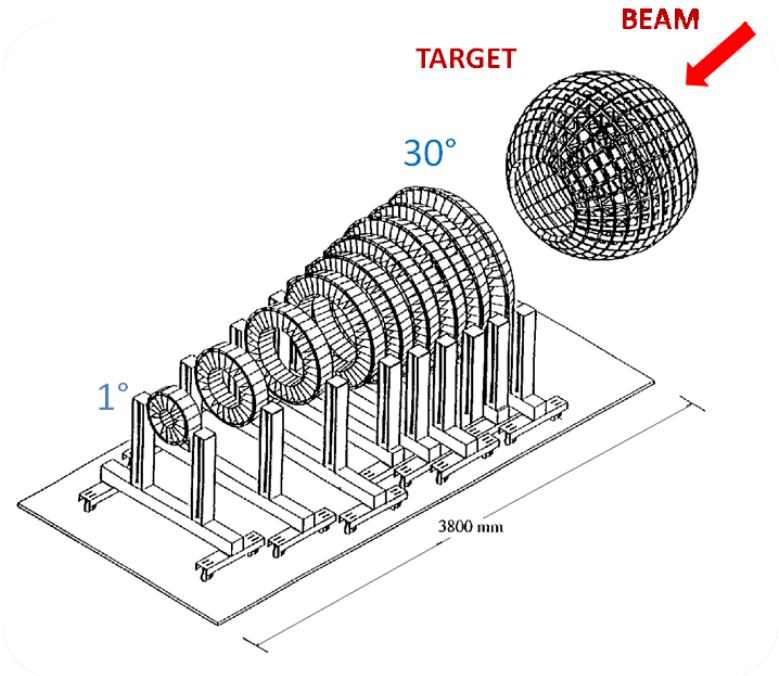

Figure 2.1a Schematic picture of the CHIMERA apparatus.

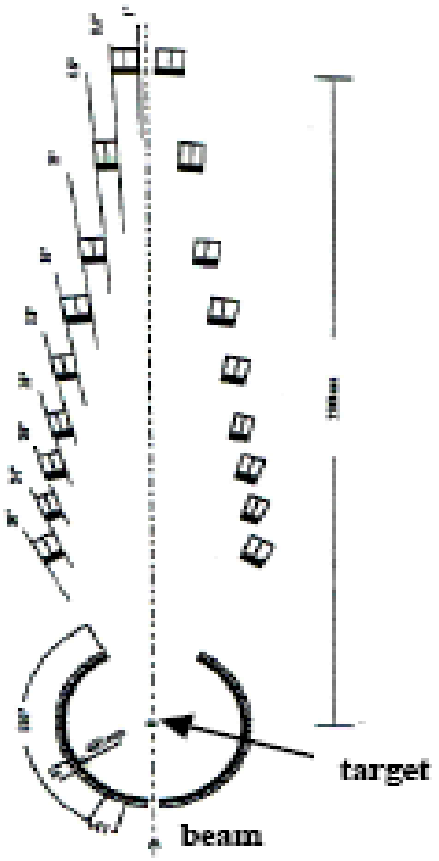

Figure 2.1b Schematic view of longitudinal section of CHIMERA multidetector

Polar angle range between 1° and 30° is covered by the forward part of the apparatus (see fig.2.2), where the above cited 18 rings are grouped in couples and supported by 9 wheels placed at a distance from the target varying from 350 to 100 cm with increasing polar angle. Each wheel is divided into 16, 24, 32, 40 or 48 trapezoidal cells, depending on its polar coordinate, containing each one a detector module, or telescope.

The remaining angular part, between 30° and 176°, is instead covered by the sphere (see fig.2.3), whose 15 forward (according to the beam direction) rings are segmented into 32 cells hosting the telescopes, while the 2 backward ones are segmented into 16 and 8 cells.

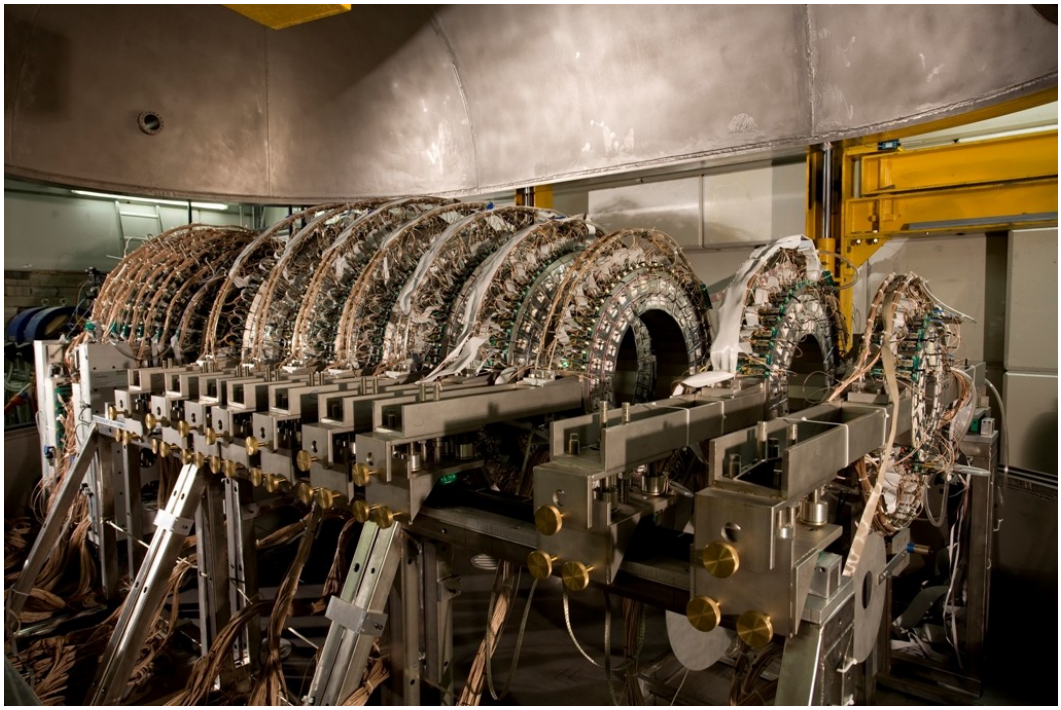

Figure 2.2 Photography of the forward part of the CHIMERA apparatus.

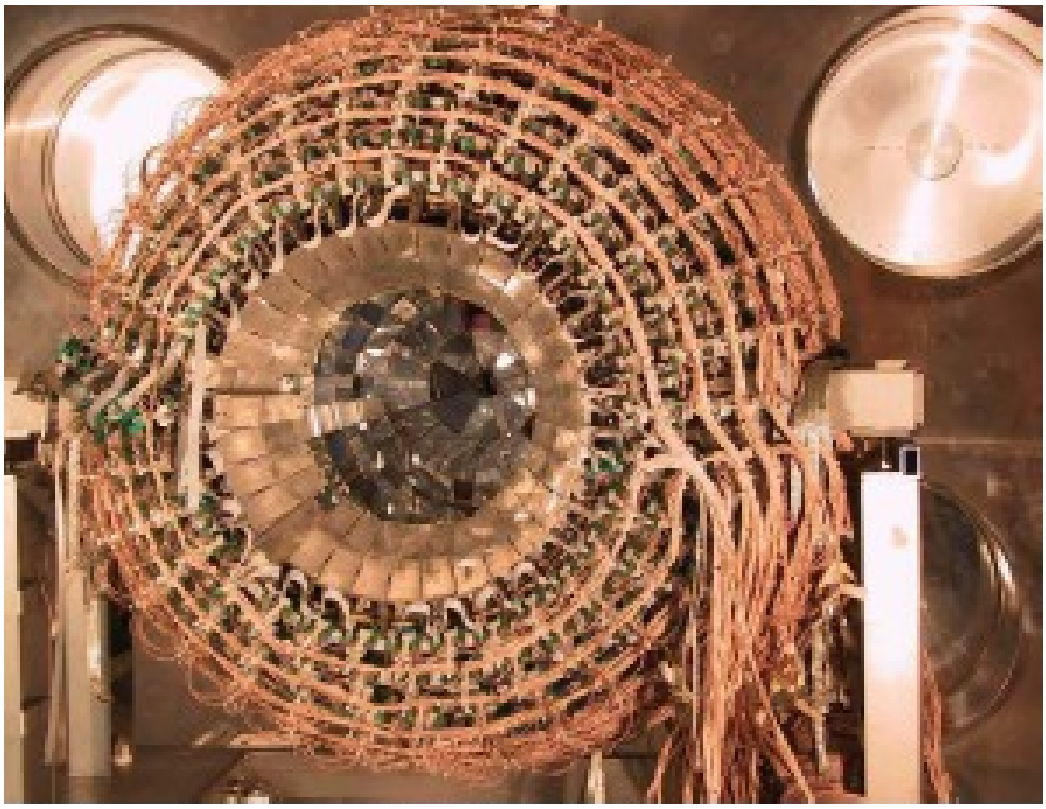

Figure 2.3 Photograph of the sphere of the CHIMERA multidetector.

In Table 2.1 the main characteristics of the multidetector geometry are listed.

The large number of telescopes and the geometrical configuration give to CHIMERA a high granularity, thus reducing the multi-hit probability, and a high solid angle coverage, about 94% of 4π considering the beam entrance and outgoing holes and the detector and target frames [AIE95, PAG95, PAG01, PAG04].

These features, together with the high performances of the identification methods and low energy detection trigger threshold make the multidetector a very useful instrument for complete event reconstruction.

Wheels	Ring	Dist. (cm)	Θmin (deg)	Θmax (deg)	Modules	ΔΦ(deg)	Surface (cm^2)	ΔΩ (mSr)/(singlemodule)
1	1 2	350	1.0 1.8	1.8 2.6	16	22.5	16.3 25.6	0.13 0.21
2	3 4	300	2.6 3.6	3.6 4.6	24	15	22.2 29.3	0.25 0.33
3	5 6	250	4.6 5.8	5.8 7.0	32	11.25	23.3 28.6	0.37 0.46
4	7 8	210	7.0 8.5	8.5 10	40	9	24.2 29.1	0.55 0.66
5	9 10	180	10 11.5	11.5 13	40	9	24.8 28.2	0.77 0.87
6	11 12	160	13 14.5	14.5 16	48	7.5	20.8 23.1	0.81 0.90
7	13 14	140	16 18	18 20	48	7.5	26.2 29.1	1.34 1.49
8	15 16	120	20 22	22 24	48	7.5	23.6 25.7	1.64 1.78
9	17 18	100	24 27	27 30.0	48	7.5	29.5 32.7	2.95 3.27
10	19	40	30.0	38.0	32	11.25	24.5	15.33
11	20	40	38.0	46.0	32	11.25	29.3	18.34
12	21	40	46.0	54.0	32	11.25	33.6	21.0
13	22	40	54.0	62.0	32	11.25	37.2	23.25
14	23	40	62.0	70.0	32	11.25	40.1	25.05
15	24	40	70.0	78.0	32	11.25	42.2	26.35
16	25	40	78.0	86.0	32	11.25	43.4	27.15
17	26	40	86.0	94.0	32	11.25	43.9	27.42
18	27	40	94.0	102.0	32	11.25	43.4	27.15
19	28	40	102.0	110.0	32	11.25	42.2	26.35
20	29	40	110.0	118.0	32	11.25	40.1	25.05
21	30	40	118.0	126.0	32	11.25	37.2	23.25
22	31	40	126.0	134.0	32	11.25	33.6	21.0
23	32	40	134.0	142.0	32	11.25	29.3	18.34
24	33	40	142.0	150.0	32	11.25	24.5	15.33
25	34	40	150.0	163.0	16	22.50	56.7	35.45
26	35	40	163.0	176.0	8	45.00	50.9	31.79

Table 2.1 Relevant geometrical features of the CHIMERA detectors.

2.2 Basic detection module of the CHIMERA apparatus

As cited above, CHIMERA consists of 1192 basic modules, each one of them is a telescope made of a 300 μm thick Silicon detector (Si) followed by a Caesium Iodide Thallium activated scintillation detector (CsI(Tl)).

The thickness of such crystals decrease with increasing of the polar angle where they are located, going from 12 cm in the angular range between 1° and 24° to 3 cm for angles between 142° and 176°.

The scintillator is then coupled to a photodiode that converts the light information in a current signal (fig 2.4).

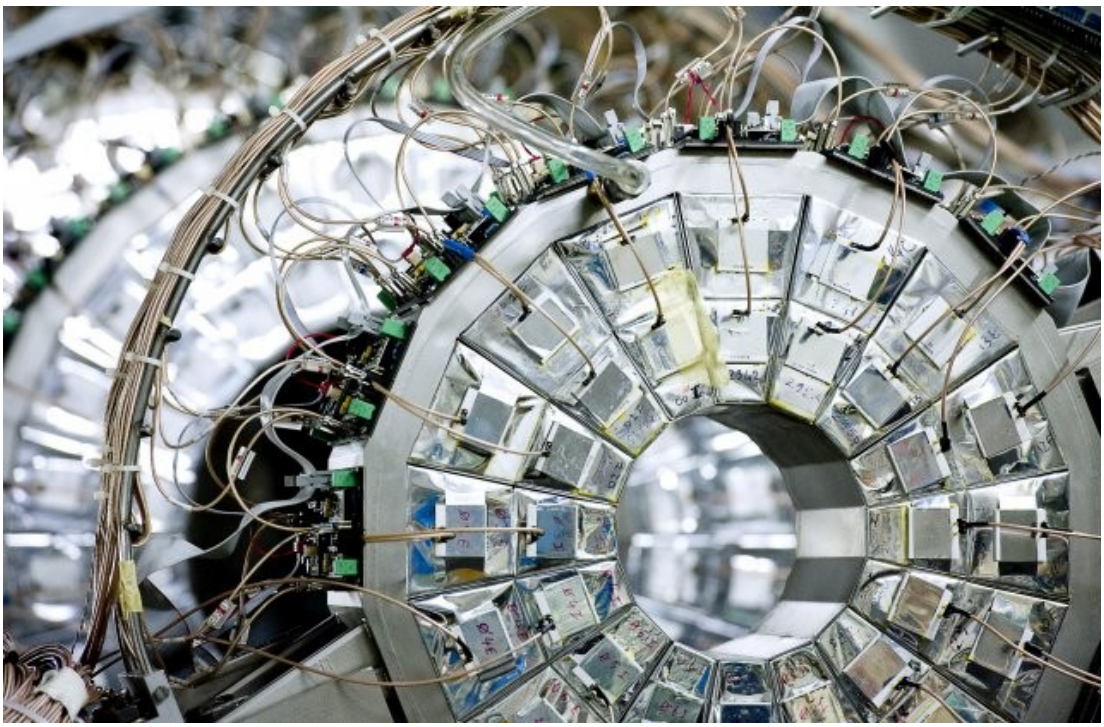

Figure 2.4 Photography of the final configuration of the CHIMERA's modules.

2.2.1 The first stage of telescope: the Silicon detector

Thank to its good energy resolution, its high density (2.33 g/cm3), the low energy needed to create an electron-hole pair (3.6 eV with respect to 30 eV in gases), its fast

signal collection (10 ns in 300 μm of thickness) and its good time resolution, the silicon is a very widely used material for nuclear physics detectors.

The CHIMERA's silicon detectors have a trapezoidal shape and were made by using the planar technology [AIE95, AIE97, AIE99, KEM84] in order to reach a well defined detector thickness (500 Å) and very sharp active zones (fig.2.5).

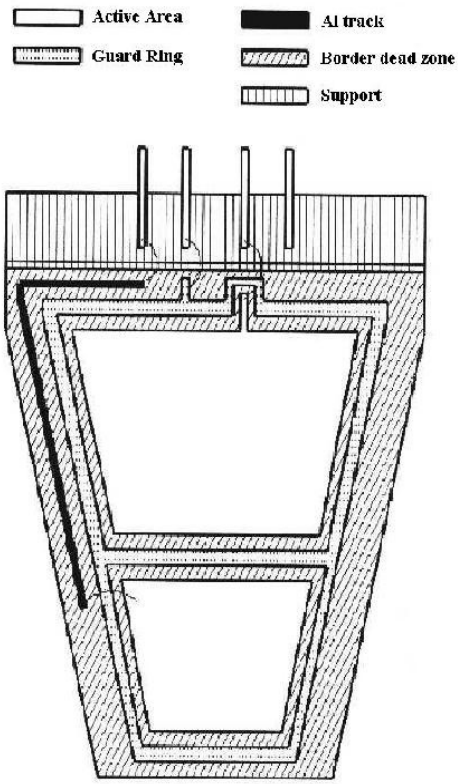

Figure 2.5 Schematic picture of a silicon detector located in the rings of CHIMERA.

Finally, both the front and rear faces of the detector are covered by a 300 Å aluminium layer in order to improve the electric contacts: this trick could affect the energy resolution, due to the introduction of a dead layer, but the rise time becomes nearly independent of the impact point of the detected particle, so that the overall timing performance is enhanced [RIJ92].

Moreover, the timing is improved by means of an high electric field inside the detector.

The junctions are oriented towards the target, in this way the highly ionizing particles that lose all their energy in Silicon are stopped in the region at highest value of electric field, where the collection of the ionization charges is maximum.

In order to work at high value of electric field, it is necessary to completely deplete, or over-deplete, the detector, and for this reason the bias voltage usually applied is larger (typically 30% more) than the nominal value. However, caution is required to compensate the effects due to inverse current.

The resistivity of the silicon detectors ranges between 4000 a 7000 Ωcm while their capacitance varies from 500 to 2200 pF depending on the surface: the geometry of each detector changes indeed according to the position in the device, while the thickness is the same and it was chosen in order to optimize the combined technique ΔE-E + TOF that will be explained in next chapters. In particular, it is possible to distinguish two classes of Silicon detectors in CHIMERA, depending on the number of active zones: the members of the first one, located on the sphere, are simple pad detector, while the second ones, on the forward part of the multidetector ($\theta < 30°$), are characterized by the presence of two active zones that work independently one.

In the wheels (that compose the forward part of the apparatus) both the two active zones are surrounded by a guard ring located 50 μm away in the dead zone (due to the planar technology) of the edge of the detector. Such a ring, besides reducing the inverse current on the surface, bounds a uniform electric field inside the detector close to the edge, avoiding possible edge effects on the output signal [ADE11, AIE97].

A thin aluminium strip, placed near the guard ring, allows taking the signal directly from inside the detector, so avoiding the use of external components that could increase the dead thickness. A similar guard ring surrounds the single pad in the sphere's detectors.

Each silicon slice is finally fixed on a PCB frame that ensures the electric connections and works as mechanical support.

2.2.2 The second stage of telescope: the CsI(Tl) crystal

In the CHIMERA telescope the second detection stage is realized by means of Caesium Iodide Thallium activated crystals CsI(Tl): these scintillators are used to measure the residual energy of particles that punch through the silicon detector [AIE96].

In the framework of the band theory for solids, an inorganic crystal is characterized by a valence band and a conduction one, with a "forbidden" region between them, a gap that cannot be occupied. The doping technique of these materials with activators like Thallium causes the formation of energy levels inside the gap, which can therefore be employed. The passage of the radiation can cause the jump of an electron from the valence to the conduction band, thus creating a free electron-hole pair; the hole can meet an activator atom and ionize it, so that the free electron of the pair can be captured by such ionized atom and can therefore undergo a transition from an excited state to the ground state, resulting in emission of a photon.

This light radiation forms the output signal from the scintillator, consisting of a fast and a slow component whose decay constants depend on the specific energy loss of the incident fragments, and therefore on their energy, charge and mass.

The CsI(Tl) crystals are chosen as second stage detectors because of their high density (4.51 g/cm3, against the 3.67 g/cm^3 of NaI or ~1 g/cm^3 of organic scintillators), so that their high stopping power allows to reduce the thickness needed to stop the high energy charged particles and fragments.

Moreover CsI(Tl) scintillators are characterized by relatively low cost, simple handling, a good resistance to radiation damage and external factors and good light output performance when coupled with a photodiode or a photomultiplier, and offer the ability to make an isotopic discrimination through the Pulse Shape Discrimination (PSD) technique, which will be described later. A disadvantage of these scintillators is the non-linearity (at low energies) in light response that is therefore not directly proportional to the deposited energy, depending on the nuclear species of the fragment and on its ionizing power.

The shape of the crystals mounted in CHIMERA is a pyramid trunk with a trapezoidal base where the dimensions of the front surface are the same of the silicon detectors and depend on the position in the device (see Table 2.1); the backward surface is bigger than the front one, depending on the thickness of the crystal. The thickness of the crystals, in the different rings of CHIMERA, is shown in Table 2.2, together with the maximum energy of proton stopped in the detectors.

All the crystal faces are sanded (in order to reduce the light dispersion) except the back one, used for the light collection, which is polished. In order to optimize such a collection, the crystals are wrapped, on all their lateral and rear faces, in a 150 μm thick Teflon layer and coated with a 50 μm thick aluminium foil; the front face coverage is instead a 2 μm reflecting foil of aluminized Mylar [AIE96].

Finally, the CsI(Tl) crystals are coupled with photodiodes (PD), favourites with respect to photomultipliers mostly for their low operating voltage (so low power dissipation), their simple handling and compact assembly under vacuum (see fig.2.4). CHIMERA photodiodes, manufactures by Hamamatsu Photonics, are 300 μm thick with an active surface are of 18×18 $mm^2$and are located into a ceramic support with the front side (corresponding to the light entrance hole) protected by a thin window of transparent epoxy.

RING	Theta	Thickness (cm)	E_{max}^{proton} (MeV)
1-16	1° - 24°	12	190
17-18	24° - 30°	10	160
19-22	30° - 62°	8	140
23-25	62° - 86°	6	120
26-28	86° - 110°	5	95
29-32	110° - 142°	4	95
33-35	142° - 176°	3	90

Table 2.2 Thickness of the CsI(Tl) crystals for different rings; E_{max} represents the maximum energy of a proton stopped in the detector at 1.5 - 2 cm before the photodiode (such a distance is relevant in order to ensure an impact point independent energy measurem

2.3 The electronic chains

The output signals from the Silicon detector and from the photodiode are processed by two different electronic chains, which convert them so that they can be read by the acquisition system. A typical experiment performed by means of the CHIMERA apparatus requires that the electronic meets some requirements, as a large dynamic (from MeV ÷ GeV), a good timing in order to ensure a resolution of about 1% in velocity measurements through the TOF technique, a low power dissipation under vacuum, a good energy resolution and a simple coupling with other experimental devices.

In order to reduce electronic noise and signal losses in parasitic circuits, which strongly affects the energy resolution, the preamplifiers (PAC), that constitutes the first stage of the electronic chains both for silicon and Caesium detectors, are placed inside the vacuum chamber, on some motherboards. The motherboards are located on the external surface of the wheels for the detectors in the forward part of CHIMERA and on the top of the metallic baskets containing the telescopes for that ones in the sphere.

Each telescope needs two PACs, one for the silicon and the other for the photodiode, so the motherboards in the forward part contain four PACs: two for the internal telescope and two for the external one; while those in the sphere have only two preamplifiers, corresponding to only one telescope. All the motherboards are cooled by using a cooling plant for the stability of the electronic against the power dissipation.

The power supply systems for detectors and PAC, together with the other stages of electronic chain, are located outside the vacuum chamber.

2.3.1 The Silicon detectors' electronic chain

The electronic chain of Silicon detectors used for the present experiment follows the steps illustrated in fig. 2.6a, briefly described below.

1. The **Charge Preamplifier** (PAC):

   Designed to ensure good timing measurements, it's the first stage in processing signal from Silicon detector providing a first amplification: it integrates the signal giving a charge output independent of the detector capacitance and proportional to the charge produced by the detected particles.

   In order to control the electronic stability and carry on the calibration operations, each preamplifier is provided with a test input which accepts signals from a pulse generator.

   The output is a single negative fast signal, with time and energy information, with a decay time of ~ 200 μs and a rise time of ~ 50 ns for input capacitance of ~ 700 pF.

   The PAC sensitivity changes with changing of the polar angle: in the forward part (1° ÷ 30°), where the more energetic particles are expected, the sensitivity is 2 mV/MeV, while in the sphere (30° ÷ 176°) it is 4.5 mV/MeV. In both cases the output signal is lower than 4 V (when adopted to 50 Ω), which represents the maximum value accepted by the following step: the amplifier.

2. The **Amplifier** (AMP):

   The used amplifier is a CAMAC 16 chs bipolar model. Each channel, besides amplifying the signal, provides two analogical output signals: a negative front bipolar one as energy output and a unipolar temporal one obtained by differentiating to 100 ns and integrated to 20 ns. It is also possible to use the multiplex output to control the signals.

   Such two signals, the energy and the time, have to be processed by a Charge Digital Converter and a Constant Fraction Discriminator respectively.

3. The **Charge Digital Converter** (QDC):

   The charge digital converter is used to process the amplified energy signal by double charge encoding: the High Gain (HG) and the Low Gain (LG) coding. In the first case an 8× amplification factor is applied and a good energy resolution can be reached also for low energy signals.

4. The **Constant Fraction Discriminator** (CFD) and the **Time Digital Converter** (TDC):

   Concerning the time information in the electronic configuration at the time of the $^{58}Ni + ^{48}Ca$ experiment (slightly changed in more recent times, as later explained), the signal from the amplifier was read by a high resolution constant fraction discriminator on a 16 channel CAMAC module. Each discriminator, still operating in some modules of the multidetector, but not in the whole device, is characterized by an input signal with 50 Ω impedance and maximum amplitude of -5 V, a delay of 20 ns, a typical fraction of 30 %, a variable discriminator threshold from 1 to 256 mV in step of 1 mV and an automatic set of the walk. That way, in such a configuration, the discriminator provides two output analogical signals: a prompt one used as a start signal for a time digital converter, and a delayed one that, together with an OR output signal, is sent to the trigger control system.

   The stop signal is then provided by the cyclotron radiofrequency and sent to the same TDC that gives an output signal proportional to the temporal distance between the start and the stop signals.

Recently the pulse shape technique, not yet used for the present experiment, was improved also for silicon detector, with substantial changes in the electronic chain (for silicon detectors from the third ring), as it possible to notice in the red box in fig. 2.6b: since for such a technique it's important to measure the rise time of the time signal from the amplifier, a new configuration was adopted, with two different discriminators characterized by different constant, 30% and 80%. Such two CFDs process two copies of the same timing signal from the AMP and send their output signals to two different TDCs. Each TDC performs a comparison between such signal (from the related CFD) and that one coming from the Cyclotron (that also in this case provides the start reference). Finally, by means of the difference between the two TDCs' outputs, $T_{30\%}$ and $T_{80\%}$ respectively, it's possible to obtain the rise time of the temporal signal from the AMP.

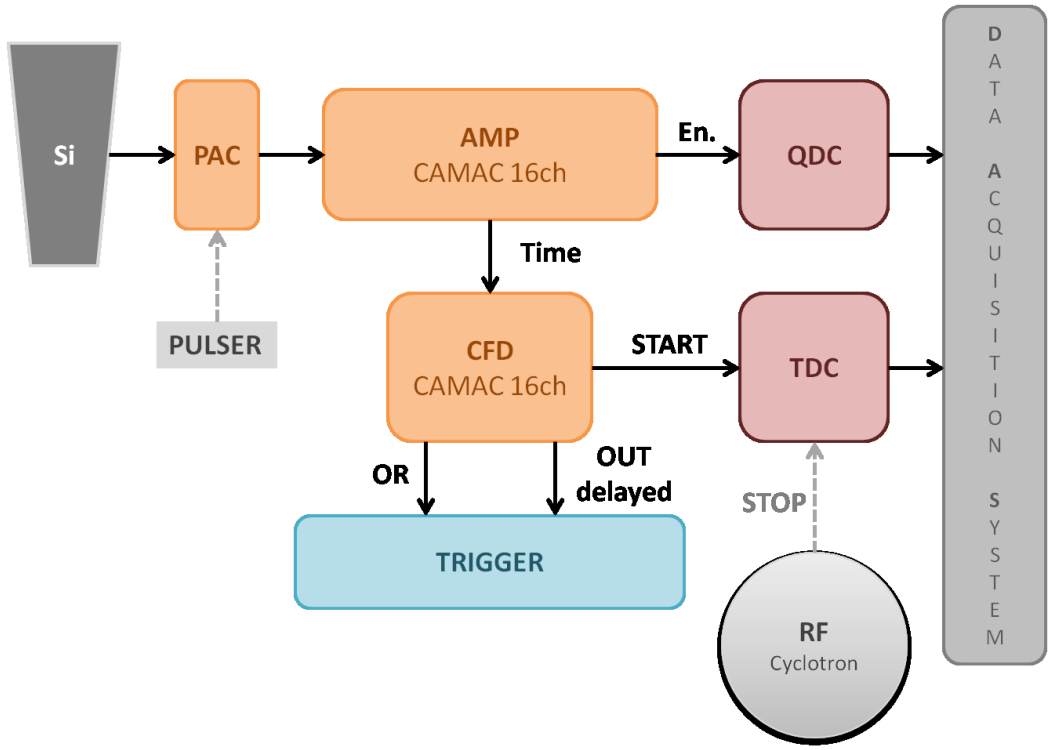

Figure 2.6a Simplified picture of the silicon detectors' electronic chain used for the 58Ni+48Ca experiment.

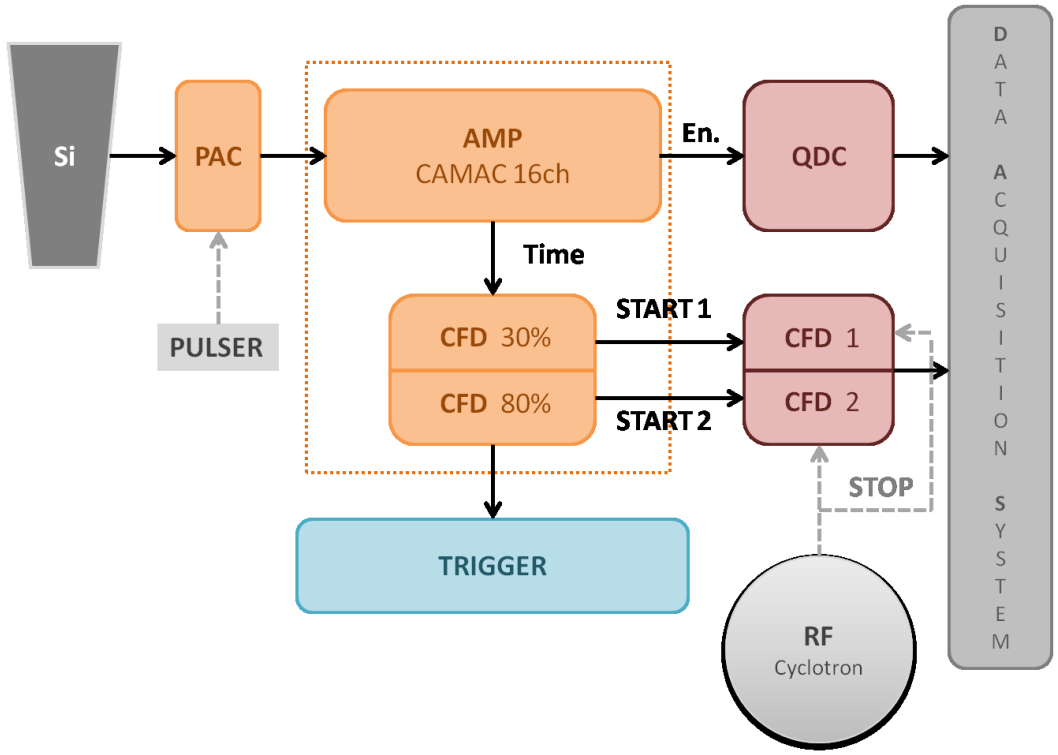

Figure 2.6b Upgrade of the silicon detectors' electronic chain (in dashed box) for the pulse shape technique.

2.3.2 The CsI(Tl) scintillators' electronic chain

The Caesium Iodide electronic chain is composed as illustrated in fig.2.7 and below explained:

1. The **Charge Preamplifier** (PAC):

   The light signal from the Caesium crystal, collected by the relative photodiodes, is firstly processed by a charge preamplifier similar to that used for the silicon detectors', being the photodiode just a thin silicon layer, but with some differences like a sensitivity of about 50 mV/MeV.

   The output signal, whose rise time can reach values of the order of the μs, is then sent to a unipolar amplifier.

2. The **Amplifier** (AMP):

   The amplifier has the task to amplify and shape the preamplified signal. The amplifiers used in CHIMERA have a variable shaping time (0.5, 1, 2, 3 μs) and are assembled in a 16 channel NIM module. They are different to those used for Si detectors, and they have a double output in energy for each channel with different gains (the higher one is 10 times the lower one). Besides they give a fast timing output with a gain equal to 15.

5. The **Charge Digital Converters** (QDCs) and the **Stretcher**:

   The two well shaped energy amplifier outputs follow two separate lines: the higher one is sent to a QDC for the integration of the so called "slow" CsI(Tl) signal component, while the lower one is stretched by a 48 channel module and then sent to another QDC for the integration of the "fast" signal component.

To collect and store data coming from both Silicon and Caesium electronic chains and to allow a fast overview of the progress of an "in fieri" experiment, a data acquisition system is needed: detailed information about the CHIMERA Data Acquisition System can be found in [AIE98, AIE98b, AIE98c, AIE00, AIE00b, ALD01, ALD02b], while the Data Analysis Software and the Trigger System in [RUS06].

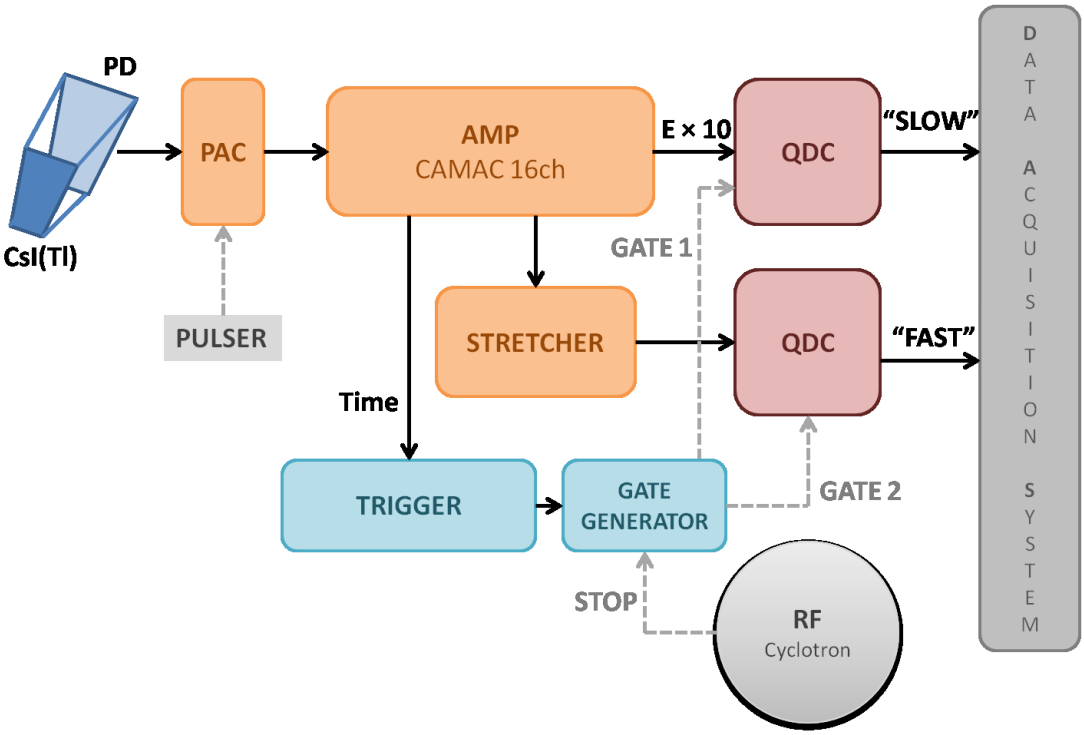

Figure 2.7 Schematic picture of the CsI(Tl) crystals' electronic chain.

2.4 The identification techniques

The CHIMERA multidetector is able to directly measure energies and velocities of particles stopped in Silicon or Caesium detectors and to identify them in charge and mass [PAG01, PAG04, PAG04b].

The energy measure is based on the physical process by which a charged particle that crosses a material loses part of (or the whole) its energy, while the velocity measurement is performed by the time of flight technique.

The dependence of the energy loss on the atomic number and mass of the particle and the contemporary measurement of the energy (kinetic energy) and velocity allows finally the identification in charge and mass of the detected particles.

The complete identification of particles is made, in CHIMERA multidetector, by using the telescopes discussed in the previous paragraphs, while energy thresholds, for charge identification of particles stopped in the scintillators, that approximately range from 6 AMeV for ^{7}Li to 12 AMeV for ^{16}O. The velocity measurements

instead, since the first stage of each telescope consists of a Silicon detector with a detection threshold of about 1 MeV, are possible for all charged particles with energy value above such energy. Since the velocity measurement is determined by time and distance measurements, its resolution varies with changing of detector position in the device: in particular it goes from 0.7% for the most energetic fragments detected in the first ring up to 10% for the less energetic ones detected in the sphere.

In the following the three employed identification techniques will be discussed.

2.4.1 The ΔE–E technique:

Such technique is used in CHIMERA to perform charge and mass identification of light charged particles (Z<3) with energy values between 6 and 30 AMeV and only charge identification for fragments (Z≥3) with energy greater than ≈ 12 AMeV.

As already cited, a charged particle that crosses a material layer loses energy through inelastic collisions with atomic electrons and ionization of the target nuclei: the average energy lost per unit path, called "stopping power", is indicated by the symbol $^{dE}/_{dx}$ and depends, according to the following approximation of the Bethe-Block formula, on charge, mass and energy of the incident particle:

$$\frac{dE}{dx} \propto \frac{AZ^2}{E}$$

Eq. 2.1

where A, Z and E correspond to the atomic mass, the atomic number and the kinetic energy of the incident particle respectively.

If the particle, in our case the reaction fragment, is energetic enough to completely punch through the detector Silicon thickness Δx (280 μm), and if the detector response goes linearly with the deposited energy, the output signal, codified by the High-Gain and Low-Gain QDC, has an amplitude proportional to:

$$\Delta E = \frac{dE}{dx} * \Delta x$$

Eq. 2.2

where Δx is the crossed material's thickness.

Then, if the incident particle is stopped in the scintillator, the output fast component signal from this last stage of the telescope is proportional to the residual energy just released in Caesium, E_{res}.

Finally, the sum of such two quantities results in the total kinetic energy of incident particle:

$$E = \Delta E + E_{res}$$

Eq. 2.3

Therefore, combining the two quantities in eq. 2.2 and eq. 2.3 in a ΔE/E scatter plot, it is possible to distinguish several groups of hyperbole's branches: each group corresponds to a Z value and, inside it, each branch corresponds to a different isotope of the same element (see fig.2.8).

So, with such a representation it is possible to discriminate the light incident fragments ($Z \lesssim 10$) in charge and mass, while the isotopic identification is difficult for heavier ones, because of the quadratic dependence of the energy loss on the atomic number.

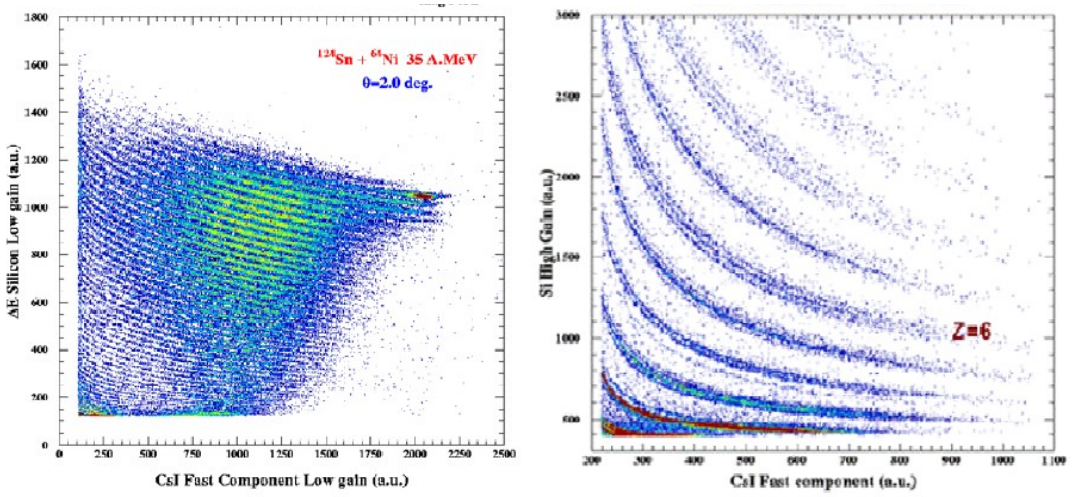

Figure 2.8 ΔE-E scatter plots for the reaction $^{124}Sn+^{64}Ni$ at 35 AMeV. On the left side, corresponding to reaction products detected at θ=2°, it is possible to observe just charge identification. A good isotopic identification is instead observed on the right side [POL05].

2.4.2 The Pulse Shape Discrimination (PSD) technique:

At first, such technique was used in CHIMERA in order to identificate particles stopped in the scintillator, by means of the light signals collected by the photodiodes and sent into the relative electronic chain; from 2008 ta PSD technique is operative also for the silicon detectors, allowing the charge identification of less energetic particles that stop inside the first detection stage: this is the case of the ISODEC experiment, that studies low energy reactions, at 10 AMeV [PIR14].

- PSD in CsI(Tl) crystals:

When reaction fragments punch through th Silicon layer and come into the CsI(Tl) scintillators they excite atoms and molecules in the crystal. Their following deexcitation then produces the light signal collected and converted in an electric pulse by the photodiode.

In the main part of scintillators the light emission is characterized by two components, a fast and a slow one, with two different decay constants, τ_f and τ_s respectively.

Such constants govern the temporal evolution of the emission process, so that the output signal from CsI(Tl) is described by the combination of the two exponential components in the following expression:

$$V(t) = V_1 e^{t/\tau_f} + V_2 e^{t/\tau_s} \qquad \text{Eq. 2.4}$$

where *V(t)* is the signal output amplitude at time *t* and V_1 and V_2 are the light pulse amplitudes for fast and slow components, independent to one another.

The amplitude V_1 increases with increasing of stopping power dE/dx of the incident particles, so depending on their energy, charge and mass, while V_2 is less sensitive to the incident particle species, and it's just on this kind of dependence that the PSD technique is based.

The signal from preamplifier passes through the amplifier where is shaped with a time constant of about 1÷2 μs (see fig.2.7). In this way the slow component of the

signal, with a characteristic time longer than the amplifier formation time, is cut off and so contributes just to the tail of the total signal. Therefore, integrating two different parts of the amplifier's output by means of two different gates shifted in time (fig.2.9a) it is possible to obtain two separated signal with amplitude proportional to the fast and the slow component.

In the CHIMERA electronic system it was chosen to work with a common gate, so the signal from amplifier is splitted in two copies and one of these is sent to a "stretcher module" (as illustrated in paragraph 2.3.2 and fig.2.7) which stretch the signal when it reaches its maximum value. The use of a stretcher avoids delays introduction and "jitter" effects. This stretched signal will constitute the fast part of the signal, being integrated at its stretched maximum, while the second one, unchanged, will be integrated in correspondence of its tail, and thus will give information about the slow component of scintillator signal, as shown in fig.2.9b.

Such two "fast" and "slow" signals are finally read by the acquisition system and displayed in a scatter plot on the y and x axis respectively, as shown in fig.2.10. As above mentioned, the fast component of the signal brings information about the nuclear properties on the incident particles, so that in the scatter plot it's possible to distinguish several lines corresponding to different light particles and their isotopes (p, d, t, ^{3}He, ^{4}He, ^{6}He, Li, and less well separated lines for heavier fragments).

In the present analysis this PSD technique has not been included, just slightly affecting the global reconstruction of the reaction patterns.

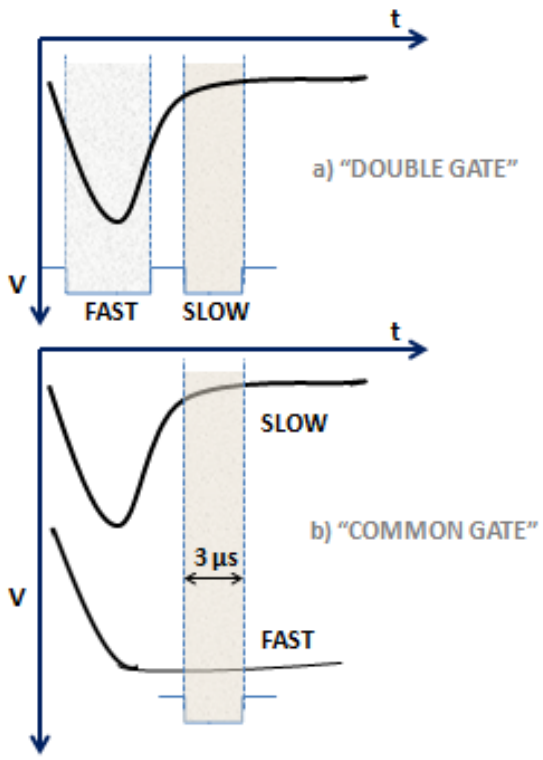

Figure 2.9 Integration of the "FAST" and "SLOW" components of amplified signal using a) the double gate and b) the common gate method.

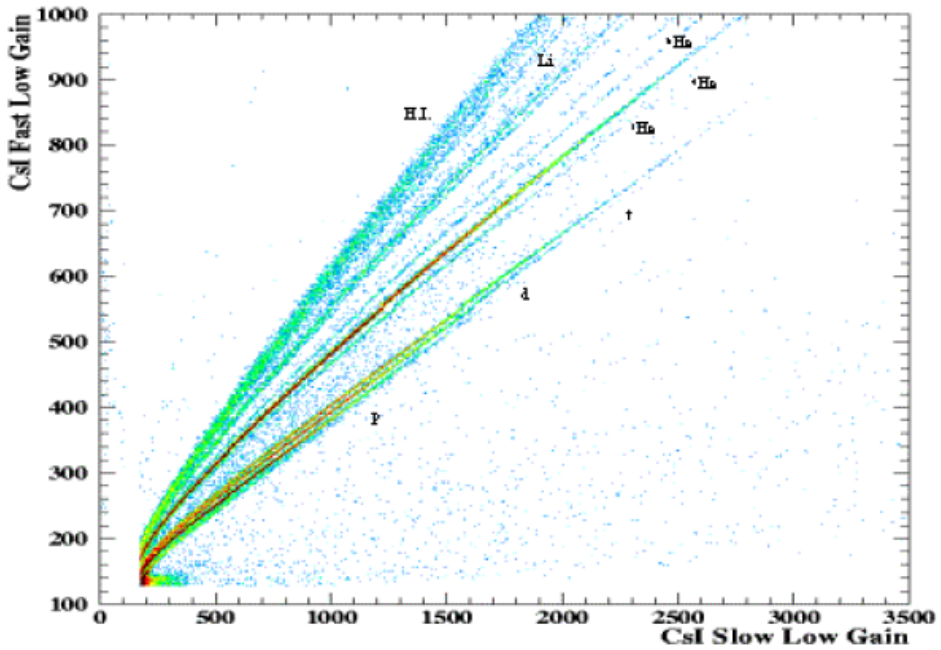

Figure 2.10 Fast-Slow components' matrix relative to a crystal of CsI(Tl) for the reaction ^{124}Sn + ^{64}Ni a 35 A MeV.

- PSD in Silicon detectors:

In 2008 the CHIMERA multidetector was upgraded with the introduction of the pulse shape technique implemented for Silicon detectors.
Since 2001 several different tests on feasibility of PSD in CHIMERA Silicon detectors have been performed both at the Tandem and Cyclotron accelerator in dedicated as well as parasitic experiments.

The extension was finally proposed in 2004/2005 with a detailed discussion of some experimental results obtained mainly in experiments with ^{16}O e ^{19}F light ions beams at energy of 100 MeV [PAG05], where the charge identification were obtained by looking at the rise time of the detector signals as a function of the detected particle energy [ALD04, ALD04b, ALD05, POL05, POL05b].

Since such technique in silicon was not yet operative in the present data acquisition, we give in this section just the essential information, referring to the bibliography for details.

Since the first years of experimentation with silicon detectors in nuclear physics (early 60s) it has been pointed out that the pulse shape of the signal generated by the ionization of a charged particle in silicon depends both on the atomic number Z and mass A of such incident particle [AMM63, ENG89].

This dependence is well detectable for ions completely stopped in the detector. Instead, for particles that pass through the silicon step (which acts in this case as a transmission detector), the shape of the signal is, in contrast, mostly independent on the charge.

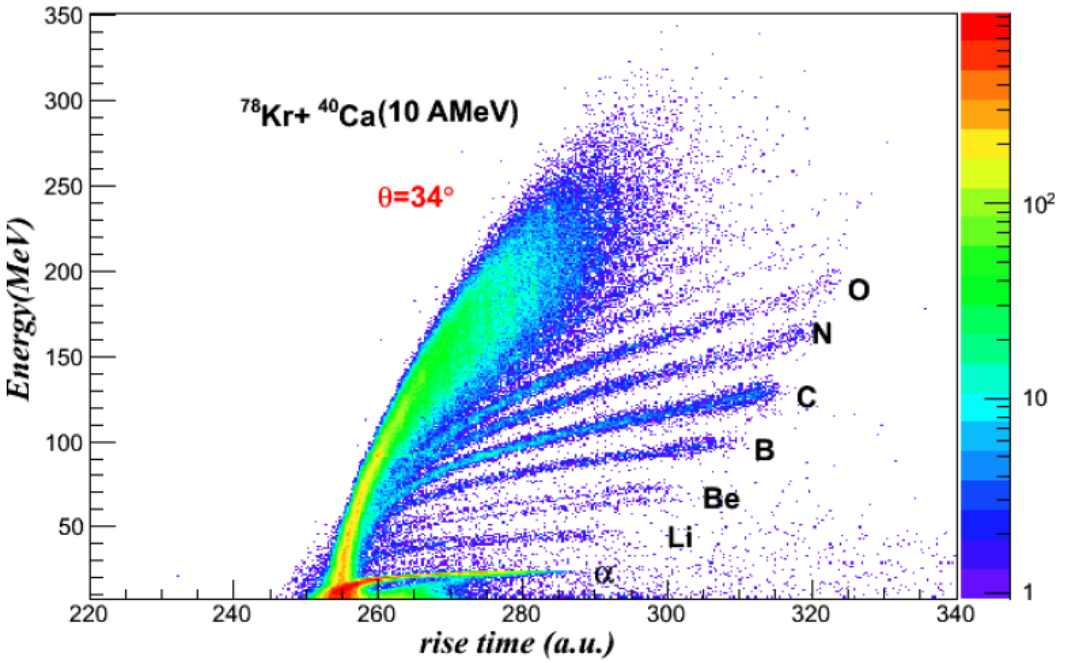

Figure 2.11 Energy vs. rise time for fragments stopped in Silicon detectors of ring 10 in the ^{78}Kr + ^{40}Ca reaction.

The reason of the Z, A dependence lies in the collection time of the negative (conduction electrons) or positive (valence holes) charges that are generated along the ionization track, that determines the rise time of the current output signal.

At a fixed value of incident energy the path taken in the silicon by the particle decreases with increasing of its charge; in addition, decreasing the energy along the ionization track, as it's known, the incident ion undergoes a partial recombination process of the electric charge so determining the formation of the so-called Bragg peak, with the downfall of the specific energy of the particle at the end of the track.

The electronic signal collected in the polarized electrodes has a rise time which increases with increasing of ion charge, regardless of its energy.

Just this dependence is the basis of the charge identification of ions stopped in Silicon.

It is also important to notice that the simoultaneous use of TOF and PSD techniques has reduced to few AMeV the energy thresholds for a full charged particles isotopic identification.

An example of charge identification for fragments stopped in silicon detector, in the ^{78}Kr + ^{40}Ca at 10 AMeV reaction, obtained by using such technique is shown in

fig. 2.11: it is also possible to distinguish two different lines corresponding to the isotopic separation of ^{7}Be and ^{9}Be.

2.4.3 The Time Of Flight (TOF) technique:

For reaction products that are stopped in silicon detector the mass identification is performed by means of the time of flight technique [PAG01, PAG04, LANZ04].

Such technique uses two temporal signals, one coming from the 30% Constant Fraction Discriminator (see the Silicon electronic chain in fig. 2.6a,b) that acts as start signal and the second given by delayed Reference Signal (RF) delivered by the super conducting cyclotron, that provides the stop signal. Thank to the good timing of the pulsed beam of the cyclotron it is possible to reach time resolution of about 0.8 ns.

Such two start and stop references are sent in input to a TDC (fig. 2.6) that gives as output a digital value proportional to the time distances between them, t_{ch} (where the symbol *ch* indicates the channel number). So we could conclude that this value is the TOF, but it's very important to consider that this measured difference time includes the true TOF that the particles takes to arrive in the detector, but also the time delays associated with cables and cyclotron phase, as well as the pulse delay in the silicon detector and the CFD walk effects. All such additional terms are taken into account by inserting a constant, t_0, that depends on the hit detector and on the electronic chain's features. In this way, the true time of flight can be expressed as:

$$TOF = t_{ch} - t_0$$

Eq. 2.5

Therefore the time calibration needs the accurate determination of this t_0 parameter.

Moreover, also the TDC conversion factor α (ps/ch) must be considered, whose typical value is about 250 ps/ch: under the simple but realistic assumption of a linear response function of the TDC the TOF can be expressed by the linear expression:

$$TOF = \alpha * (t_{ch} - t_0)$$

Eq. 2.6

Finally, using the simple relation $= {}^{d}/_{TOF}$, where d is the flight base, it is possible to measure the velocity of all the fragments that hit the detector (also for the ones that punch through the first detection stage), while, just for the ones that are stopped and so lose all their energy in the silicon layer, by means of the classical kinetic energy formula, it's also possible to measure the mass M:

$$E = {}^{1}/_{2}\,Mv^2 = {}^{M}/_{2} * {}^{d^2}/_{TOF^2} \Rightarrow M = 2E\,{}^{TOF^2}/_{d^2} = \frac{2E[\alpha * (t_{ch} - t_0)]^2}{d^2}$$

Eq. 2.7

The energy E of particles is provided by the AMP output signal of the Silicon electronic chain.

CHAPTER 3

Looking for the most central collisions:

A Shape Analysis

In this section I would like to briefly introduce the $^{58}Ni + ^{48}Ca$ reaction at 25 AMeV, performed some years before the present PhD thesis, and to show the method adopted for the centrality selection, its results, and the scientific motivations that have driven toward such a choice.

The reaction cited above is a part of an experimental campaign carried out by the ISOSPIN and NUCL-EX collaboration in 2003-2008 that aimed at the systematic study of the liquid and liquid-gas coexistence region with new generation devices like an upgraded version of the GARFIELD + Forward Ring Counter apparatus for low energy reactions at LNL (Laboratori Nazionali di Legnaro) and the CHIMERA multidetector (see chapter 2), located in the LNS of Catania, for the higher energy ones at 25 AMeV and 35 AMeV incident energy.

The experimental campaign followed two main research lines, dynamic and thermodynamic, both requiring high experimental performances in order to reach an accurate measurement of observables related to single reaction products as well as global variables and thus obtain detailed information about evolution from the early to the final stage of the reactions. The complete reconstruction and characterization of the event is indeed a fundamental element for the study of reaction mechanisms like multifragmentation and an accurate identification of the reaction products is necessary in order to study the dynamic and thermodynamic properties of the emitting sources. In this respect, experimental characteristics such as high granularity, low energy thresholds and large dynamic range are required [PAG95, PHA93, SOU06].

For these reasons it was chosen to perform the $^{58}Ni + ^{48}Ca$ reaction, in which an onset of multifragmentation was expected, at the INFN-LNS in Catania by using the 4π multidetector CHIMERA, whose main features have been briefly described in the

previous section: an ion beam of ^{58}Ni was accelerated by the LNS Superconducting Cyclotron at 25 AMeV towards a thin ^{48}Ca target $\left(\rho = 650\,{}^{\mu g}/_{cm^2}\right)$ sandwiched between two very thin carbon foils used in order to reduce oxidation.

As already mentioned, purposes of the experiments were the study of the dynamic and termodinamical aspects of heavy ions reactions in the energy range between 10 and 35 AMeV, with particular interest to the onset of multifragmentation with increasing of the incident energy (strictly related to the liquid-gas phase transition in finite nuclear system), and to the investigation of the thermodynamic features of sources with mass values around 80 amu, formed by central collisions.

The study of the central collisions in the ^{58}Ni + ^{48}Ca reaction, here presented, can provide some relevant information about the formation of such sources as well as the competition between the persistence of low energy processes and a possible onset of the multifragmentation mechanism.

The main advantage to operate with central collisions at lower-intermediate energy lies in the removal of some phenomena just partially understood, that can constitute a "dynamic noise" for thermodynamic studies: one of those is the radial flow, observed in central collisions for incident energies well above ~ 35 AMeV, due to compression of the nuclear matter in the early stage of the collision; another one is, for peripheral collisions, the onset of the mid-velocity emission.

Nevertheless, in chapter one it has been mentioned, besides the great dependence of the reaction mechanisms on the impact parameter, also the difficulty to disentangle such features of the nuclear reactions. Such a difficulty become also greater at the mid-low energies, as in the present reaction at 25 AMeV, just at the beginning of the Fermi energy range, where the presence of processes typical of low energies makes the use of the methods for centrality selection commonly employed at Fermi energies very complicated.

The most relevant example is the applicability of the method based on the charged particles multiplicity M_{CP} (see section 1.3.1), as it will be shown in the next section 3.1. While in the Fermi energy range a relevant feature is indeed the rising of such a multiplicity with centrality [CAV90], due to the typical production of Intermediate

Mass Fragments (IMFs: namely fragments with $3 \leq Z \leq 12$), in the lower range the same M_{CP} observable is not sensitive to the impact parameter.

Moreover, also other methods based on kinematic quantities of the reaction, like that one based on the Total Kinetic Energy Loss (TKEL: see section 1.3.1), require much attention in their application to the centrality selection, mostly for the identification of the most central collisions, as it will be better explained in section 3.2: it will be shown that such method, even if applicable to the present reaction, is just useful to give qualitative information about the centrality classes, but is not able to perform a strict selection of a precise class among them.

3.1 The M_{CP} method applicability at the $^{58}Ni+^{48}Ca$ reaction at 25 AMeV

As mentioned above, the reaction $^{58}Ni + ^{48}Ca$ at 25 AMeV shows strong evidences of the competition between the reaction mechanisms typical of low and intermediate energies, that implies a reduction of the applicability of the M_{CP} selection method. We can become aware of this statement by looking at the evolution of the fragments ($Z \geq 3$) emission trend with increasing of M_{CP}.

For this purpose, in fig. 3.1 the M_{CP} distribution is plotted and divided into four regions corresponding to four consecutive M_{CP} ranges: $M_{CP} < 4$, $4 \leq M_{CP} < 8$, $8 \leq M_{CP} < 12$, $M_{CP} \geq 12$. For each region the correlation between the mass number A and the component of velocity parallel to the beam is then shown in fig. 3.2

Such correlation is built for all detected fragments in complete events: i.e. events where the 70% of total initial charge is detected in the final channel and where the same constraint is applied on the total momentum.

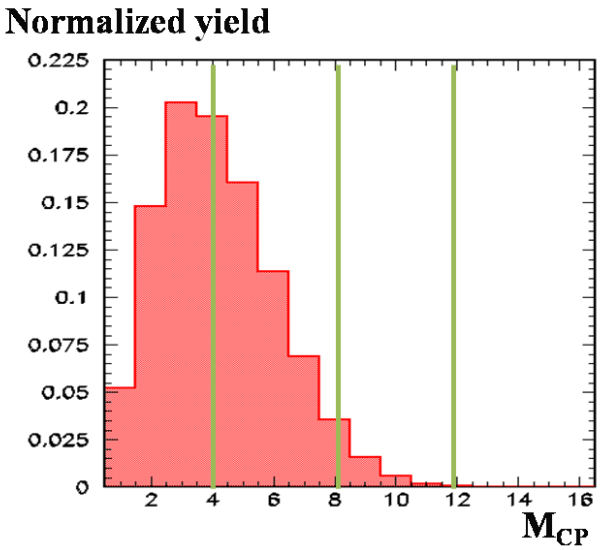

Figure 3.5 Total charged multiplicity distribution.

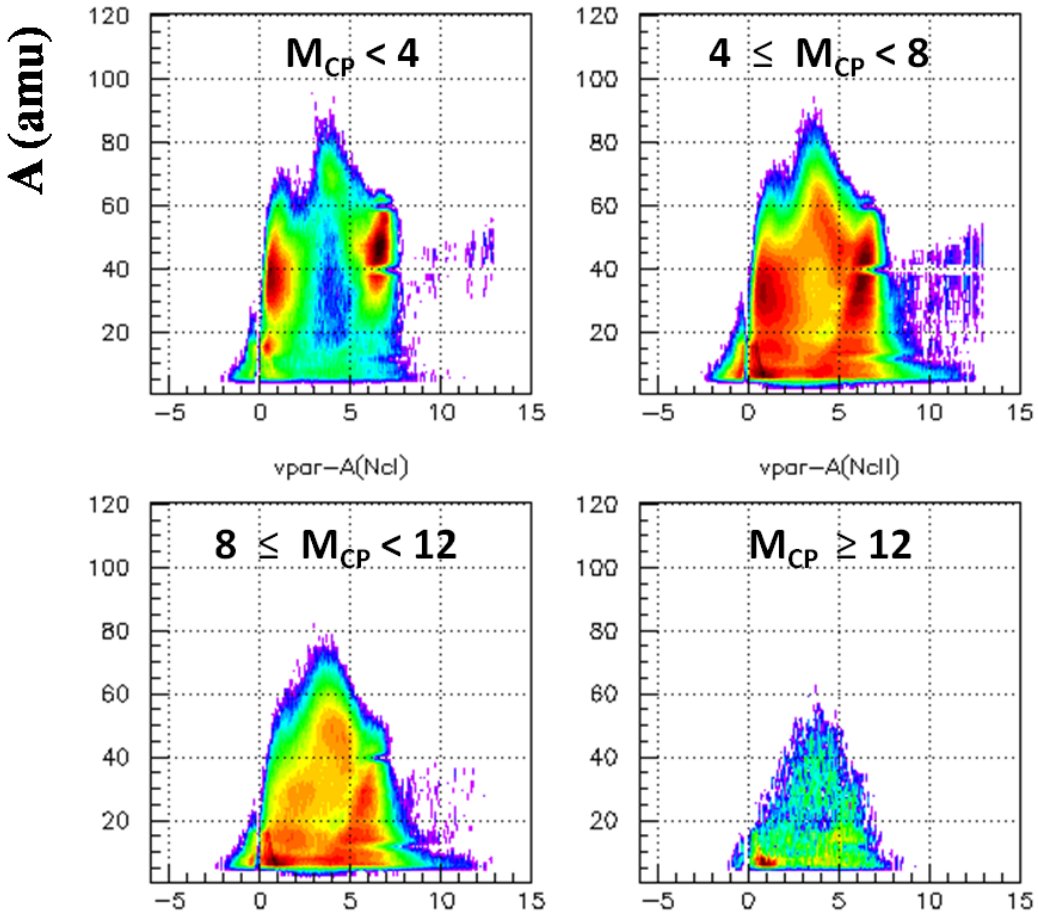

Figure 3.6 Correlation plots between the mass number A and the component of velocity parallel to the beam for all the fragments detected in the four different regions of total charged particles multiplicity.

It could be useful to remind that light particles are not included in the present analysis, except for what concerns their multiplicity, since the information from pulse shape technique from CsI(Tl) crystals has been not included and the upgrade of such technique to the Silicon detectors was not jet available in the time of the experiment.

As anticipated, by looking at fig. 3.2 it is possible to notice that a selection based on imposing several cuts of M_{CP} does not result in a centrality selection: the large number of fragments with parallel velocity close to the projectile velocity ($v_{proj} \cong 6.5$ cm/ns in the laboratory frame) and to the target one (close to zero), still present for high values of charged particles' multiplicity, is indeed indicative of a survival of events with strong memory of the entrance channel of the collision, typically peripheral or semiperipheral events, for any M_{CP} cut.

Moreover, in the middle velocity region centred on the centre of mass velocity ($v_{CM} \cong 3.8$ cm/ns) of all the three M_{CP} windows it is also present a broad component of reaction products with mass larger than projectile or target masses (58 and 48 respectively), reminiscent of the formation of a composite nucleus following the full stopping of the binary interacting system due to central collisions.

Once again, such behaviour underlines the weak sensitivity of M_{CP} observable to the impact parameter for the studied reaction.

In the following we will see that the multiplicity of charged particle is actually a not very significant variable for the investigated reaction, since its distribution will show an almost unchanged shape for any selected ensemble of events.

3.2 The Total Kinetic Energy Loss method

On the other hand, for the same reasons, also other global variables like the Total Kinetic Energy Loss (TKEL) are not completely suitable to give information about the impact parameter, at least when they are used alone: a high value of energy dissipation is indeed characteristic of central collisions both in intermediate and low energy ranges, but also of deep inelastic peripheral ones at low energy, whose memory is still present in the reaction.

What would differentiate a deep inelastic, peripheral, process by a central one could be the multiplicity of fragments, since the first one has a strictly binary character. Nevertheless, as it has been shown in the previous section, deleting binary events from our selections would be not a good choice in order to select central collisions: at low-intermediate energy, indeed, a binary event with a high measured value of TKEL could equally come from a process reminiscent of deep-inelastic mechanisms, as well as from a binary scission (a quasi-fission) of a composite system by quasi-fusion process, characteristic of a central collision. This is just what it was observed in the system ^{58}Ni + ^{48}Ca at 25 AMeV.

At this point it is important to underlying that in the following it will be used the variable Total Kinetic Energy TKE, measured as the sum of kinetic energy of all detected fragments (reaction products with Z≥3) in each event, in place of TKEL, for consistency with the literature's tradition: the TKE distributions is shown in fig. 3.3.

In order to distinguish a possible sensitivity of such observable to the centrality of the collision, in fig. 3.4 the same v_{par} – A correlation used in the previous section (fig. 3.2) is plotted for the three energy regions obtained by means of the two cuts at TKE = 700 MeV and TKE = 1200 MeV (fig. 3.3).

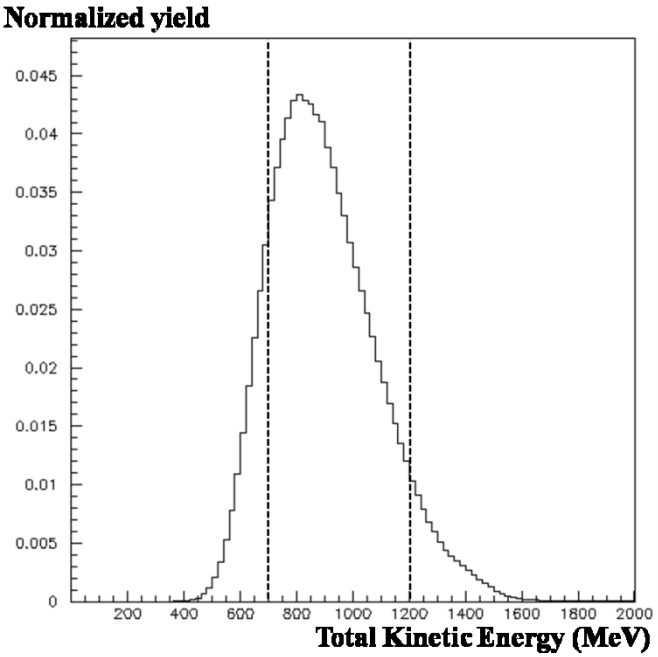

Figure 3.3 The Total Kinetic Energy (TKE) distribution measured over all the complete events.

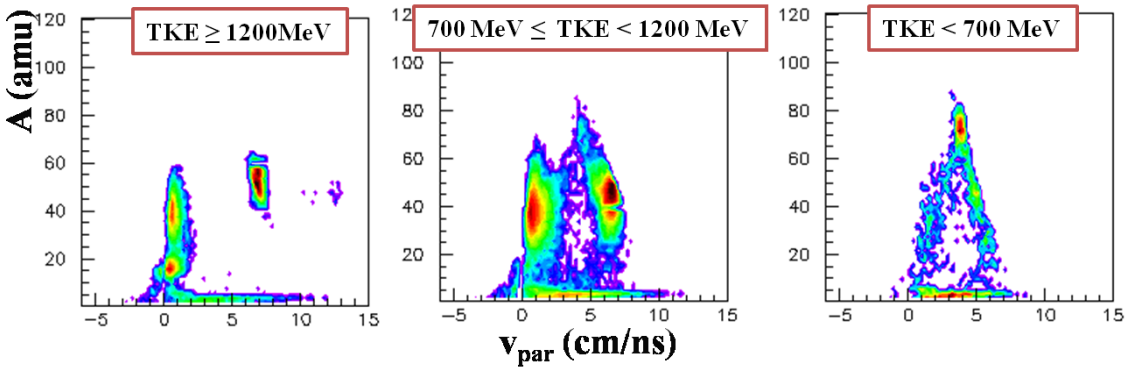

Figure 3.4 Correlation plots between the mass number A and the component of velocity parallel to the beam for all the fragments detected in the three regions of Total Kinetic Energy (TKE).

Differently from what previously observed about the charged particles' multiplicity, in fig. 3.4 we can notice a significant evolution of the fragments emission mechanism passing from one region to another: the strong contribution due to fragments similar to projectile (Projectile Like Fragments, PLFs) and to target (Target Like Fragments, TLFs), that is the dominant emission pattern in the first region, is progressively reduced with increasing of the energy dissipation.

Nevertheless, the presence of peripheral and semi-peripheral events is not completely removed by the application of these cuts on the kinetic energy, not even in the third region (TKE < 1200 MeV, fig. 3.4c)

This trend is in agreement with what is expected but, of course, the method is not powerful enough for a rigorous selection (even if qualitative) of the impact parameter, at least for most central collisions: this is indeed a clear example of how a given variable could be better suited as a centrality indicator for a given impact parameter range (peripheral in this case) but not for another one.

The relevant information we can get from the application of these cuts on TKE is that while central and semiperipheral collisions are mixed for higher value of energy dissipation, the presence of central events for values of TKEL less than about 450 MeV (corresponding to TKE ≥ 1200) is negligible. Such a statement will result in an important indication for the continuation of the analysis.

Therefore, since the strong competition between different reaction mechanisms doesn't allow the use of the two methods explained above, we have to follow another

way to “select” centrality, or at least to select data samples cleaned from peripheral and semiperipheral collisions, to which our analysis is not interested.

We have thus performed an analysis based on measuring the event shape in the momenta space by means of the kinetic energy tensor: the so called Shape Analysis, event by event, discussed and illustrated in the following sections.

3.3 The Event Shape Analysis

By reviewing the various techniques that can be used in order to select centrality, based on the measure of very sensitive observables, it is clear that a good variable is one that can preserve the main part of the information collected during the experiment. Such a condition certainly depends on the experimental apparatus as well as on the system involved and on the available energy but, as general rule, those variables measuring the shape of the event can be good candidates for selection methods.

We have also seen that different centrality ranges (thus different impact parameter ranges) prefer different variables in order to be selected, and the reason of this lies in the fact that any used method refers to quantities which are expected to vary with impact parameter and to also be representative of a specific feature of the searched collisions.

In the previous section, for instance, it was highlighted how a high value of TKE is characteristic of peripheral collisions, while it’s not strictly true the opposite, i.e. that an its low value is a feature of central ones.

In this respect, the variables related to the event shape are more appropriate to select the most central collisions, since they are able to underline an important feature of these latter: the existence of a unique emission source, revealable as a compact configuration of the matter at the decay stage [LEC96]. A shape observable is indeed a quantity related to spatial distribution of the reaction products in an appropriate reference frame.

Anyway, it should bearing in mind that any indirect method to select the centrality of the collisions, mostly the event shape ones, are always affected by errors and

fluctuations due to a model dependence, and to the finite number of detected particles [ref.]. Nevertheless, in this work the goal is not the quantitative estimation of the impact parameter, but the isolation of the most central collisions from the whole events, hence the precision degree reached (tipically 10-20% for intermediate energy reactions [DUR01]) will be enough for our analysis.

The basic idea of a shape analysis is to measure all the particles' momenta, so as to transform the interesting physical quantities into the center-of-momentum frame and thus determine the direction of maximum momentum and energy flow by performing a principal axis transformation, in analogy to the momentum of inertia tensor [STO82].

All event shape variables are obtained from a tensor with components [CUG83]:

$$F_{ij} = \sum_{\nu=1}^{N} \gamma p_i^{\nu} p_j^{\nu}$$

Eq. 3.1

where $p_{i,j}$ are the momentum Cartesian coordinates of each particle in the centre of mass and γ is a weighting factor characterizing the tensor.

Depending on such a weighting factor, the tensor can be: a *sphericity tensor* if $\gamma = 1$; a *momentum tensor* if $\gamma = {}^{1}/_{m_\nu}$; a *velocity tensor* if $\gamma = {}^{1}/_{m_\nu p_\nu}$ (m being the particle mass); or a *kinetic energy tensor* if $\gamma = {}^{1}/_{2m_\nu}$, assuming in the latter case the same expression as in eq. 1.5.

The kinetic tensor [CUG82, GYU82, BUC83d] is a generalization to intermediate energy of the sfericity one [CUG82, GYU82,STÖ82], well known and widely used at high energy. The sphericity is a concept that has been first introduced for the analysis of jet-like events in e^+ - e^- collisions [GRAS76, CRI82]: since the weighting factor is equal to one, each reaction product has the same weight in the summation, implying the disadvantage that mass A fragments receive an A times higher weight than A separate nucleons. This is not important at high energy, where selected sources undergo a complete vaporization, while become very relevant at intermediate energy where the mass distribution covers a large range of values, as shown in fig. 3.5 for the ^{58}Ni + ^{48}Ca system at 25 AMeV.

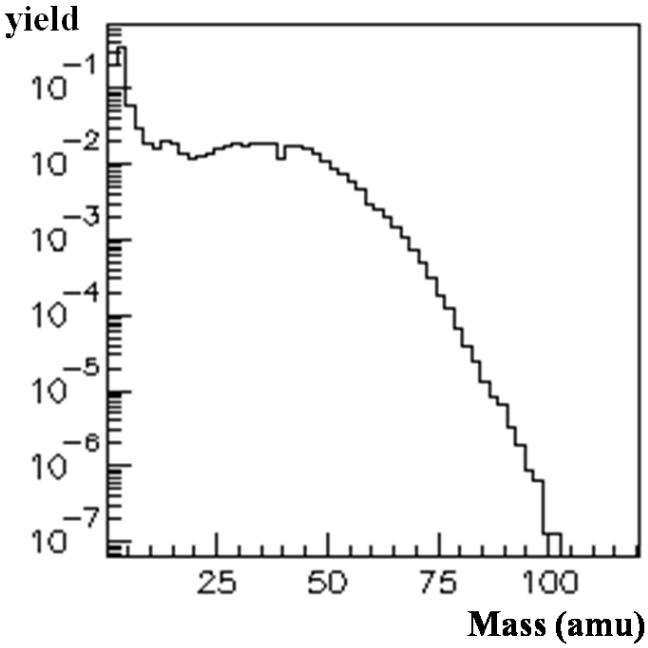

Figure 3.5 Mass distribution for all fragments in the complete events.

The weighting factor $\left({}^{1}/_{2m_v}\right)^{-1}$ in the kinetic tensor ensures that composite fragments contribute to the matter flow with the correct weight relative to nucleon, thus making such a tensor more appropriated for heavy ions reactions at intermediate energy.

The summation in eq. 3.1 could be in a first approximation extended to all detected particles in each event, but actually some researchers choose different samples of reaction products, depending on the studied reaction and on the different aspects of processes of the reaction they are interested in [LEC96].

At Fermi energy indeed, since the thermalization time and the interaction time (typically 30 fm/c for a medium mass system at 50 AMeV) are comparable, it is expected that a large fraction of the available energy may be thermalized during the reaction process itself leading to very hot systems, while another not negligible part may be not thermalized during the collision, leading to a fast emission before thermalization. Such an emission constitutes the so called pre-equilibrium emission, that could distort the source pattern, therefore the event shape, just because such pre-equilibrium particles are emitted early, before a complete memory loss of the beam direction.

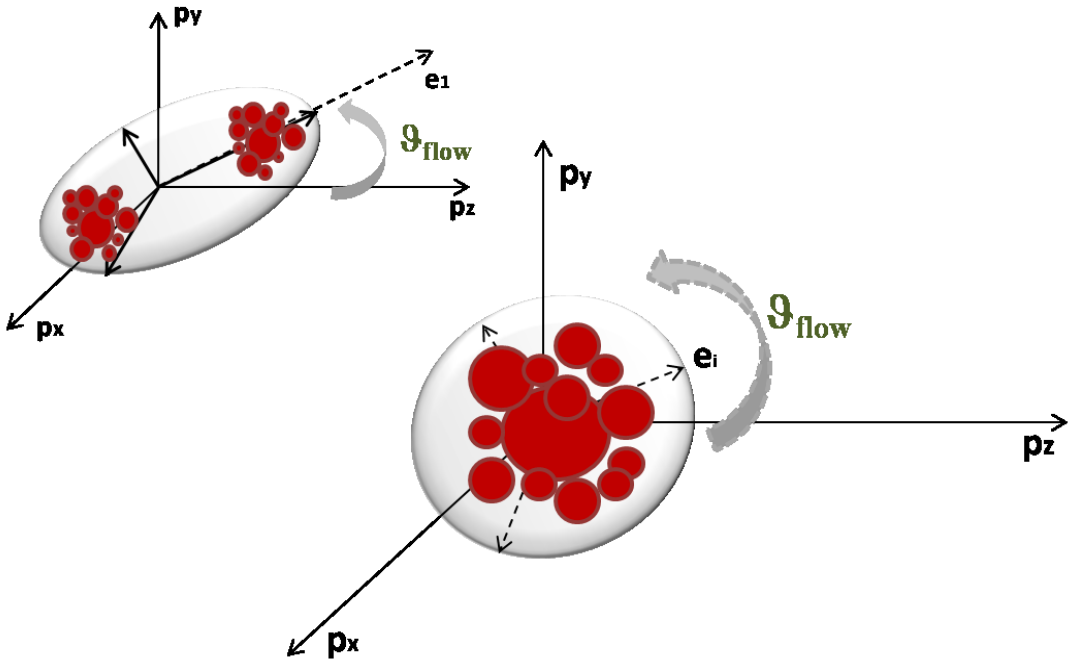

Figure 3.6 Schematic pictures of the two limiting configurations (peripheral on the left and central on the right) of the ellipsoid associated with the kinetic energy tensor.

For this reason, in the present analysis the choice was to perform the summation in eq. 3.1 by considering only fragments, excluding LCPs (whose energy information is in any case not available for this system). Therefore we can rewrite eq. 3.1 as follow:

$$F_{ij} = \sum_{Z \geq 3} \frac{p_i p_j}{2m}$$

Eq. 3.2

with the same meaning of symbols in eq. 3.1.

Such energy tensor is a 3×3 symmetric matrix that, in its diagonal form, defines an ellipsoid in momenta space with the three principal axis oriented along the three eigenvectors of F_{ij}: e_1, e_2, e_3, as shown in fig. 3.6 [GYU82, STO82, CUG83, STO86, HER99].

The corresponding eigenvalues, λ_1, λ_2, λ_3, are generally normalized to unity:

$$\lambda_1 + \lambda_2 + \lambda_3 = 1$$

Eq. 3.3

And sorted and then ordered according to the inequalities:

$$\lambda_1 \geq \lambda_2 \geq \lambda_3 \geq 0$$

Eq. 3.4

The orientation of the main axis of such ellipsoid (corresponding to λ_1) with respect to the beam axis then defines the flow angle, ϑ_{flow}, that range from 0° to 90°:

$$\cos(\vartheta_{flow}) = \boldsymbol{e_1} \cdot \boldsymbol{z}$$

Eq. 3.5

Shape variables are built starting from $\lambda_1, \lambda_2, \lambda_3$ [CUG82].

Traditionally some quantities have been proposed, among them we can find the two used for the present system:

- the Sphericity:

$$S = \frac{3}{2}(1 - \lambda_1)$$

Eq. 3.6

- and the Coplanarity:

$$C = \frac{\sqrt{3}}{2}(\lambda_2 - \lambda_3)$$

Eq. 3.7

together with others historically used like:

- the ratios:

$$q_1 = \frac{\lambda_1}{\lambda_3} \quad and \quad q_2 = \frac{\lambda_2}{\lambda_3}$$

Eq. 3.8

where $q_1 \geq q_2$,

- the "Jettiness":

$$j = \lambda_1 - \lambda_2$$

Eq. 3.9

- the "Prolateness":

$$\phi = \frac{\lambda_2 - \lambda_3}{\lambda_1 - \lambda_3}$$

Eq. 3.10

and

- the "Eccentricity":

$$\varepsilon = \lambda_s - \frac{1}{2}(\lambda_2 - \lambda_r)$$

Eq. 3.11

where λ_s is the eigenvalue corresponding to the axis of quasi-symmetry that is equal to λ_1 or λ_3 for prolate (in this case it follows $\lambda_r = \lambda_3$) or oblate ($\lambda_r = \lambda_1$) shape of the event respectively [CUG83].

Cugnon et al. presented in their work (see ref. [CUG93]) a review of the more used shape variables and ordered them in a table, like the following Table 3.1, where the values they assume were indicated for the three limiting event shapes: sphere, rod, and disk.

Shape Variable	Sphere	Rod	Disk
q_1	1	∞	∞
q_2	1	undefined	∞
Sphericity	1	0	$3/4$
Coplanarity	0	0	$\sqrt{3}/4$
Jettiness	0	1	0
Prolateness	Undefined	0	1
Eccentricity	0	1	$-1/2$

Table 3.1 Values of the global variables for limiting events. From [CUG83]

The overall size of the tensor is of little interest, since it is mainly given by conservation laws, while, in order to get a topological description of the sources, one shape variable and one angle (usually the above cited flow angle ϑ_{flow}) are sufficient.

Moreover, since the volume of the ellipsoid cannot change event by event, an event with a large linear momentum distribution along an axis will result in a very prolate ellipsoid, while an event with an almost isotropic distribution in momentum space will correspond to a more spherical shape. In the first case we can imagine that

the fragments are mainly "located" in the two lobes of the ellipsoid, as distant as the momentum range along that axis is large. Otherwise, in the second condition, the centre of the ellipsoid (corresponding to the centre of mass momentum of the reaction) will be mainly populated, as illustrated in fig. 3.6. Unlike the case of prolate ellipsoid, this latter case is indicative for a strong redistribution of momenta during the reaction.

In such two different circumstances the two lobes of the ellipsoid and the centre of the more spherical figure represent the emission sources of detected fragments: in this respect a shape variable like the sphericity can give indication about the existence of one single source (namely sphericity value close to 1) or different sources (sphericity value close to zero) in each event. Therefore a shape analysis can provide first information about the centrality of the collisions, but it's important to keep in mind that such a variable is affected by the strong fluctuations due to the finite number of fragments used to evaluate it. For this reason it is very important to adapt the use of shape variables to the specific reaction studied: in the present work they can provide just an indication of the topology of the source, since, as already stressed, the multiplicity of fragments in each event is very low also for the more central collisions (we found 25% of events with just a fragment in the final state in events with ϑ_{flow} greater than 60°) and this tends, for instance, to lower the value of the sphericity.

Another relevant information comes from the knowledge of the orientation of the main axis of the ellipsoid with respect to the beam axis, that is given by the value of the flow angle ϑ_{flow}: in a peripheral or semiperipheral collision indeed the events keeps memory of the entrance channel of the reaction (of the beam direction in particular), so that the inclination of the main axis will be very small, providing small values of the flow angle. Regarding the previous mentioned problem about the difficulty of removing events from deep inelastic processes, this could be accomplished by the following satisfactory solution. Deep inelastic reactions exhibit indeed a completely non isotropic angular distribution of the emitted fragments, being the latter mostly emitted at low angles with respect to the beam direction, with peaks in the angular distributions located at angles close to the grazing angle. With

respect to the momenta space, this situation leads to low values of the flow angle, that we can thus consider to reject from our analysis.

The situation completely changes for central collisions. The latter, indeed, leading to a more spherical shape of the ellipsoid, may not properly have a main axis, or, once identified (event by event and on a large statistical sample of events), such an axis will be isotropically distributed in the space so that the flow angle could assume any value between 0° and 90°. This is what we expect for transient systems that have forgotten any memory of the entrance channel, in particular of the beam direction.

3.3.1 Event shape analysis on ^{58}Ni + ^{48}Ca at 25 AMeV reaction

An event shape analysis is presented in this section for the studied reaction, ^{58}Ni + ^{48}Ca at 25 AMeV. A first step consists in correlating the flow angle ϑ_{flow} defined in eq. 3.2 with the Total Kinetic Energy TKE carried away by fragments. The relative plot, commonly called Wilczynski-like plot, is shown in fig. 3.7.

Such a method was proposed for the first time at intermediate energies for the analysis of the reaction Pb + Au at 29 AMeV, performed by using the Nautilus multidetector [LEC96].

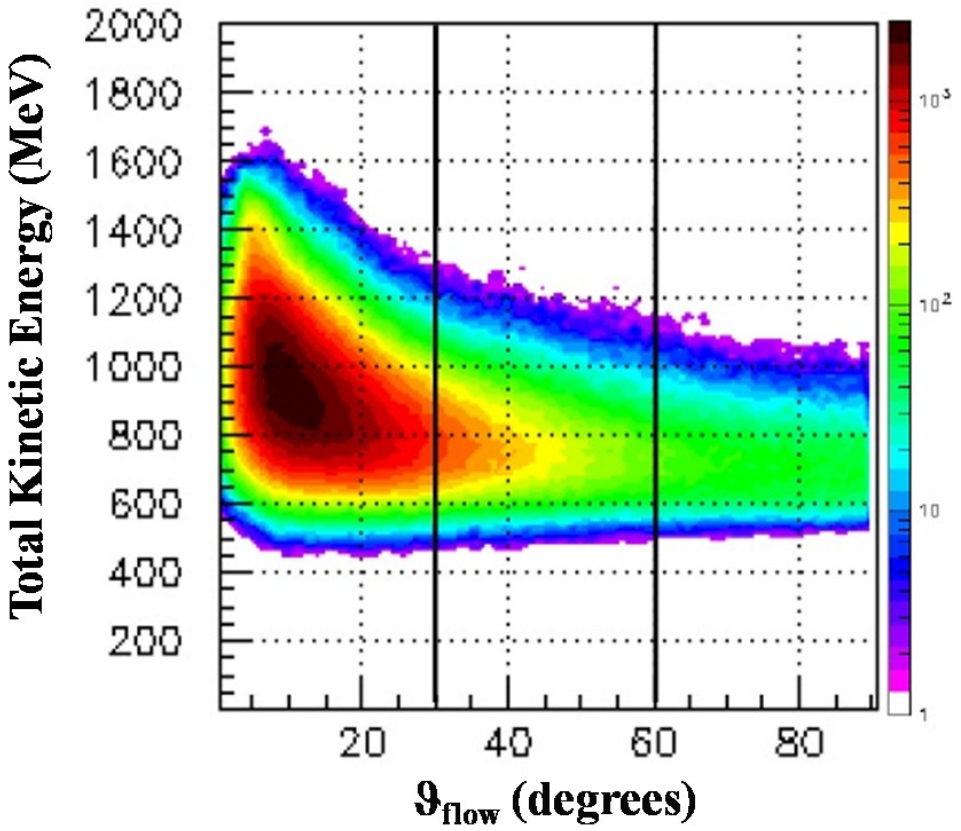

Figure 3.7 Correlation plot between the Total kinetic energy (TKE) and the flow angle ϑ_{flow}, for all detected fragments in complete events.

Even if there is a clear correlation between the two observables TKE and ϑ_{flow}, being both built with the same fragments, this is not relevant for the implementation of the method. The total kinetic energy carried away by the fragments, indeed, just determines the volume of the ellipsoid, that has no effects on the shape analysis and is not related to the inclination of the ellipsoid.

As it is possible to notice, an increase in the ϑ_{flow} value will results in a selection of more dissipative collisions that, as seen (fig. 3.4), are those where the contribution from central collisions is the dominant one. In particular, in fig. 3.7 we can observe that flow angle values ranging between 60° and 90° correspond to Total Kinetic Energy values less than 1200 MeV, thus to a part of the events shown in the third panel of fig. 3.4. Events with such high values of ϑ_{flow}, by definition of flow angle, come from the collisions with the most weak memory of the kinematic properties of the entrance channel of the reaction, in particular of the beam direction.

The collected indications suggest performing the event selection according to ϑ_{flow} values, choosing flow angles values greater than 60° for the most central collisions.

It is therefore worthwhile to divide the TKE- ϑ_{flow} plot by means of two cuts at $\vartheta_{flow} = 30°$ and $\vartheta_{flow} = 60°$ and follow the emission pattern varying the angle in order to check such a selection.

We chose to give first a qualitative idea of the source shape by using the first two defined variables sphericity and coplanarity.

3.3.2 Sphericity – Coplanarity correlation

Usually, in order to perform a topological analysis of emitting sources, the more common shape variables are the sphericity and the coplanarity. Their distribution are not shown separately but correlated as in fig. 3.8.

Both these quantities range from 0 and 1 and their correlation defines a triangle in the sphericity-coplanarity plane. Inside the triangle each region identifies a different shape: a disk close to the upper vertex, a rod in the zone close to the origin of the axes, and finally a sphere in the right lower part (see fig.3.8).

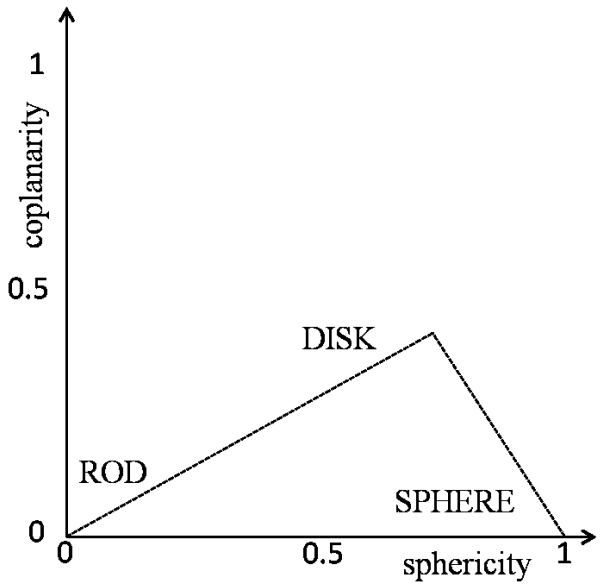

Figure 3.8 A schematic picture of the Dalitz plot.

In fig. 3.9 a, b, c such plots are shown, built with all fragments emitted in each event for the three different regions of flow angles, each point representing an event inside the triangle.

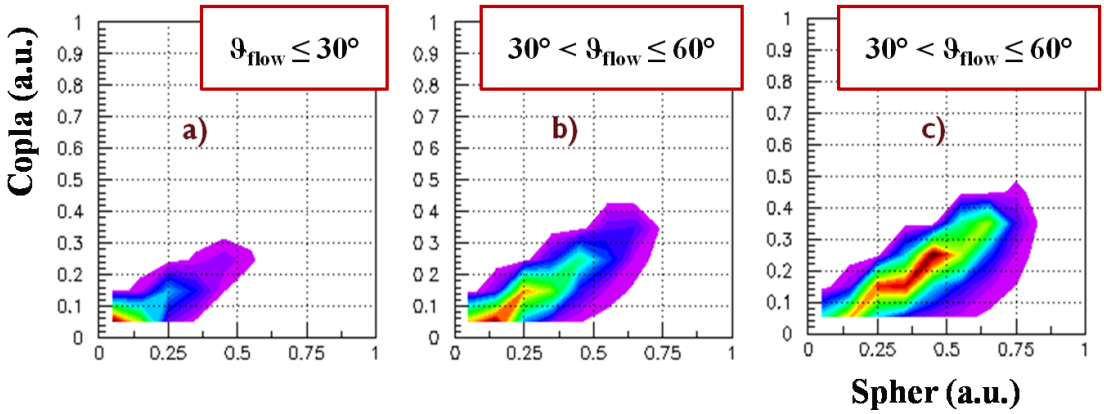

Figure 3.9 Sphericity and coplanarity correlation plot for the three selected regions of flow angle: by moving toward the regions at higher angles the centre of the triangle is more and more populated, indicating an evolution of the event shape to a more spherical configuration.

An evolution of the event shape is observed from the rod-like structure for low values of the flow angle to more spherical shapes for higher flow angle values, showing a relevant sensitivity of the flow angle variable to the "compactness" of the matter configuration in the momentum space.

It is possible to notice that the sphericity cannot reach very high values because of the low number of fragments used event by event in its evaluation: also in the third region, indeed, for high values of the flow angle (corresponding to high degree of energy dissipation), events with only one or two fragments are still largely present (see fig.3.10) and thus widely contribute to the event shape.

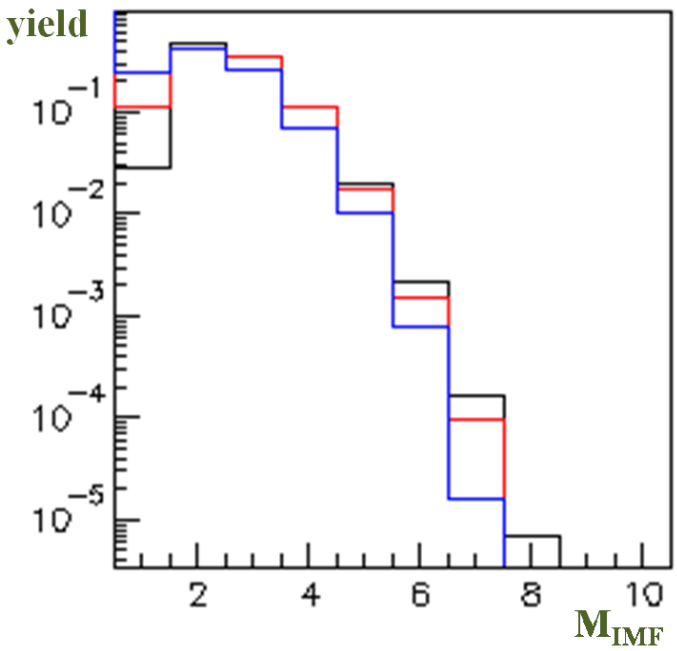

Figure 3.10 Comparison between the M_{IMF} distributions for events with $\vartheta_{flow} \leq 30°$ (black line), $30° < \vartheta_{flow} \leq 60°$ (red line) and $60° < \vartheta_{flow} \leq 90°$ (blue line).

In fig. 3.10 the distributions of fragments' multiplicity are shown for the three above selected ϑ_{flow} windows by means of the black, the red and the blue lines respectively. The yield of events with just one or two fragments is very high until the third region, where it even becomes dominant. Such an aspect of these events will be very interesting for the study of the competition between different reaction mechanisms, carried out in the next chapter.

3.3.3 Velocity – mass correlation

In order to check if the cuts in the TKE- ϑ_{flow} correlation can constitute a good centrality selection, in fig. 3.11 the v_{par} – A correlation with increasing of flow angle values is shown, similarly to what previously done for different TKE cuts. It is evident a steady decrease of the contribution to the emission due to Projectile Like Fragments (PLFs) or Target Like Fragments (TLFs), that is signature of a gradual vanishing of peripheral collisions with increasing of the flow angle.

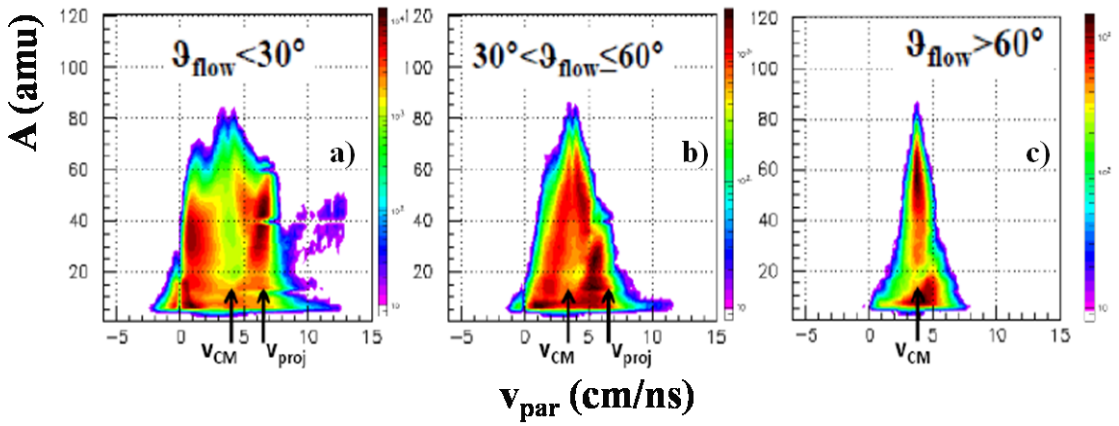

Figure 3.11: Correlation plots between mass and parallel velocity for fragments emitted in events with $\vartheta_{flow} \leq 30°$ (panel a), $30° < \vartheta_{flow} \leq 60°$(panel b) and a), $\vartheta_{flow} > 60°$ (panel c).

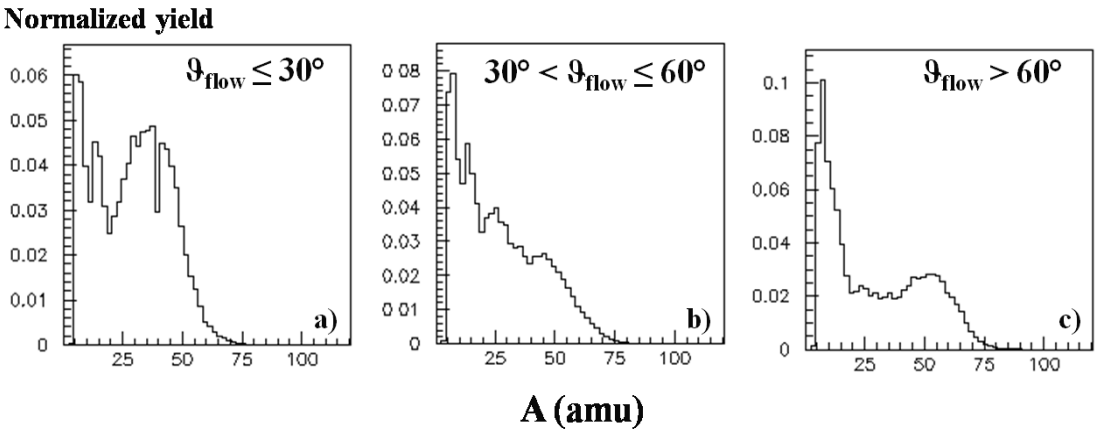

Figure 3.12: Mass distribution of fragments detected in events the three different regions of flow angle.

Similarly, the spectrum in longitudinal velocity shows a gradual increase of yield densities around the mid-velocity region between the PLF and TLF velocities, up to the third panel (fig. 3.11c: flow angle greater than 60°) where it is more and more centred upon the centre of mass velocity (v_{CM}). In terms of the kinetic energy tensor and corresponding ellipsoid, such an evolution results in gradually closer values of the three λ_i eigenvalues, and can be seen as a relative approaching of the two lobes of the ellipsoid.

Moreover, looking at fig. 3.12 a,b,c (projections of fig. 3.11 a,b,c respectively on the *y* axis) it is possible to observe a characteristic trend of the mass distribution as function of the flow angle: the emission component due to fragments with mass values greater than those of projectile or target (also exceeding 60 amu), that was already present for low value of ϑ_{flow}, becomes the most relevant in the third

region. These events are strongly indicative of the formation of a heavy residue coming from fusion-evaporation processes (therefore of central collisions), while the component covering the intermediate range of mass could be a first indication for the possible presence of multifragmentation processes (these also characteristic of central events).

The contributions from peripheral and semi-peripheral collisions are therefore progressively removed and the cut on high values of ϑ_{flow} , greater than 60 degrees, results in a very useful tool in order to select very compact sources from the most central collisions.

3.4 Emitting sources characterization

By means of the shape analysis it was thus possible to select those sources characterized by a high compactness in the momenta space, therefore indicative for the formation of a unique source and for a strong redistribution of linear momentum transferred to the fused system, and by a high degree of energy dissipation. The characterization of the corresponding events in terms of mass and velocity distributions then acted as a check for the applied selection.

Once selected these most central collisions, we are interested in a first characterization of the emitting sources, so that in the next chapter we will go to investigate the different reaction mechanisms that are competitive in such collisions.

3.4.1 vpar – vper correlation and invariant Galilean cross section

A very worthwhile tool in order to identify and to "visualize" the fragments' sources for a selected class of events is to plot the invariant Galilean cross section in a tridimensional velocity representation:

$$\sigma_{inv} \propto \frac{1}{Av_{\perp}}\left(\frac{d^2\sigma}{dv_{\parallel}dv_{\perp}}\right)$$

Eq. 3.12

where the abscissa and the ordinate are, respectively, the parallel to the beam and the perpendicular to the beam velocity components ($v_{\parallel}$ and $v_{\perp}$respectively) and the third axis then is the corresponding cross section, normalized according to the elementary differential volume $2\pi v_{\perp}dv_{\parallel}dv_{\perp}$. In this way the plot is shown as isocontours of cross section.

In fig. 3.13 such a correlation plot is presented, symmetrised and with a logarithmic intensity scale for the third axis, for the three regions of flow angle (a: $\vartheta_{flow} \leq 30°$; b: $30° < \vartheta_{flow} \leq 60°$; c: $\vartheta_{flow} > 60°$).

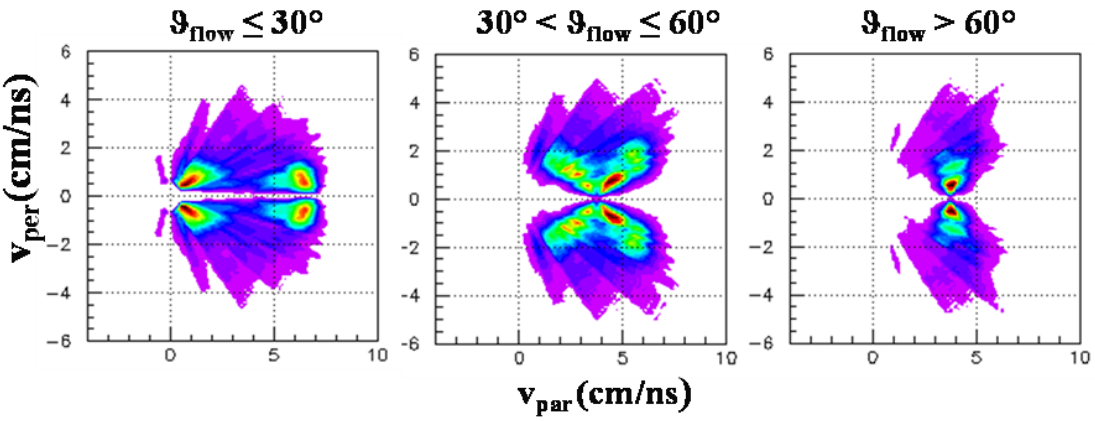

Figura 3.13 Invariant vpar-vper cross section plots relative to the fragments from events with $\vartheta_{flow} \leq 30°$ (panel a), $30° < \vartheta_{flow} \leq 60°$ (panel b) and $\vartheta_{flow} > 60$ (panel c).

The location of the fragments for the three different classes of events in such a plot is consistent with the emission from two distinct sources (PLF for fragments with parallel velocity close to $v_{proj} = 6.5\ cm/ns$ or TLF for those with velocity close to zero) in the first region while, passing through an intermediate situation in panel b, a well-defined unique source with velocity values close to the centre of mass

velocity ($v_{CM} = 3.8\, cm/ns$) is finally evident in the third region. This is in total agreement with what was underlined in previous sections.

3.4.2 Some features of the emitting sources

The shape analysis up to now performed has therefore driven toward a good selection of "compact sources" (i.e. a unique source, event by event) coming from very central collisions. In this last section we would like to characterize such sources in terms of mass and excitation energy, providing some information from simple evaluations and theoretical computations.

The selected sources show a mean mass value $\langle A_{bound} \rangle \cong 90$ amu, simply evaluated as the summation of the atomic masses of all detected charged particles, corrected for the undetected evaporated neutrons.

In this summation both fragments used to build shape variables from the kinetic tensor and light charged particles (whose energy information is not available but that we can detect and identify) are included.

Computations carried out by M. Colonna from Laboratori Nazionali del Sud in Catania in collaboration with E. Geraci from INFN-Sez. di Catania in the framework of the Boltzmann-Nordheim-Vlasov (BNV) transport theory predicted a source charge of about 34-37, a source mass around 75-80 amu and an excitation energy of 2.5-3 AMeV (after about 400 fm/c) for an impact parameter b = 0 ÷ 1 fm [GER09].

In fig. 3.14 the time evolution of the ^{58}Ni + ^{48}Ca at 25 AMeV reaction (red dots), together with the ^{58}Ni + ^{40}Ca one (blue dots) at the same energy is presented in terms of excitation energy (first panel), average mass and charge of the sources (second and third panel respectively).

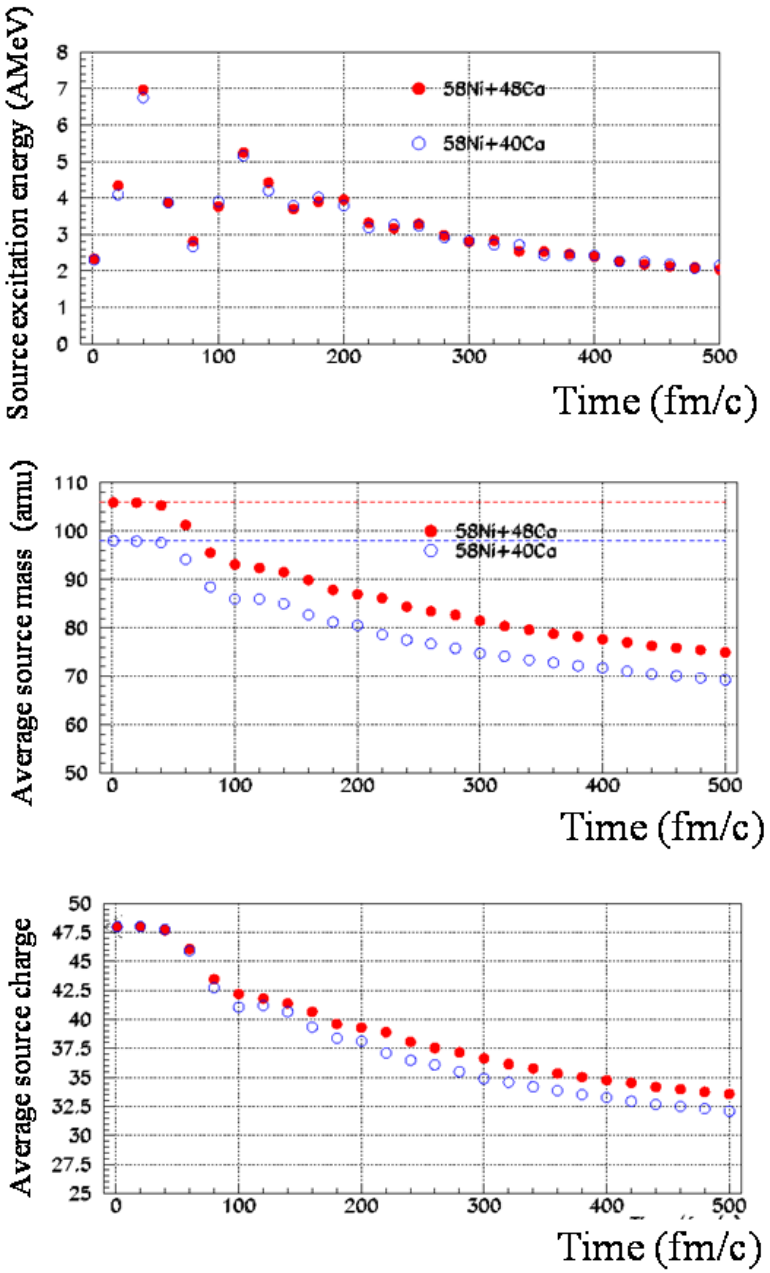

Figure 3.14 Time evolution of the ^{58}Ni + ^{48}Ca (red dots) and ^{58}Ni + ^{40}Ca (blue dots) reactions at 25 AMeV from BVN calculations: the average source excitation energy, mass and charge evolutions are shown in the upper, middle and lower panel respectively.

Afterward, in order to compare the experimental data with ideal pure central collisions, the same computations have been carried out lowering the value of the impact parameter, in the limiting situation b = 0. The lower b value results in slightly different values of the charge, mass and excitation energy of the sources: equal to 43, 94 and 400 $\pm$ 50 MeV respectively.

CHAPTER 4

Reaction mechanisms competition

In the previous section it has been shown how to isolate the most central events on the basis of an event shape analysis aimed to investigate the nuclear matter configuration in the momenta space. The identification of the so called “compact sources”, i.e. the presence of a unique emission source, event by event, for the detected fragments, provided relevant information about the centrality of the collisions, and allowed to perform a proper selection of the class of events of interest in the present thesis.

In this section we propose to investigate the reaction mechanisms that are competitive in such central collisions and to isolate the multifragmentation sources, if present, in order to extract their most relevant characteristics. In particular, the possible onset of that process that leads to a low density coexistence phase of nuclear matter that falls in the well known multifragmentation phenomenon will be evidenced

The already stressed competition among different reaction mechanisms in such most central collisions is evident by looking at fig. 3.11c, in this section represented as fig. 4.1, where the fragments properties are shown in terms of their parallel velocity and mass. In this plot fragments coming from different events are mixed, so that we can distinguee the various contribution to emission, but not separate events from different processes (like a fusion-like followed by evaporation or a multifragmentation mechanism).

One of the main reasons for selecting events with flow angle greater than 60° (see fig. 4.1), besides the large energy dissipation and the “compactness” of the sources, was the observed evolution of the parallel velocity spectrum, with increasing of flow angle value, toward values very close to the centre of mass velocity ($v_{CM} \cong 3.8$ cm/ns). Such behaviour indeed, together with the high values of mass reached by the emitted fragments (around 60-65 for the most massive), gives strong evidence for a

fusion-like process of projectile and target, typical of very central collisions. Moreover, this class of events, that covers just the 6.2% of the complete events, also shows a broad mass distribution with a relevant amount of fragments in the range between 20 and 40 amu. Such an emission contribution opens the doors to an interesting and stimulating exploration of the reaction mechanisms that could be responsible of such a phenomenon, first of all the presence, also like an onset, of the already cited multifragmentation process.

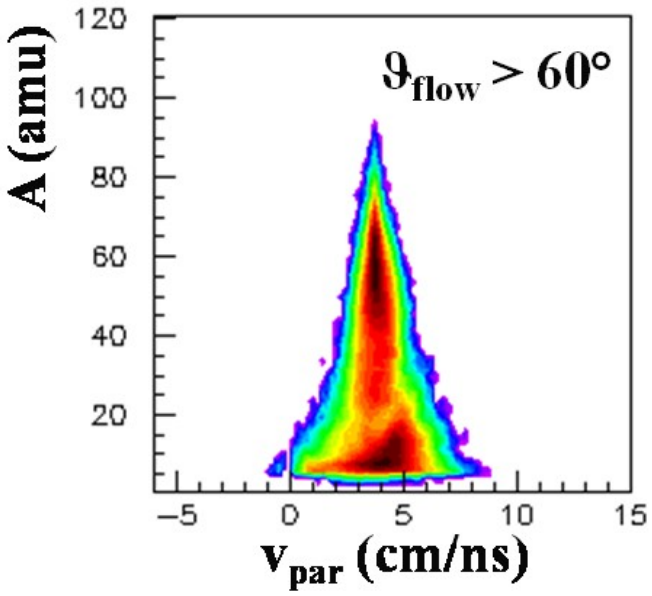

Figure 4.1 Mass and parallel velocity correlation for all fragments emitted in the selected central events (flow angle greater than 60 degrees).

4.1 An event by event analysis

As already noticed, the fragments emitted by different events are mixed in the correlation plot of fig 4.1, so that it is not possible to associate a fragment to a specific emission process starting from this first information. For this reason, in order to obtain more detailed information, in fig. 4.2 the same velocity-mass correlation plot of fig. 4.1 is reported, but in this case only for the heaviest fragment emitted in each event, whose correspondence is indicated with the number “1”. Thus the plot shows the mass of the heaviest fragment A(1) in the y axis vs. its parallel component of velocity vpar(1) on the x axis.

In this way it is possible to disentangle between events that show or not show the presence of a heavy remnant, that is commonly associated with a fusion evaporation mechanism, and then to separately studying such two different classes of events.

We first impose an arbitrary cut at mass value equal to 40 amu, as drawn in fig. 4.2, so dividing the central events in two groups that in the following will be indicated as "classes" to simplify the terminology. Such a choice, even if arbitrary in a first approximation, comes from reasonable consideration about the previously evaluated mass of the emitting sources (section 3.4.1). If we consider indeed a mass of about 90 amu for the composite system formed because of the fusion-like of projectile and target (after pre-equilibrium emission), we expect to detect fragments of about 40 amu for a symmetric splitting (a fission-like), or fragments with a greater mass value in the case of evaporative deexcitation. Since we are searching for possible multifragmentation events, it is not hazardous to imagine that these latter lie in the remaining class of events: those characterized by mass values less than 40 amu for the heaviest emitted fragment, shown in the lower panel of fig. 4.2.

In order to better characterize our choice, the mean values of IMFs and light charged particles multiplicities, $<M_{IMF}>$ and $<M_{LCP}>$ respectively, are reported in figure 4.2 for both the two classes of fragments.

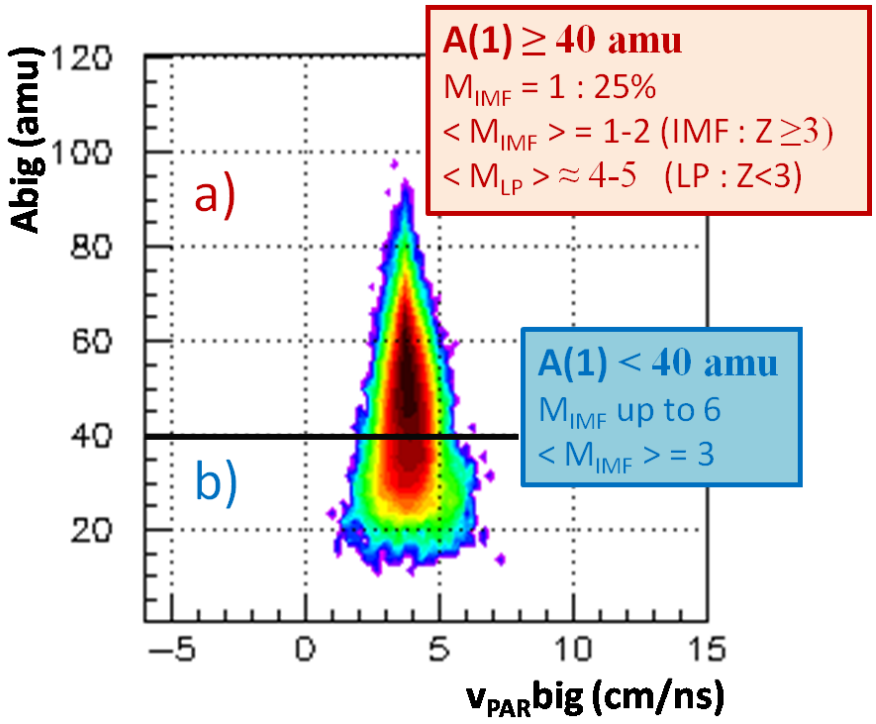

Figure 4.2 Mass (amu) and parallel velocity (cm/ns) correlation for the heaviest fragment in each central events.

If we look at the differences in terms of yields of events with one, two or more fragments in the final state between the two classes of events identified by the cut in A(1) (fig. 4.3), we realize that the events with only one fragment, that constitute 25% of the first class (black line), are essentially absent in the second (red line): here the M_{IMF} spans a substantially wider range of values, around an average of $\langle M_{IMF} \rangle = 3$ and reaching a maximum at $M_{IMF} = 6$. Moreover, in the second class the emissions of three or four fragments become dominant, while what provides the main contribution to the first class of events is a binary process, in which two fragments are emitted in coincidence with 4-5 light charged particles (Z=1, Z=2).

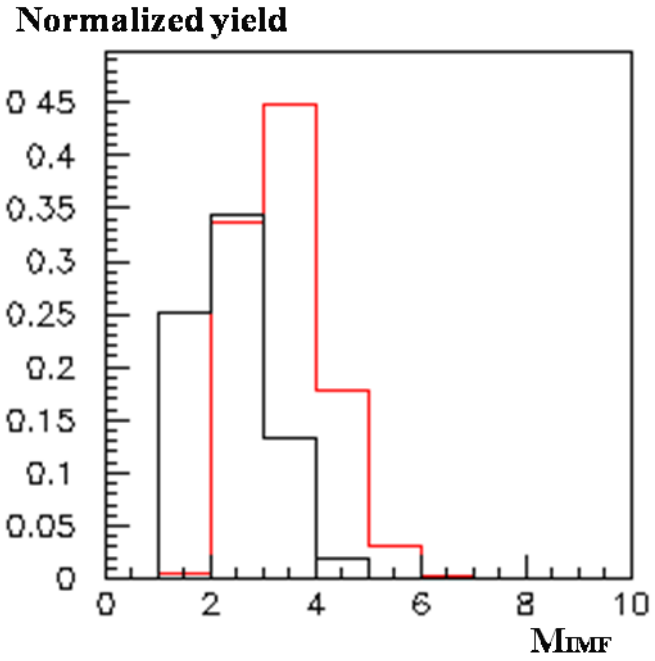

Figure 4.3 Multiplicity of Intermediate Mass Fragments distributions for event in the "first class" (with A(1) ≥ 40: black line) and in the "second class" (with A(1) < 40: red line).

As already discussed concerning the evaluation of the impact parameter, however, the M_{IMF} observable alone is not able to give complete information about the emission processes, mostly in events with two or three fragments in the final state. This is true, for the studied system, not only in looking for the centrality of the collisions, but more generally in the investigation of the main reactions' features.

Being in an energetic region of strong competition among different reaction mechanisms indeed, for a given value of M_{IMF} it remains a strong ambiguity between different possible processes. Let consider for instance a two or three body emission (again from central collisions): the first process could equally come from an evaporation of light particles from the quasi-fused system plus one small fragment, or from a fission-like mechanism. Similarly the three body emission could be consequent to a fission-like process again accompanied by another small fragment (evaporative process) or to a multifragmentation event where three masses are formed at the same time with almost equal masses (an onset of multifragmentation events with more and more fragments at high energies).

In order to disentangle among such several competitive reaction mechanisms we therefore need further information, first of all concerning the masses of the emitted fragments.

4.2 Mass distributions: from binary to more fragmented events.

4.2.1 Low Multiplicity: one remnant and binary events

Events that show just a heavy remnant in the final state, accompanied by some light charged particles and strongly indicative for the formation of a quasi-fused nuclear system that de-excites via evaporation of light particles, constitute a not negligible percentage (25%) of the central events.

Concerning events with two fragments in the final state, it can be interesting to look at the mass distributions of the first and the second heaviest fragment emitted in each event: A(1) and A(2) respectively. This is indeed a basic tool in order to visualize such emissions and better understand if they come from a fusion-evaporation or a fission-like event, both reminiscent of the lower energy reaction mechanisms in central collisions.

In fig. 4.4 the A(1) and A(2) mass distributions are shown for the totality of central events. Moreover, since we found a large percentage of such binary events in the first class ($A(1) \geq 40$) but also a not negligible amount in the second ($A(1) < 40$), in fig. 4.5 the A(1), A(2) mass distributions for both the two classes are also plotted.

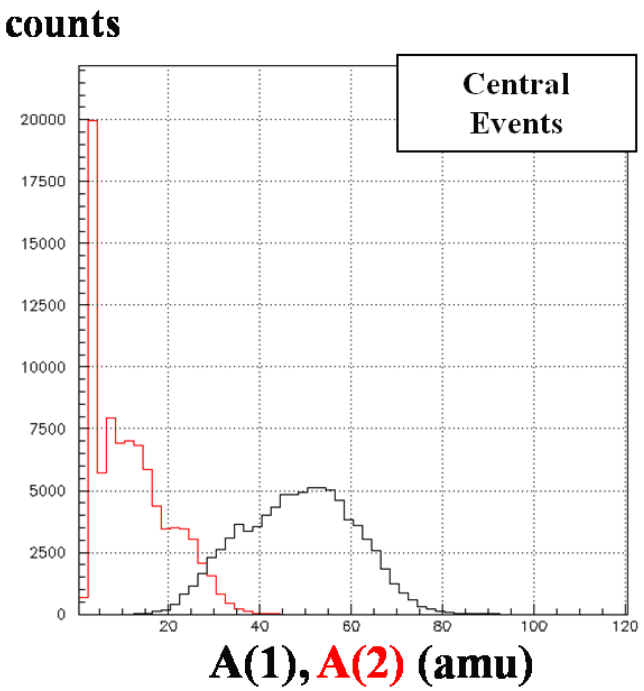

Figure 4.4 Mass distributions of the two heaviest fragments A(1) and A(2) (ordered according with their masses) for all the central events.

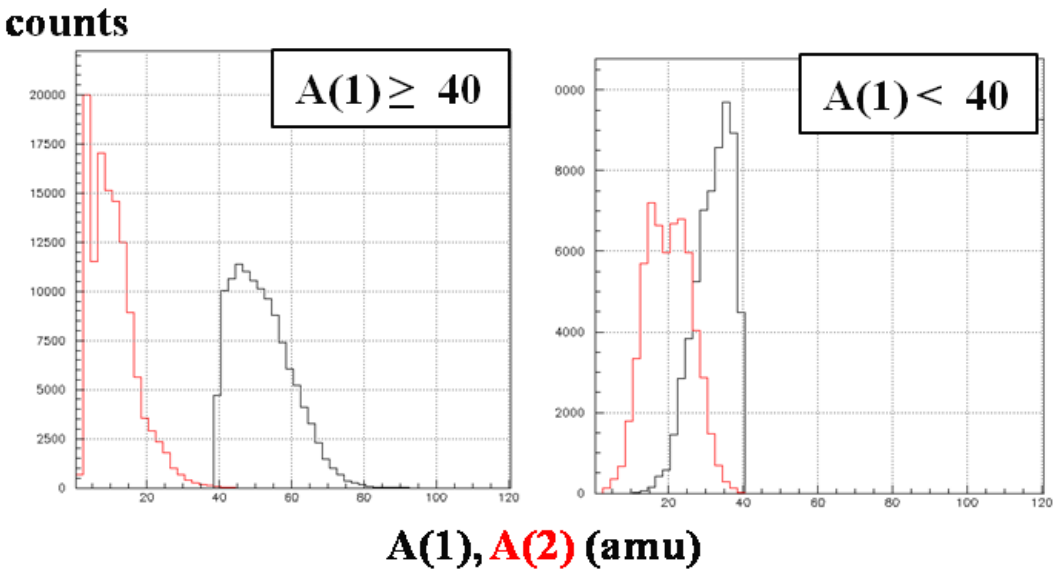

Figure 4.5 Mass distributions for the two heaviest fragments in the events with A(1) ≥ 40 amu (belonging to "first class") and with A(1) < 40 amu ("second class") : left and right panel respectively.

It is readily visible that the binary events (almost those with A(1) ≥ 40 amu, here identified as belonging to the "first class") show a great mass asymmetry, very far

from a symmetric fission-like scenario. Such a character of the emission is strongly attributable to a fusion-like evaporative mechanism, that is the process with the largest cross section at low energy. In a statistical framework the decay of a nucleus is related to the number of states that are allowed to the decaying system, proportional to the density of accessible states. Such a scenario, where the excitation energy and the temperature are connected by the relation $E^* = aT^2$, is valid for temperature values $T \leq 3 \div 4$ MeV (Fermi gas model).

It is worth notice also the presence, even if very small, of emissions characterized by a very little asymmetry, whose main contribution lies in the second class of events ($A(1) < 40$ amu), as it is trivially expected because of the mass conservation.

The similarity between the A(1) and A(2) masses in such a class of events is indicative for the presence of symmetric fission-like processes, at least for a small percentage recognizable in the plot as the overlap region between the two curves.

Therefore, based on what just observed, we can assert that the studied reaction is dominated by fusion-evaporation processes, with a not negligible contribution of fission-like mechanisms, at least for what concerns events with a small (less than three) number of fragments.

But furthermore, since such events (with one or two fragments in the final state) constitute the 68% of total central collisions, we can generalize such a statement and assert that the main part of the emissions in such a reaction is strongly reminiscent of the reaction mechanisms characteristics of the low energies, and in particular of evaporative processes.

What so far found highlights the strong competition present in our system and characteristic of the intermediate energy regime, at least in terms of possible memory of low energy processes. Now, what we want to investigate is a possible onset of the multifragmentation mechanisms that, differently, is characteristic of higher energies. In order to do this we must therefore concentrate our attention on those events with higher value of M_{IMF}.

4.2.2 Dalitz plots: mass splitting of the selected sources.

Let's go now to ternary of with more fragments events. It is indeed such en ensemble that we should investigate for the possible presence of multifragmentation events. Information on mass distributions for these latter can come from the analysis of the Dalitz plots both for the first and the second class of the events mentioned above.

A Dalitz plot is a triangular plot that allows highlighting the relationship between the mass (or charge) distributions of the three heaviest fragments emitted in each event. Once measured, the three masses are used to build the following coordinates in a Cartesian frame:

$$x = \frac{1}{3}(A_2 - A_3)$$

Eq. 4. 2

$$y = A_1 - \frac{1}{3}S_{123}$$

Eq. 4. 3

where $S_{123} = A_1 + A_2 + A_3$. In this way, each point of coordinates (x, y) lies in an equilateral triangle, the distances d_i to each side of the triangle being equal to A_i.

Each point thus represents an event and the position of each point (each event) inside the triangle is able to give information about the mass asymmetry between the three heaviest fragments.

In particular: in the corners there are events with a heavy residue and two small fragments (long distance from an axis means high value of mass of a fragment), the sides are occupied by events characterized by a binary behaviour (more or less symmetric emission of two massive fragment plus a small one: fission-like) while the centre of this triangle is characterized by multifragmentation events (the three distances from the axis are almost the same), see fig. 4.6.

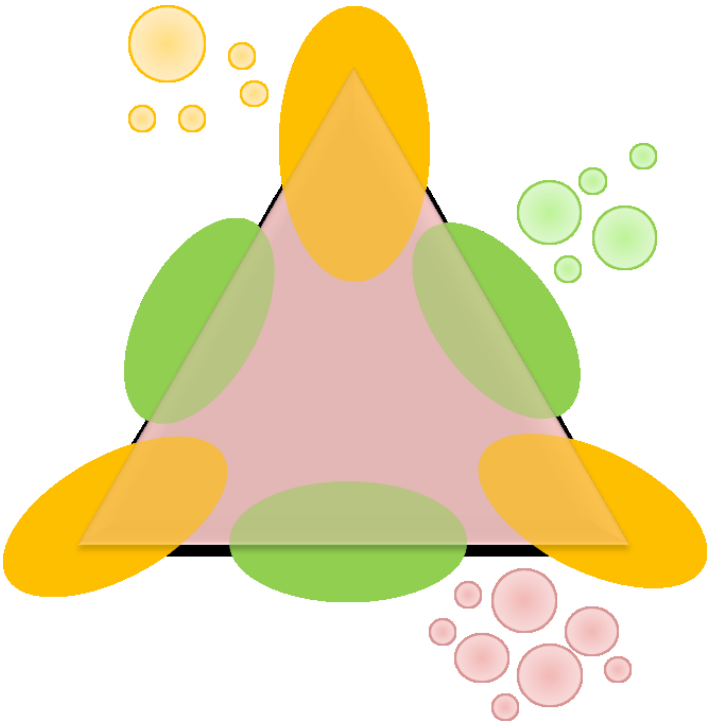

Figure 4.6 Schematic picture of a Dalitz plot: events in the corners are characterized by an heavy remnant and light particles (yellow), events on the sides are indicative for binary splitting (green) and finally the inner part is filled by multifragmentation events (light red).

In fig. 4.7a,b the Dalitz plots are built for the two selected classes of central events, with A(1) ≥ 40 amu and A(1) < 40 amu respectively, and just for fragment multiplicity $M_{IMF} \geq 3$. It could worth consider that the first and the second class cover the 75% and the 25% of the central events respectively.

Already from a first glance it readily appears a completely different behaviour of these highly fragmented emissions, which means completely different reaction mechanisms that have produced them.

Looking at fig. 4.7a) we can indeed observe that the main part of events is located on the vertices of plot, indicating the complete dominance of events with a heavy residue and at least two light fragments, characteristic of typical fusion-evaporation phenomena. Otherwise, events in fig. 4.7b) show the approaching of a more symmetric splitting of the source, filling the inner area of the triangle and depleting vertex and sides, as it is expected for multifragmentation events.

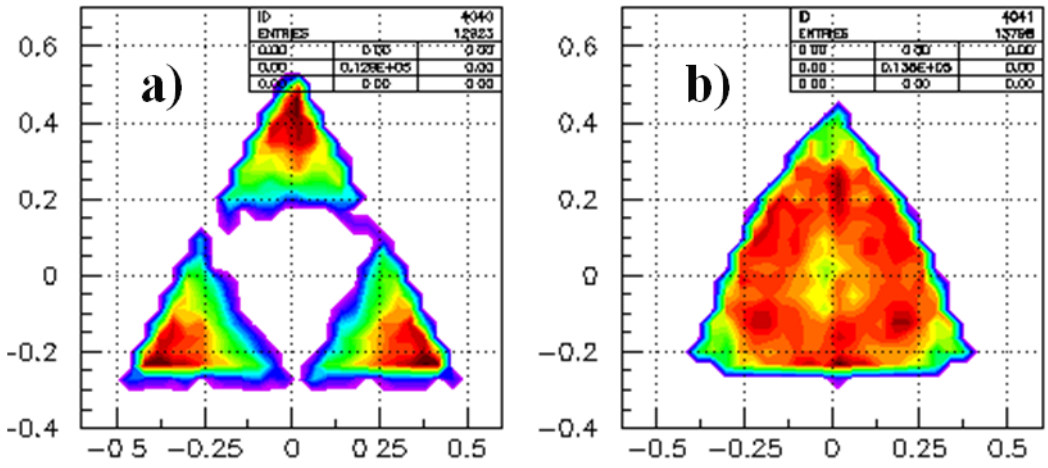

Figure 4.7 Dalitz plots for events belonging to the "first class" (a) and to the "second class" (b).

In this way, by using the cut on the mass of the heaviest fragment, we could highlight the competition between fusion-evaporation and multifragmentation mechanisms for events with higher number of fragments (≥ 3) from very central collisions. If we had tried to select multifragmentation events from M_{IMF} cuts, equal or greater than three for instance, we would have confused such two kinds of emissions, while higher cuts would have excluded a large amount of multifragmentation events, leading to an incomplete analysis, made on a very low statistic.

4.3 Comparison with evaporative models: is it finally plausible to talk about Multifragmentation?

According to our analysis and in particular to the latter discussion about fragmented events that have been visualized in terms of mass asymmetry by means of the Dalitz plots, we got to select a class of events that seems to be the best candidate for the multifragmentation scenario.

These events are characterized by $M_{IMF} \geq 3, \langle M_{LCP} \rangle \cong 5$ and $A(1) < 40\ amu$.

In such a way, considering the remaining part of events as belonging to a fusion-like mechanism followed by an evaporative deexcitation, we finally assert that such a multifragmentation onset covers in the studied reaction about the 16.4% of reaction mechanisms in central collisions.

In order to have a more clear idea about this strong competition between reaction mechanisms, namely quasi-fusion-evaporation or fission-like and multifragmentation, we have compared mass distributions and multiplicities for selected central events (without any differentiation between fusion-evaporation and multifragmentation like events) with those predicted by a two step mechanism: dynamical stochastic BNV calculation followed by the sequential de-excitation of the composite source (SIMON code).

The source information was obtained from BNV calculations, including pre-equilibrium emission, and corresponds to a source with mass equal 94 amu, a source's charge of atomic number Z =43 and an excitation energy equal to 400 MeV (± 50 MeV). In this computations we have considered events from central collisions of vanishing angular momentum (L=0) (see section 3.4.1).

The second stage, concerning the de-excitation of the sources produced by the BNV computations, is carried out by means of the SIMON code, developed by D. Durand and based on the EUGENE generator.

The SIMON code consists itself of two phases, the first concerns the preparation of the system (according to the reaction mechanisms that one chooses to simulate) while the second one regards the decay of the formed nuclei via binary sequential emission of fragments and light particles. The decay of primary nuclei is obtained by a sequence of binary break-up using Monte Carlo simulations treated in the framework of the transition state theory. This latter was developed by Moretto [MOR75] and Swiatecki [SWI83] as generalization of the Bohr and Wheeler formalism that describes the symmetric nuclear fission.

With respect to the EUGENE code the SIMON code takes into account the discrete levels of light nuclei as Li, Be and B for the study of the decay in light particles (n, p, d, α) and considers the coulombian trajectory of emitted fragments in order to ensure the conservations of space-time correlation, so allowing a detailed comparison with experimental data.

Figure 4.7 shows the comparison of fragment multiplicity distributions (left panel) and mass distributions (right panel) for experimental data (black line) and for the calculations (red line). At this stage of comparison the simulation data are not yet

filtered, i.e., energy and mass resolutions, detector efficiency and trigger threshold are not included. We can notice the quite good agreement in reproducing the shape of both multiplicity and mass distribution for both heavy and light reaction products, indicating the dominance of evaporative mechanisms in the selected central collisions.

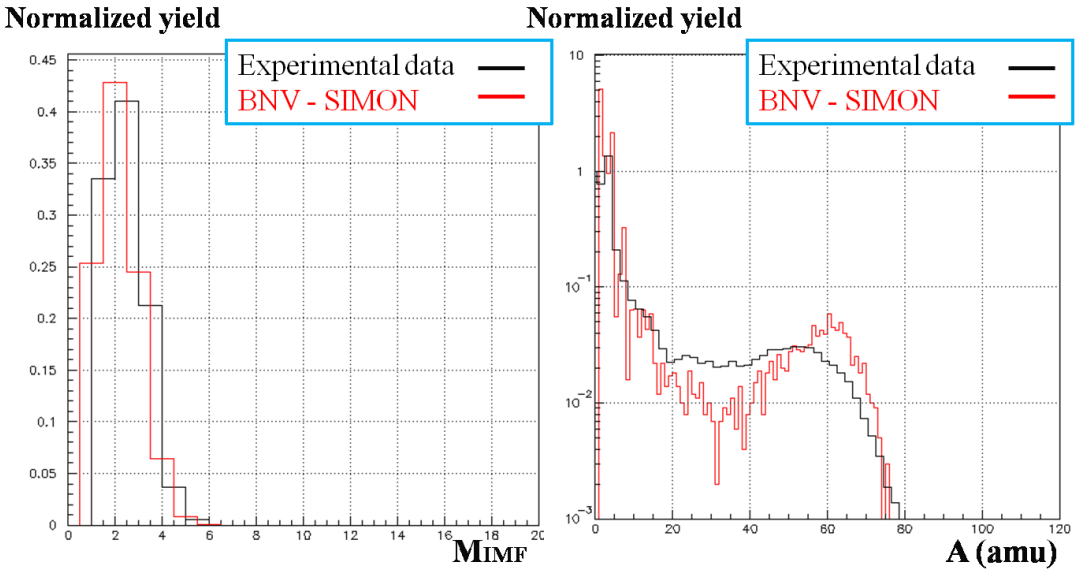

Figure 4.8 Comparison between experimental (black line) and theoretical (red line) M_{IMF} distribution. Right: mass distribution for experimental data (black line) and results of calculation (red line).

The only one part of the mass spectrum not so well reproduced by simulations, in favor of an enhancement of heavy residue contribution, is that one populated by fragments with mass between 20 and 40 amu, so at this point the question is: "can we expect to find different, not sequential, not evaporative-like, decay mechanisms for this, although small, part of events?". On the other hand, it has been previously noticed how events related to such quite massive fragments are those constituting the second class of events in sect. 4.2.2, with A(1) < 40 amu and $M_{IMF} \geq 3$, mainly characterized by a very symmetric splitting of the sources on three or more fragments and strongly indicative for multifragmentation processes (see fig. 4.7b).

The mass distribution of fragments emitted in such events is shown in fig. 4.9: it is readily possible to notice that it covers properly the part of fig. 4.8 not reproduced by the SIMON (sequential and evaporative) code.

It had seen in the previous section that these events cover a small percentage, about 2%, of all the complete data for the present system.

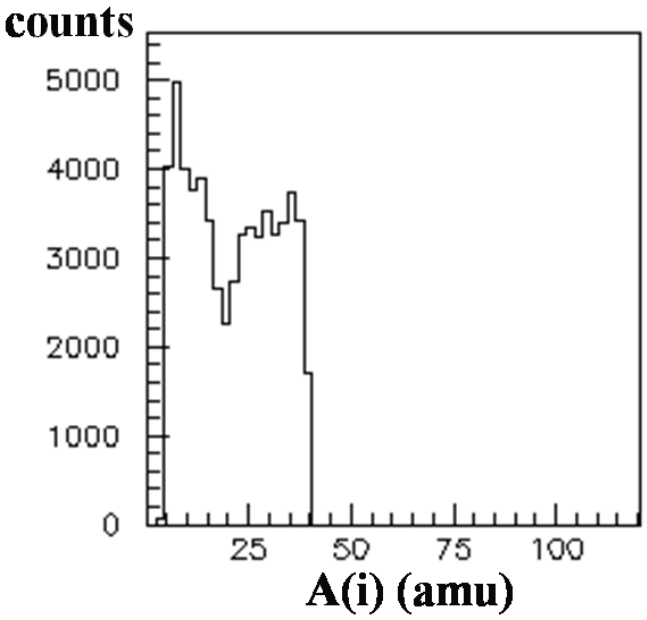

Figure 4.9 Mass distribution from fragments belonging to central events with A(1)<40 and $M_{IMF}\geq 3$.

Finally, the good agreement between the experimental data and a data generator like the SIMON code confirms the results of the previous sections about the great dominance of reaction mechanisms reminiscent of fusion-evaporative processes.

About the 83.6% of the central events can indeed be associated to such scenario, mainly in terms of evaporation by a composite source with consequent detection of a heavy remnant of the quasi-fusion reaction and in terms of quasi-fission, well recognizable in event with two (section 4.2.1) or more fragments (see Dalitz plots in fig. 4.7b). The Fermi energy regime is indeed a sort of bridge between low and high energy, ruled by the competition of mean filed and nucleon-nucleon interactions and characterized by the emission of fragments called IMFs. The open question about such fragmentation mechanism, that connects evaporation and vaporization [GRO90, MOR93, BON95, RIV01] as an evolution with energy of one to another, is whether it can be seen as an offshoot of fission and evaporation (sequential phenomena) from low energies or as an onset of the complete (prompt) nuclear disassembly of the high energies regime, including a liquid-gas phase transition.

In order to better understand in which faceting our analysis is moving it is relevant now to investigate the properties of the multifragmenting sources: their mass, temperature, excitation energy. The first is related to size effects on the reaction mechanism, the second and the third features are decisive in the opening of a new decay channel as multifragmentation and in order to evaluate the possibility of a phase transition of finite nuclear matter from liquid to liquid + gas phase, exploring the coexistence region in the stage of fragments' formation.

4.4 Multifragmentation sources: Temperatures and excitation energy evaluations.

Among the most central events (with $\vartheta_{flow} > 60°$) we have thus isolated sources of multifragmentation, selected as sources of events that show a multiplicity of fragments $M_{IMF} \geq 3$ and a mass value of the heaviest emitted fragment $A(1) < 40$ amu.

The total mass of such emitting sources is readily estimated around 90 amu by the summation of the masses of charged light particles and fragments, corrected for the undetected neutron multiplicity.

The excitation energy of the system can be evaluated, with the subtraction calorimetric method, summing the total kinetic energy available in the centre of mass frame and the Q value (energy difference between the initial and final masses) taking into account the mass conservation: in this way we obtained a value of the so called calorimetric excitation energy $E^*_{cal} \cong 5$ AMeV.

Moreover, we have also estimated the excitation energy in a second way, using the BNV model to describe the time evolution of the interacting nuclei up to the assumed equilibration of the emitting systems (about 400 fm/c): $E^*_{BNV} = 4.2 \pm 0.5$ AMeV.

Now, for such sources, we would like to extract another information, very meaningful in the perspective of a multifragmentation scenario: the nuclear temperature. Actually, the temperature that we can evaluate is just an "apparent" temperature, as cited in sect. 1.5.5 where the three methods for its estimation have been shown.

We have performed a measurements of the so called “chemical” temperature, or temperature of the isotopic ratios, using the yields of isotopes of Li, Be and C [ALB85]: in particular ^{6,7,8}Li, ^{7,9,10}Be and ^{11,12,13}C.

As already mentioned in chapter 1, the method of double ratios of isotope yields is based on some assumptions like the thermal and chemical equilibrium of the emitting source, detected as a unique source for all used isotopes, and the validity of the Maxwell-Boltzmann statistics for the system.

The method uses a statistical approach, where the probability of fragment emission is ruled by the phase space constraints, in particular by the separation energy associated to the emission process [DUR01] that is directly related to the chemical potential μ. For density values of the source much lower than the saturation density, it is not simple to evaluate such chemical potential, related to the free protons and free neutrons ones, μ_Z and μ_N respectively, via $\mu = \mu_Z + \mu_N$; the isotopic ratio method forbears this measurements considering the yields of fragments differing by a single neutron or a single proton, prior to secondary decay: in this way the chemical potentials finally cancel out (in a first approximation).

Therefore once chosen two pairs of isotopes (or isotones) it is possible to build the double ratio:

$$R = \frac{Y(A_i, Z_i)}{Y(A_{i+1}, Z_i)} \frac{Y(A_{j+1}, Z_j)}{Y(A_j, Z_j)} = R_1 R_2$$

Eq. 4.4

R_1 and R_2 are function of the spins and the binding energies of the fragments: the spin factors are then combined into a single variable α_s while the four binding energies are enclosed into the factor ΔB, so that the eq. 4.3 becomes:

$$R = \alpha_s exp(^{\Delta B}/_{T})$$

Eq. 4.5

Consequently, it is possible to measure the isotopic temperature:

$$T = {}^{\Delta B}/_{ln(R/\alpha_s)}$$

Eq. 4.6

However, it should be kept in mind that the fragments can be highly excited, leading to secondary decays that can result in non-negligible corrections to the measured ratios R. To reduce the sensitivity to such corrections, it is advisable to choose cases for which $\Delta B \gg T$ [MIL98].

From literature [MIL98] it is well known that the best thermometers are those with a high value of the ΔB parameter in eq. 4.5, therefore we have used only those with $\Delta B > 10$ MeV.

In the last years a long list of couples of ΔB and α_s values has been compiled: in table 4.1 those of our interest are reported.

Nuclear species pairs	ΔB (MeV)	α_s^{-1}
He - Li	13.3	2.2
Be -Li	11.3	1.8
Li - C	11.5	5.9
C - C	13.8	7.9

Table 4.2 Values of the coefficients use in 4.5 for different couples of nuclear species.

The values shown in table 1 are thus used in eq. 4.5 in order to measure four values of temperature T using different ratios of yields: $^{6}Li/^{7}Li - {}^{11}C/^{12}C$, $^{7}Li/^{8}Li - {}^{11}C/^{12}C$, $^{9}Be/^{8}Li - {}^{7}Be/^{6}Li$ and $^{12}C/^{13}C - {}^{10}C/^{11}C$.

The used relationships and the resulting temperatures are indicated below:

$$T_{Li-C} = 11.5/ln\left(5.9 * \frac{Y(^{6}Li)/Y(^{7}Li)}{Y(^{11}C)/Y(^{12}C)}\right) = 2.77 \pm 0.14\ MeV$$

Eq. 4.7

$$T_{Li-C} = 11.5/ln\left(5.9 * \frac{Y(^{7}Li)/Y(^{8}Li)}{Y(^{11}C)/Y(^{12}C)}\right) = 2.58 \pm 0.14\ MeV$$

Eq. 4.8

$$T_{Be-Li} = 11.3/ln\left(1.8 * \frac{Y(^{9}Be)/Y(^{8}Li)}{Y(^{7}Be)/Y(^{6}Li)}\right) = 3.99 \pm 0.11\ MeV$$

Eq. 4.9

$$T_{C-C} = 13.8/ln\left(7.9 * \frac{Y(^{12}Li)/Y(^{13}Li)}{Y(^{11}C)/Y(^{12}C)}\right) = 3.93 \pm 0.09MeV$$

Eq. 4.10

We can notice that the errors' values decrease if we use heavier thermometers and this is due to higher statistics available for such isotopes.

Finally we can associate an average apparent temperature $\bar{T} = 3.9 \pm 0.1\ MeV$ to selected sources.

Such a value, together with the ones for excitation energy extracted from both calorimetric method, $E^*_{cal} \cong 5$ AMeV, and BNV calculation $E^*_{BNV} = 4.25 \pm 0.50$ AMeV, defines a point in the temperature-excitation energy relationship, in agreement with the existing systematic for the caloric curve, where temperature values between 3 and 4 MeV are associated to this excitation energy range in the "plateau" region (fig. 4.9), in a phase transition scenario.

Such an apparent temperature's value is lower than the one (about 6 MeV) predicted by the simple relation $E^*=aT^2$ for a Fermi system in a liquid phase.

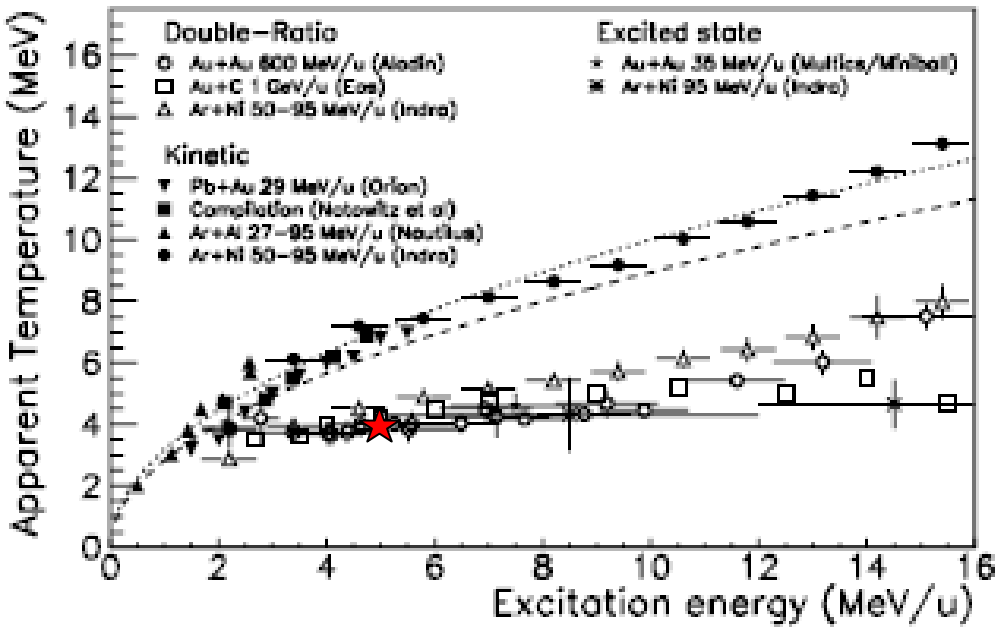

Figure 4.10 Systematic of measured nuclear temperatures with the three methods described in section 1.5.5 as a function of the excitation energy [DUR01].

Summary and conclusions

In this PhD thesis it is presented the study concerning the competition of different reaction mechanisms in central collisions at Fermi energies, with particular interest on the onset of multifragmentation phenomena as a possible evolution of evaporative processes toward more explosive mechanisms.

This study has been carried out through the analysis of the $^{58}Ni + ^{48}Ca$ reaction at 25 AMeV, performed at the Laboratori Nazionali del Sud in Catania by the ISOSPIN and NUCL-EX collaborations in 2003. The ion beam was accelerated by the Superconducting Cyclotron and the reaction products were collected and identified in mass, charge and energy by the CHIMERA multidetector.

The experiment belonged to an experimental campaign lasted four years, that aimed to the investigation of the termodinamical characteristics of sources formed in central collisions at intermediate incident energy in the framework of a systematic study of the liquid and liquid-gas coexistence region with new generation devices.

In order to reach such a purpose, an important part of this work has been devoted to an efficient selection and characterization of central events among all detected events by using the event shape method, based on the construction of the kinetic energy tensor for the analysis of the configuration of the matter in the momentum space at the decay stage.

It has been noticed how a cut on the shape variable ϑ_{flow} (at $\vartheta_{flow} = 60°$) obtained by the diagonalization of the tensor resulted in a strong reduction of peripheral and semiperipheral less dissipative events, and in a very stringent selection of single compact sources, on an event by event basis.

This latter feature has been highlighted by the analysis of other event shape variables like the sphericity and the coplanarity and their correlations and also trough the distributions in longitudinal vs. transverse velocity of all fragments coming from such sources.

Once selected such most central events, the main features of the reaction products were explored by using different constraints on some of the relevant observables, like mass and velocity distributions and their correlations.

In this way, a dominance of evaporative (sequential) mechanisms together with evidences of more fragmented processes has been highlighted and the two different contributions to emission have been firstly disentangled by a cut on the mass value of the heaviest fragment detected in each event (at A(1) = 40 amu).

A successive analysis of the fragments' mass distributions for different values of fragment multiplicity, performed by means of the Dalitz plot for ternary and more highly fragmented events, has leaded to the selection of a not negligible (even if small) percentage of events that can be reasonably considered as the best candidates for evidence of prompt multifragmentation.

In order to better understand the nature of the mechanisms involved in such central collisions, the experimental data have been compared with the results obtained by a two steps calculation. Dynamical stochastic BNV computations, taking into account the dynamical evolution of the system and pre-equilibrium emissions in the framework of transport theories, provided information about the emitting sources. Afterwards, the de-excitation of such sources was carried out by means of the SIMON code, that followed decay of the formed nuclei via binary sequential emissions of fragments and light particles.

Preliminary results have shown reasonable agreement with the assumption of sequential multifragmentation emission in the mass region of IMFs close to the heavy residues, while deviations from sequential processes have been found for those IMFs in the region of masses intermediate between the mass of heavy residues and the mass of light IMFs. Such a region, corresponding to events with a IMFs multiplicity greater than two and mass of the heaviest emitted fragment lower than 40 amu, has been finally the object of a termodinamical analysis.

Excitation energy estimation (both from calorimetric method and theoretical computations) and apparent temperature evaluations through the isotopic ratio thermometer applied on light emitted nuclei (Li, Be and C), have been performed in order to analyze the possibility of a phase transition of finite nuclear matter from liquid to liquid + gas phase in the studied system, exploring the coexistence region in the stage of fragments' formation: results are in quite in agreement with the existent systematic of excitation the energy and temperature correlation.

It could be very interesting to enlarge such analysis by studying the evolution of the reaction mechanisms with increasing of the incident energies and by investigating its isospin dependence. This will be possible by exploring those variables sensitive to the symmetry energy in the comparison with other systems as $^{58,62}Ni+^{40,48}Ca$ in the reactions at 25 AMeV and 35 AMeV carried out by the collaboration.

Bibliography

[ADE11] G. Ademare, Phys. Rev. C83, 0546199 (2011).

[AIE95] S. Aiello et al., Nucl. Phys. A 583, 461c (1995).

[AIE97] S. Aiello et al., Nucl. Instr. and Meth. A 385, 306 (1997).

[AIE98] S. Aiello et al., IEEE Trans. on Nucl. Sci. 45, 1798 (1998).

[AIE98b] S. Aiello et al., IEEE Trans. on Nucl. Sci. 45, 1877 (1998).

[AIE98c] S. Aiello et al, Nucl. Instr. and Meth. B 136, 1172 (1998).

[AIE99] S.Aiello et al., Nucl. Instr. and Meth. A 427, 510 (1999).

[AIE00] S. Aiello et al., IEEE Trans. Nucl. Sci. 47, 114 (2000).

[AIE00b] S. Aiello et al., IEEE Trans. Nucl. Sci., 47, 196 (2000).

[ALB85] S. Albergo et al., Nuovo Cimento A89 (1985).

[ALD02] M. Alderighi et al., IEEE Trans. Nucl. Sci. 49, 334 (2002).

[ALD02b] M. Alderighi et al., IEEE Trans. Nucl. Sci. 49, 432 (2002).

[ALD04] M.Alderighi et al., Nucl. Phys. A 734, E88-E91 (2004).

[ALD04b] M. Alderighi et al., 2004 IEEE Nucl. Scie. Symp. Conference Record, 0-7803-8700-7/04/$20.00 (C) IEEE 2004

[ALD05] M. Alderighi et al., IEEE Trans. on Nucl. Scie. 52 N. 5, 1624 (2005).

[AMM63] C.A.J. Ammerlaan et al., Nucl. Instr. and Meth. 22, 189-200 1963.

[BAC95] O. Bacri et al., Phys. Lett. B 353, 27 (1995).

[BAR05] V. Baran et al., Phys. Rep. 410, 335 (2005), and references therein.

[BEA96] L. Beaulieu et al., Phys. Rev. Lett. 77, 462 (1996).

[BEA00] L. Beaulieu et al., Phys. Rev. Lett. 84, 5971 (2000).

[BOC00] F. Bocage et al., Nucl. Phys. A 676, 391 (2000).

[BON86] A. Bonasera, Phys. Rev. C 34, 740 (1986) and references therein.

[BOR90] B. Borderie et al., Ann.Phys. 15, 287 (1990).

[BOW93] D.R. Bowman et al., Phys. Rev. Lett. 70, 3534 (1993).

[BON00] A. Bonasera et al., Rivista del Nuovo Cimento 23 N.2, 1 (2000).

[BOT00] R. Botet et al, nucl-ex/0101012 and Phys. Rev. E62 1825 (2000).

[CAV90] C. Cavata et al, Phys. Rev. C 42, N. 4, 1760 (1990).

[CHA91] R.J. Charity et al., Zeit. Phys. A 341, 53 (1991).

[CHO94] P. Chomaz, "The nuclear liquid gas phase transition and phase coexistence: A review", arXiv:nucl-ex/0410024.

[CHO08] P. Chomaz, F. Gulminelli. Phase Transitions in Finite Systems using Information Theory. *Dynamics and Thermodynamics of Systems with Long Range Interactions: Theory and Experiments*, Jul 2007, Assisi, Italy. 970, pp.175-202.

[COLI03] J. Colin et al., Phys. Rev. C 67, 064603 (2003).

[COR95] E. Cornell et al., Phys. Rev. Lett. 75, 1475 (1995).

[CRI82] L. Criegee and G. Knies, Phys. Rep. C83, 151 (1982).

[CUG83] J. Cugnon and D. L'Hote Nucl. Phys. A397, 519-543 (1983).

[DAG96] M. D'Agostino et al., Phys. Lett. B 371, 175 (1996).

[DAG00] D'Agostino M. et al, Nucl. Phys. A650 329(1999); and Elliott J. B. et al, Phys. Rev. Lett. 85 1194(2000)

[DAN01] P. Danielewicz, Nucl.Phys. A 685, 368c (2001).

[DAV02] B. Davin et al., Phys. Rev. C 65, 064614 (2002).

[DEF05] E. De Filippo et al., Phys. Rev. C 71, 044602 (2005).

[DEF05b] E. De Filippo et al., Phys. Rev. C 71, 064604 (2005).

[DUR98] D. Durand, 1998 Nucl. Phys. A ,630 52c.

[ENG89] J. B. A. England and al., Nucl. Instr. and Meth. A 280, 291 (1989).

[FIS67] M.E. Fisher, Physics 3, 255 (1967).

[GER09] E. Geraci et al., Procs. of International Workshop on Multifragmentation and related topics IWM2009, Catania, Italy (2009).

[GER11] Lessons of "Heavy Ions Physics": prof. Elena Geraci, University of Catania (2011).

[GRAS76] Nucl. Phys. B102, 297 (1976).

[GRE85] C. Grégorie, Procs. Of Winter College on Fundamental Nuclear Physics, Ed. K. Dietrich, M. Di Toro and H. J. Mang, 467 (World Scientific, 1985).

[GUA97] A. Guarnera et al, Phys. Lett. B403 191 (1997), Chomaz Ph. et al, Phys. Rev. Lett. 73 3512 (1994).

[GUL97] F. Gulminelli and D. Durand, Nucl. Phys. A615 117 (1997) and ref. therein.

[GYU82] M. Gyulassy, K.A. Frankel and H. Stöcker, Phys. Lett. B110, 185 (1982).

[HAU98] J.A. Hauger et al., Phys. Rev. C 57, 764 (1998).

[HER99] Herrman et al., Annu.Rev. Nycl. Part. Sci., 49, 581 (1999).

[KEM84] J. Kemmer, Nucl. Instr. and Meth. A 226, 89 (1984).

[LAR98] Y. Larochelle, et al., Phys. Rev. C 57, R1027 (1998).

[LEC95] J.F. Lecolley et al., Phys. Lett. B 354, 202 (1995).

[LEC96] J. F. Lecolley et al., Phys, Lett. B387, 460-465 (1996).

[LEF00] T. Lefort et al., Nucl. Phys. A 662, 397 (2000).

[LUK97] J.Lukasik et al., Phys. Rev. C 55, 1906 (1997).

[LYN95] W.G. Lynch, Nucl. Phys. A 583, 471-480 (1995).

[MIL98] P.M. Milazzo et al. Phys. Rev. C 58, 953 (1998).

[MIL01] P.M. Milazzo et al., Phys. Lett. B 509, 204(2001).

[MIL02] P.M. Milazzo et al., Nucl. Phys. A 703, 466 (2002).

[MIL98] P.M. Milazzo, et al. Phys. Rev. C58 953 (1998).

[MON94] C.P. Montoya et al, Phys. Rev. Lett. 73, 3070(1994).

[MOR75] L.G. Moretto, Nucl. Phys. A247, 211 (1975).

[NAT02] Natowitz et al., PRC 65, 034618 (2002).

[NAT08] J.B. Natowitz, et al. Phys.Rev C65 034618 (2002).

[NGO78] C. Ngo and M. Lefort, Ann. De Phys. 3, 5 (1978).

[OGI91] C. Ogilvie et al., Phy. Rev. Lett. 67, 1214(1991).

[DUR01] D. Durand, Dominique Durand, P. Sabatier, "Nuclear Dynamics in the Nucleonic Regime", Ed. CRC Press (2000).

[PAG95] A. Pagano, et al., Procs. Of Perspectives in Heavy Ion Physics, 2nd Japan–Italy Joint Symposium '95, May 22–26 1995, Riken, Japan, Ed. World Scientific, Singapore (1995).

[PAG01] A. Pagano et al., Nucl. Phys. A 681, 331 (2001).

[PAG04] A. Pagano et al., Procs. of XLII International Winter Meeting on Nuclear Physics,.Bormio – Italy, ed. by I. Iori, 2004.

[PAG04b] A. Pagano et al., Procs. of 5° Italy-Japan Symposium - Recent achievements and perspectives in Nuclear Physics, Naples 2004.

[PAP05] M. Papa et al., Procs. of International Workshop on Multifragmentation and related topics, Nov. 28 – Dec. 1 2005, Catania, Italy , Ed. SIF, 399 (2005).

[PIA02] S. Piantelli et al., Phys. Rev. Lett. C 885, 052701 (2002).

[PIR14] *Pirrone et al.,* J. Phys : Conf. Ser. vol. 515, 012018 (2014).

[PEI94] G. Peilert, H. Stocker and W. Greiner, Rep. Prog. Phys. 57, 533-602 (1994).

[PHA93] L. Phair et al., Nucl. Phys. A 564, 453 (1993).

[PLA99] E. Plagnol et al, Phys. Rev. C 61, 014606(1999).

[POC95] J. Pochodzalla al., Phys. Rev. Lett. 75, 1040 (1995).

[POC96] J. Pochodzalla et al., contr. To 'Critical phase and collective observable', procs. of CRIS 1996, Edited by S. Costa, S. Albergo, A. Insolia, C. Tuvè, World Scientific (1996), 1.

[POL05] G. Politi et al., 2005 IEEE Nuclear Science Symposium Conference Record, N28-5 (2005).

[POL05b] G. Politi et al., Procs. of International Workshop on Multifragmentation andrelated topics IWM2005, Nov. 28 – Dec. 1 2005, Catania, Italy , Ed. SIF, 83 (2005).

[POP98] R. Popescu et al., Phys. Rev. C 58, 270 (1998).

[RIC01] J. Richter and P. Wagner, Phys. Rep. 350, 1(2001).

[RIV01] M.F. Rivet et al., Procs. of International Workshop on Multifragmentation and related topics IWM2001, Catania, Italy, Nov. 2001, 11.

[RUS06] P. Russotto et al., Int. Jour. Of. Mod. Phys. E 15, 410 (2006); *P. Russotto*, *Phd Thesis*, Catania University (2006).

[SAN95] T.C. Sangster et al., Phys. Rev. C 51, 1280 (1995).

[SCH04] W.U. Schröder and J. Töke, in Nonequilibrium Physics at Short Time Scales,edited by K. Morawetz (Springer-Verlag, Berlin/Heidelberg/New York, 2004), p.417.

[SOB97] L.G. Sobotka et al., Phys. Rev. C 55, 2109 (1997).

[SOU06] R.T. De Souza, N. Le Neindre, A. Pagano and K.H. Schmidt , Eur. Phys. J. A 30, 275-291 (2006).

[STE95] A.A. Stefanini et al, Zeit. Phys. A 351, 167 (1995).

[STO82] H. Stöcker et al., Nucl. Phys. A387, 205c-208c (1982).

[STO86] H. Stöcker and W. Greiner, Phys. Rep.137, 277-392 (1986).

[SWI83] W. J. Swiatecki, Aust. J. Phys. 36, 641 (1983).

[TOK95] J. Töke, et al. , Phys. Rev. Lett. 75, 2920 (1995).

[TSA96] B. Tsang et al, Phys. Rev. C53 R1057 (1996).

[TSA06] Eur. Phys. J. A30, 129-139 (2006).